Proton Minibeam Radiotherapy

Dipl.–Phys. Stefanie Girst

Vollständiger Abdruck der von der Fakultät für Luft– und Raumfahrttechnik der Universität der Bundeswehr München zur Erlangung des akademischen Grades eines

Doktors der Naturwissenschaften (Dr. rer. nat.)

genehmigten Dissertation.

Vorsitzender:	Prof. Dr. phil. rer. soc. Berthold Färber
1. Gutachter:	Prof. Dr. rer. nat. Günther Dollinger
2. Gutachter:	Prof. Dr. rer. nat. Jan Wilkens

Die Dissertation wurde am 24.07.2015 bei der Universität der Bundeswehr München eingereicht und durch die Fakultät für Luft– und Raumfahrttechnik am 21.10.2015 angenommen. Die mündliche Prüfung fand am 08.03.2016 statt.

Abstract

The risk of developing adverse side effects in the normal tissue after radiotherapy is often limiting for the dose that can be applied to the tumor. Proton minibeam radiotherapy, a spatially fractionated radiotherapy method using sub-millimeter proton beams, similar to grid therapy or microbeam radiation radiotherapy (MRT) using X-rays, has recently been invented at the ion microprobe SNAKE in Munich. The aim of this new concept is to minimize normal tissue injuries in the entrance channel and especially in the skin by irradiating only a small percentage of the cells in the total irradiation field, while maintaining tumor control via a homogeneous dose in the tumor, just like in conventional broad beam radiotherapy. This can be achieved by optimizing minibeam sizes and distances according to the prevailing tumor size and depth such that after widening of the minibeams due to proton interactions in the tissue, the overlapping minibeams produce a homogeneous dose distribution throughout the tumor.

The aim of this work was to elucidate the prospects of minibeam radiation therapy compared to conventional homogeneous broad beam radiotherapy in theory and in experimental studies at the ion microprobe SNAKE. Treatment plans for model tumors of different sizes and depths were created using the planning software LAP-CERR, to elaborate suitable minibeam sizes and distances for the individual tumors. Radiotherapy-relevant inter-beam distances required to obtain a homogeneous dose in the target volume were found to be in the millimeter range.

First experiments using proton minibeams of only 10 µm and 50 µm size (termed microchannels in the corresponding publication Zlobinskaya et al. 2013) and therapy-conform larger dimensions of 100 µm and 180 µm were performed in the artificial human in-vitro skin model EpiDermFT^{TM} (MatTek). The corresponding inter-beam distances were 500 µm, 1 mm and 1.8 mm, respectively, leading to irradiation of only a few percent of the cells in the skin tissue, but with significantly increased doses (up to 5000 Gy) compared to the average dose of 2 Gy, which was applied homogeneously in further skin samples for comparison. Gaussian-shaped minibeams of even larger sizes (σ= 260 µm and 520 µm, inter-beam distance 1.8 mm) were analyzed in further experiments to evaluate the effect of increasing beam sizes as in deeper-lying tissues. Acute side effects were quantified via the MTT tissue viability test and the release of inflammatory pro-

teins into the culture medium and showed improved results for minibeam compared to homogeneous irradiation. Genetic damage, an indicator for secondary tumor induction, was analyzed via the micronucleus test in the epidermal keratinocytes and was less than half for minibeams up to 180 µm size compared to homogeneous fields. Increasing minibeam sizes, i.e. increasing fractions of irradiated skin (receiving a dose higher than the average dose of 2 Gy) increased the number of micronuclei per divided cell, but never exceeded the genetic damage induced by a homogeneous dose distribution.

A more authentic and representative in-vivo skin model, accounting for higher complexity with blood vessels, further cell types, follicles, glands and especially a working immune system, was used in the next step to further examine the side effects of minibeam radiotherapy compared to homogeneous irradiation. The central part of the ear of adult BALB/c mice was irradiated with 20 MeV protons, using an average dose of 60 Gy in a field of 7.2 x 7.2 mm^2. The 4 x 4 minibeams of nominal 6000 Gy had a size of 180 x 180 μm^2 and inter-beam distances of 1.8 mm, as in previous in-vitro skin experiments. Minibeam irradiation induced no ear swelling or other visible skin reaction at any time, while significant ear swelling (up to 4-fold), skin reddening (erythema) and desquamation developed in homogeneously irradiated ears 3-4 weeks after irradiation. Loss of hair and sebaceous glands only occurred in the homogeneous irradiation fields and did not recover during the monitoring phase of 90 days.

Taken together all theoretical considerations and experimental findings, proton minibeam radiation therapy appears suitable for the implementation in clinical tumor therapy using protons and/or heavy ions, as it reduces side effects in the normal tissue compared to conventional broad beam irradiation. However, the upper limit of the minibeam size for tissue sparing and the technical feasibility are still to be elucidated as current technologies might have to be improved and adapted for the generation of sub-millimeter proton beams of energies up to 250 MeV at therapy plants.

Zusammenfassung

In der Strahlentherapie von Tumoren ist das Risiko von Nebenwirkungen im Normalgewebe häufig limitierend für die Dosis die im Tumor appliziert werden kann. Proton Minibeam Strahlentherapie wurde am Ionenmikrostrahl SNAKE in München entwickelt, um die Schädigung von Normalgewebe, insbesondere der Haut, zu minimieren. Durch die Verwendung von submillimeter großen Protonenstrahlen erfolgt die Bestrahlung räumlich fraktioniert, d.h. nur auf kleinen Flächen innerhalb des Bestrahlungsfeldes auf der Haut wird Dosis appliziert. Die Tumorkontrolle wird wie in der konventionellen Strahlentherapie durch eine homogene Tumordosis gewährleistet, die sich nach Aufweitung der Minibeams durch Wechselwirkungen der Protonen mit dem durchquerten Gewebe im gesamten Tumor ergibt. Die homogene Tumorbestrahlung wird durch eine individuell an die Tumorgröße und -lage angepasste Optimierung der Minibeam-Abstände erreicht.

Das Ziel dieser Arbeit war das Potential der Minibeam Strahlentherapie im Vergleich zur konventionellen homogenen Strahlentherapie in der Theorie und in experimentellen Studien am Ionenmikrostrahl SNAKE aufzuklären. Bestrahlungspläne für Modelltumoren verschiedener Größe und Tiefe wurden mit der Planungssoftware LAPCERR erstellt, um passende Minibeam Größen und Abstände für den jeweiligen Tumor auszuarbeiten. Therapierelevante Minibeam Abstände, die für eine homogene Dosis im Zielvolumen erforderlich sind, liegen dabei im Bereich von einigen Millimetern.

Erste Experimente mit Proton Minibeams von nur 10 µm und 50 µm Größe (noch *Microchannels* genannt in der zugehörigen Veröffentlichung Zlobinskaya et al. 2013) und therapie-konforme größere Minibeams von 100 µm and 180 µm wurden in dem künstlichen, menschlichen in-vitro Hautmodell EpidermFT^{TM} (MatTek) durchgeführt. Die dazugehörigen Minibeam Abstände waren 500 µm, 1 mm und 1,8 mm, so dass nur ein paar Prozent der Zellen im Hautgewebe bestrahlt wurden, jedoch mit signifikant höheren Dosen (bis zu 5000 Gy) als die mittlere Dosis von 2 Gy, die zum Vergleich homogen auf weiteren Hautproben appliziert wurde. Gaußförmige Minibeams von noch größeren Dimensionen (σ= 260 µm und 520 µm, Abstand 1,8 mm) wurden in weiteren Experimenten angewendet, um den Effekt von zunehmenden Strahlgrößen, wie in tieferliegenden Geweben, zu untersuchen. Akute Nebenwirkungen wurden

mittels MTT Viabilitätstest und der Expression von Entzündungsproteinen in das Nährmedium quantifiziert und zeigten bessere Ergebnisse für Minibeam als für homogene Bestrahlung. Genetischer Schaden, ein Indikator für Sekundärtumorinduktion, wurde mit dem Mikrokerntest in den epidermalen Keratinozyten analysiert, und war weniger als halb so groß für Minibeams bis 180 µm Größe verglichen mit homogenen Feldern. Zunehmende Minibeam Größen, d.h. zunehmender Anteil an bestrahlter Haut (mit Dosen größer als die mittlere Dosis von 2 Gy) erhöhte die Anzahl von Mikrokernen pro geteilter Zelle, aber überstieg nie den genetischen Schaden, der von einer homogenen Dosisverteilung induziert wurde.

Zur Berücksichtigung der höheren Komplexität der menschlichen Haut, mit Blutgefäßen, weiteren Zelltypen, Haarfollikeln und Drüsen, vor allem aber eines funktionierenden Immunsystems, wurde als nächster Schritt ein authentischeres und repräsentativeres in-vivo Hautmodell beim Vergleich von Minibeam und homogener Bestrahlung verwendet. Der zentrale Bereich des Ohres von erwachsenen BALB/c Mäusen wurde mit 20 MeV Protonen bei einer mittleren Dosis von 60 Gy in einem Feld von 7,2 x 7,2 mm^2 bestrahlt. Die 4 x 4 Minibeams von nominal 6000 Gy waren 180 x 180 μm^2 groß und hatten einen Abstand von 1,8 mm, wie in den vorangegangen in-vitro Hautexperimenten. Minibeam Bestrahlung induzierte zu keiner Zeit Ohrschwellungen oder andere sichtbare Hautreaktionen, während signifikante Verdickungen (bis zu 4-fach), Erythem (Hautrötung) und Desquamation (Abschuppung) nach 3-4 Wochen in homogen bestrahlten Ohren auftraten. Der Verlust von Talgdrüsen und Haaren trat nur in den homogenen Bestrahlungsfeldern auf und erholte sich nicht bis zum Ende der Beobachtungszeit von 90 Tagen.

Betrachtet man alle theoretischen Überlegungen und experimentellen Ergebnisse zusammen, so scheint die Proton Minibeam Strahlentherapie geeignet für die Implementierung in der klinischen Tumortherapie mit Protonen und/oder Schwerionen, da sie die Nebenwirkungen im normalen Gewebe verglichen mit der konventionellen homogenen Bestrahlung reduziert. Jedoch gilt es dafür noch die obere Grenze der Minibeam Größe für eine Gewebeschonung und die technische Machbarkeit der Methode aufzuklären, da aktuelle Technologien eventuell verbessert und angepasst werden müssten um sub-millimeter Protonenstrahlen von Energien bis zu 250 MeV an Therapieanlagen zu erzeugen.

Contents

Chapter 1

Introduction

The annual incidence of cancer is about 14 million worldwide [1], with almost half a million new cancer diagnoses per year in Germany alone [2]. Nearly two thirds of these cancer patients are treated with radiotherapy alone or in conjunction with other therapies, most of them receiving X-ray irradiations in the form of external beam radiotherapy (EBRT) [3–5]. The aim of each curative therapy is tumor control, i.e. to prevent the tumor from growing further, which can be achieved by depositing a tumor type-dependent radiation dose in the tumor. Even though a higher tumor dose will increase the likelihood of tumor control, this cannot be achieved without depositing dose in the surrounding tissues, thus limiting the maximum applied doses to minimize side effects in the healthy tissue. The use of ions for radiotherapy instead of photons offers a way to reduce dose deposition behind the target and in the beam entrance channel in front of the tumor, as the depth-dose distributions differ significantly (cf. Fig. 1.1): while energy deposition by photons decreases exponentially with depth after a dose buildup region of a few cm for megavoltage beams, charged particles increasingly lose their energy with depth with most of the energy deposited at the end of their range in the so-called Bragg peak, allowing a conformal irradiation of the target structure [6]. This can also be achieved with X-rays using several irradiation fields from different directions to generate a dose escalation in the tumor, but while depositing a higher total energy in the healthy tissue of the patient compared to ions at the same tumor dose.

Nevertheless, radiation induced toxicities in irradiated healthy tissue remain a problem in radiotherapy, limiting the dose to the tumor and reducing the patients' quality of life during and after treatment [7, 8]. The commonly applied radiation doses can lead to various side effects during the treatment period (acute side effects) and in the months or years after treatment (long-term side effects), with severity and duration depending on the irradiated organs, the treatment parameters (radiation quality, dose, fractionation

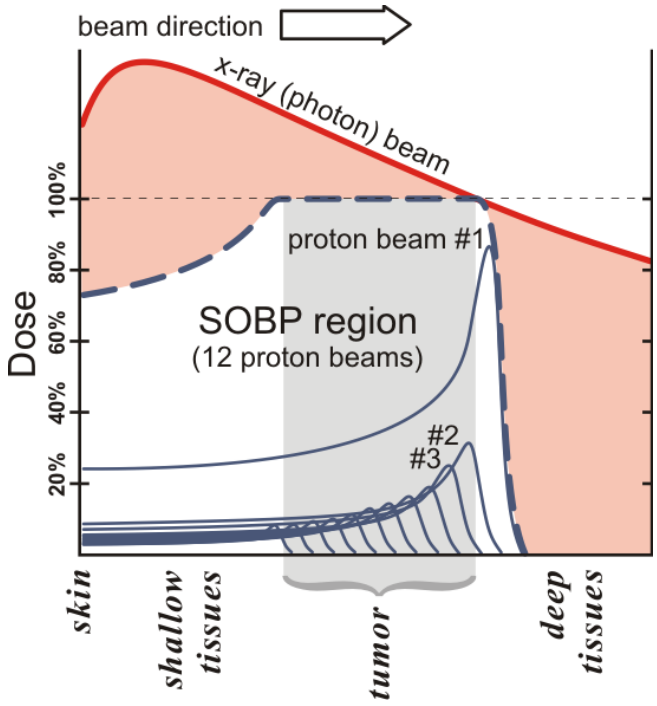

Figure 1.1: *Depth-dose distribution for X-rays (red line) and protons (thin blue lines): the proton Spread-Out Bragg Peak (SOBP, dashed blue line) is the sum of several Bragg peaks with different numbers of protons at increasing depths (i.e. increasing proton energies) to form a homogeneous dose in the tumor (grey area). The orange area represents the additional X-ray dose compared to the proton irradiation when treating the same tumor, which can cause additional damage to normal tissues, especially of the skin. From [9]*[(1)]

scheme, treatment field size, etc.) and the patient itself. Main side effects are fatigue and skin changes (dermatitis) in the treatment area, other, body part-dependent, acute reactions include hair loss in the irradiated field, diarrhea, nausea and vomiting, urinary and bladder changes, sexual changes and mouth and swallowing problems. Late reactions in the treatment area after more than three months arise mainly from damage to blood vessels and cells in the connective tissues and may involve fibrosis (scarring), epilation, dryness (mouth, eyes, axilla, vagina), joint problems, infertility, lymphedema and secondary cancer, dependent on body part and radiation dose. [7, 8]

[(1)]"Comparison of dose profiles for proton v. x-ray radiotherapy" by User:MarkFilipak. Licensed under GFDL (http://www.gnu.org/copyleft/fdl.html) or CC BY-SA 3.0 via Wikimedia Commons - http://commons.wikimedia.org/wiki/File:Comparison_of_dose_profiles_for_proton_v._x-ray_radiotherapy.png#/media/File:Comparison_of_dose_profiles_for_proton_v._x-ray_radiotherapy.png

Almost 90 % of radiotherapy patients develop moderate to severe skin reactions and irritations, due to the high turnover rate of epithelial skin cells. Skin changes range from mild erythema (like in a sun burn) and dry desquamation (itching, peeling) to moist desquamation (skin break-down, open wound) and ulceration. These are the combined results of a decline in functional stem cells, changed endothelial cells, inflammation, necrosis and cell death of skin cells [8]. Skin irritations often occur in areas with natural folds of the skin (e.g. underneath the breast, in the groin) or where the skin is particularly thin (e.g. throat). Although skin reactions can be uncomfortable and even painful, most changes will recover quickly after the end of treatment. [7, 8]

As side effects from radiotherapy are mostly limited to the treatment area, modern radiation techniques aim to reduce normal tissue damage in this region. In Intensity-Modulated Radiation Therapy (IMRT) damage of normal tissues is reduced by irradiating the tumor from several beam directions and thus with lower doses in each beam. Another approach is the so-called spatial fractionation, i.e. irradiation of only a (small) fraction of the normal tissue and sparing of the rest from radiation, e.g. by using a grid or sieve in front of the skin [10–12]. Such an inhomogeneous dose distribution within the healthy tissue of the entrance channel has been shown to reduce normal tissue injuries due to the increased tissue tolerance for smaller treatment volumes, termed dose-volume effect [13]. Normal tissue can also be spared from radiation by the use of small, non-overlapping beams instead of homogeneous broad beams, leaving the tissue in between the beams unirradiated. This is often referred to as microbeam radiation therapy (MRT [14–16]) or minibeam radiotherapy [17–19] when micrometer-sized or sub-millimeter planar or pencil beams are applied with inter-beam distances larger than the beam dimensions. MRT using synchrotron-generated X-rays was developed at the National Synchrotron Light Source (NSLS), Brookhaven National Laboratory (BNL) and the European Synchrotron Radiation Facility in Grenoble (France) for neurosurgical treatments and controls the tumor with the maintained pencil beam/microarray geometry applied to the skin [14, 20, 21]. A homogeneous tumor dose, as in conventional radiotherapy, can only be obtained by overlaying microarrays from opposing beam directions, matching size and distance of the planes/pencil beams. Similar ideas have been examined using heavy ions such as carbon ions, which basically maintain the applied irradiation geometries due to low scattering in tissue [22].

In this work, micro- or minibeam radiation therapy using proton pencil beams is presented and analyzed in theory and in experiments at the ion microprobe SNAKE[(2)]. The major difference to X-ray MRT is that proton beam scattering in tissue is not negligible, such that initial beam sizes are not maintained in depth. However, this

[(2)] Superconducting Nanoprobe for Applied nuclear (German: Kern-) physics Experiments

can be exploited to generate a homogeneous dose distribution inside the tumor, when beam dimensions and distances are optimized for the given tumor depth. The concept of spatial fractionation remains valid in the irradiated regions close to the skin, allowing the reduction of side effects in this normal tissue, while keeping the advantages of tumor control by a homogeneous dose. This idea may also be applicable for sub-millimeter sized heavy ion beams, although additional beam divergence might be necessary.

The following two chapters give a detailed introduction to the underlying idea of micro- or minibeam radiation theory (chapter 3) and the experimental setup at SNAKE used for this work (chapter 4). The fifth chapter describes the experimental study of minibeam radiotherapy in an in-vitro human skin model, while chapter 6 presents the further development in an in-vivo mouse skin model. Chapter 7 discusses the achieved results in both models and their implications for future implementation in radiotherapy, together with possible continuation of this research and future prospects and applications.

Most of the ideas and experiments presented in this work have already been published in Zlobinskaya et al. 2013 [23], Girst et al. 2015*a* [24], Girst et al. 2015*b* [25] and Girst et al. 2015*c* [17], which explains the sometimes inevitable closeness of the used expressions and explanations.

Chapter 2

Charged particles in radiotherapy

2.1 Dose deposition of energetic ion beams

Charged particles belong to the class of ionizing radiation, like alpha, beta and gamma radiation and neutrons. As directly ionizing radiation, energy deposition in matter happens mainly via direct Coulomb interactions between the energetic ion and electrons of atoms in the medium (i.e. excitation and ionization), but also with target nuclei [6]. These interactions can, when sufficient energy is transferred, lead to the destruction of molecules. The physical measure describing the mean energy ΔE imparted in a mass Δm is the (absorbed) dose D, with unit Gray, $1\,\mathrm{Gy} = 1\,\mathrm{J/kg}$:

$$D = \frac{\Delta E}{\Delta m} \tag{2.1}$$

Dose deposition is not homogeneous within the target, but varies along the beam direction, described by the linear energy transfer (LET), and perpendicular to the beam (radial or lateral dose distribution) [6, 26]. The linear energy transfer is the energy deposited in the medium per distance Δl,

$$LET = \frac{\Delta E}{\Delta l} \tag{2.2}$$

The LET is closely related to the so-called stopping power (or better speaking stopping force) of the ion, i.e. the energy loss per unit path length dE/dx, although energy loss via bremsstrahlung is not included in the LET (restricted linear collision stopping power) [6]. For energetic ions, stopping power and LET are nearly equivalent, as energy loss via bremsstrahlung is negligible, due to the large ion masses compared to e.g. electrons [26, 27].

The LET varies over a wide range between different ions and for different ion energies, with a maximum for protons at an energy E_{max} of approximately 100 keV in water (see Fig. 2.1) [26]. Water is typically used as target material for representation

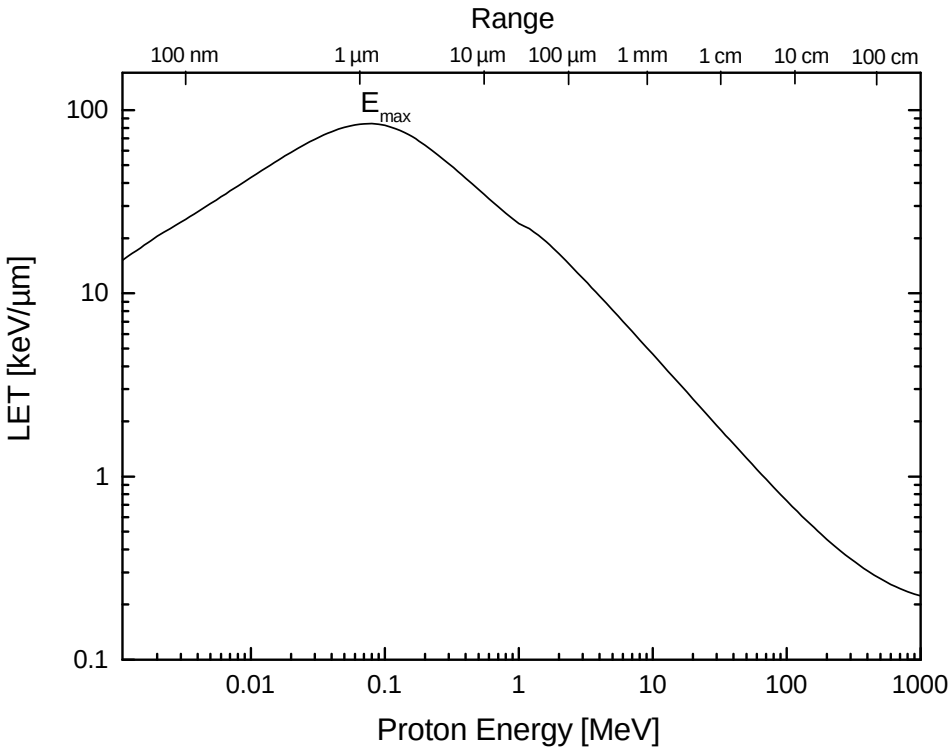

Figure 2.1: *Linear energy transfer (LET) of protons in water, calculated with SRIM [29].*

of biological matter. For higher energies than E_{max}, energy transfer is dominated by interactions with target electrons (i.e. electronic stopping) and the LET can be approximated by the Bethe formula [28]:

$$-\frac{\mathrm{d}E}{\mathrm{d}x} = \left(\frac{e^2}{4\pi\epsilon_0}\right)\frac{4\pi n}{m_e}\frac{z^2}{v^2}\ln\left(\frac{2m_e}{I}v^2\right) + \text{relativistic corrections} \tag{2.3}$$

with atomic number z and velocity v of the ion, electron density n and mean excitation potential I of the target material, electron mass m_e and dielectric constant ϵ_0. The LET is basically dependent on the squared atomic number (charge) of the ion and the inverse energy (z^2/E) as the logarithmic term is negligible, until relativistic effects come into play above energies of about 1 GeV/u.

For energies larger than E_{max}, the ions are completely ionized. Beneath this energy, the ions are not further completely ionized so that the nuclear charge is shielded and thus the Coulomb interaction between ion and target electrons is reduced, leading to a decrease in LET in this energy region (with decreasing energy). At energies of a few

keV/u, the interaction of the ion with the target nuclei contributes significantly to the total energy deposition (nuclear stopping) [26].

2.1.1 Depth-dose distribution

As a charged particle passes through matter, it continuously transfers energy to the medium and thus slows down. The increasing energy loss with decreasing energy (above E_{max}[(1)]) leads to a growing energy loss towards the end of the ion range and a large energy deposition shortly before the ion stops. This results in the so-called Bragg peak at the end of the depth-dose curve of charged particles (cf. Fig. 1.1, the thin blue lines representing monoenergetic proton beams of different energies[(2)]). For an ion beam, the range of the single ions straggles around a mean range due to the statistic process of energy loss, which leads to a broadening of the depth-dose curve compared to a single ion (together with the effect of lateral straggling).

In the radiotherapy of tumors, a homogeneous dose distribution within the target volume is desired in order to irradiate every single tumor cell with a lethal dose. For the generation of a homogeneous tumor dose along the beam axis, several Bragg peaks of different energy and intensity can be superimposed to form a so-called Spread-Out Bragg Peak (dashed blue line in Fig. 1.1). Compared to photon irradiations, basically no dose is deposited behind the tumor and also the dose in front of the tumor can be reduced, even when irradiating from only one direction (cf. Fig. 1.1). A dose escalation in deep-lying tumors can for X-rays only be achieved by irradiating from several directions. This reduces the dose in the healthy tissues but with the effect of irradiating several times the volume of healthy tissues compared to the irradiation from one direction. Therefore, more energy is deposited in the healthy tissue compared to proton or heavy ion irradiation for the same tumor dose. The characteristic dose deposition of charged particles compared to photons allows a lower total energy deposition in the tissue surrounding the tumor, and thus sparing of healthy tissue [26, 30].

2.1.2 Radial dose distribution

For the description of the radial or lateral dose deposition of an ion beam in matter, the widening of the beam due to particle scattering and the radial dose deposition of each single ion via secondary particles has to be taken into account.

---

(1) Protons with energy E_{max} (and maximum LET) only have a range of $\sim 1\,\mu m$ in water.

(2) The Bragg peak of a single ion is even more pronounced, with increases of the LET by more than two orders of magnitude.[26]

The deflection of ions due to the interaction with atomic electrons is negligible compared to that caused by the Coulomb interaction with positively charged, heavy atomic nuclei [27]. Most of these deflections are still rather small due to the shielding of the nuclear charge by the surrounding electron cloud, but large-angle Rutherford scattering can occur as well, when the ion passes very close to a nucleus of the target material. Each particle of a beam undergoes many (small-angle) scattering events on its track through matter, statistically adding up to a net angular and lateral deviation from the original beam direction, hence termed "Multiple Coulomb Scattering" (MCS) [27]. The resulting angular particle distribution of the ion beam can be approximated by a Gaussian distribution with standard deviation Θ_{MCS}, given by the "Highland's formula"[31], parametrizing Moliere's theory [32]

$$\begin{aligned}\Theta_{MCS} &= \frac{14.1MeV}{pv} z\sqrt{\frac{x}{L_R}}\left[1+\frac{1}{9}\log_{10}\left(\frac{x}{L_R}\right)\right] rad \\ &\cong \frac{z}{E_{kin}}\sqrt{x}\end{aligned} \tag{2.4}$$

where z is the atomic number, p the momentum and v the velocity of the ion. The material-specific radiation length L_R is the mean length which reduces the energy of a (high-energy) electron to 1/e of its initial value ($1/L_R$ of water = 0.02753/cm). x is the thickness of a small slab of material. For thicker geometries, equation 2.4 is integrated over the geometry depth, taking x infinitesimal [31, 33].

The width of the lateral distribution of an ion beam can therefore be approximated by $\sigma \approx x \times \Theta_{MCS} \propto x^{3/2}$ for small depths x. However, due to large-angle scattering events, the lateral shape of the charged particle beam is not a perfect Gaussian, but has long tails which can again be approximated via a second (broader) Gaussian [27, 31].

The radial dose deposition of every single particle of an ion beam has to be overlaid to the particle distribution of the beam to obtain the overall lateral dose distribution. In ionization events between charged particles and target material, part of the energy deposited by the ion is transferred to secondary electrons as kinetic energy. The maximum energy of these delta electrons is maximal in head on collisions and is limited by the ion's velocity [26]. Therefore, energy and dose deposition is not restricted to the ion track itself (core) but also takes place in the surrounding region. The dose in this so-called penumbra decreases with the inverse of the squared distance from the track ($\propto 1/r^2$) until a maximum radius $r_{max} = 0.0616\,(E/A)^{1.7}\,\mu$m, with E/A in MeV/u [34–36]. For 20 MeV and 200 MeV protons this radius is 10 µm and 0.5 mm, respectively, which needs to be taken into account when calculating lateral dose distributions of proton beams in different depths. However, due to the sharp drop of the dose with

$1/r^2$ from the ion track, the dose contribution of electrons with large ranges is negligible in the total radial dose deposition of (high-energy) protons, even for sub-millimeter sized beams ($\sigma \gtrsim 100\,\mu\text{m}$) (cf. Fig. 2.2).

Secondary particles like neutrons can be generated in inelastic nuclear reactions between ions and the target material as well, leading to further changes in the dose deposition of the original ion beam and should also be considered in dose calculations and simulations [27].

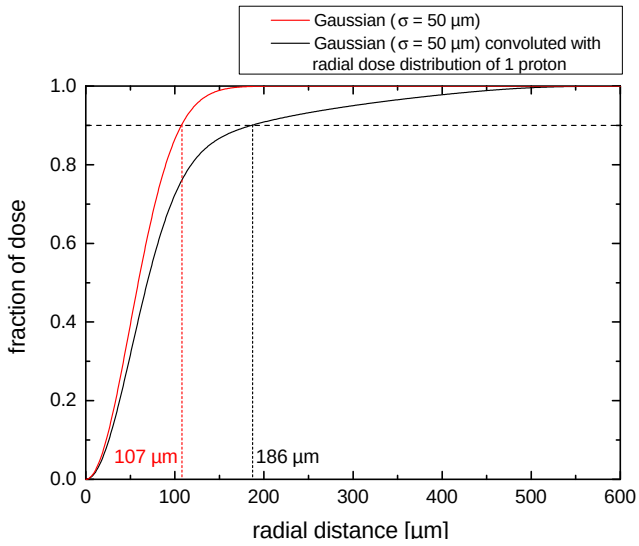

(a) *Radial dose distribution for a 200 MeV proton beam of $\sigma = 50\,\mu m$ standard deviation (black line). 90 % of the dose is deposited within a radius of 186 μm compared to 107 μm for a true Gaussian dose distribution (red line).*

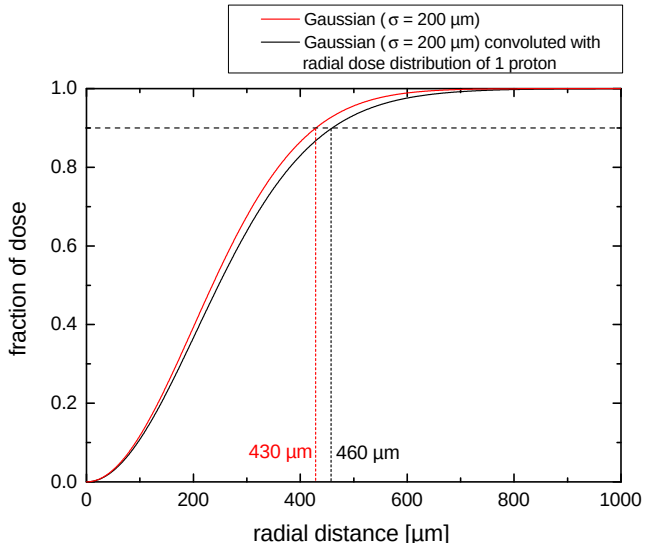

(b) *Radial dose distribution for a 200 MeV proton beam of $\sigma = 200\,\mu m$ standard deviation. 90 % of the dose is deposited within a radius of 460 μm compared to 430 μm for a true Gaussian dose distribution (red line).*

Figure 2.2: *Radial dose distribution for a 200 MeV proton beam of 50 μm (a) and 200 μm (b) standard deviation (black line). Displayed is the fraction of the total dose deposited within a radial distance from the center of the proton beam for a true Gaussian dose distribution (red line) and for a Gaussian proton distribution convoluted with the radial dose deposition of one proton (black line, cf. [37, 38] with $r_{min} = \frac{v}{c} \times 40\,nm \sim 16\,nm$ and $r_{max} = 0.5\,mm$).*

2.2 Radiation effects on tumors and normal tissue

2.2.1 Radiation effects on cells

The most radio-sensitive part of living cells is the nucleus and especially the DNA[3] molecule, which contains the genetic information. Damage can occur via direct interaction of ionizing radiation with the target structures (i.e. through ionization or excitation with subsequent chemical reactions leading to biological damage), or indirectly, via interaction with other atoms or molecules in the cell (particularly water), producing free radicals, which can on their part induce damage to the critical structures. Particles with high linear energy transfer (LET $> 10\,\mathrm{keV}/\,\mu\mathrm{m}$) interact mainly directly with biological material, inducing DNA damage continuously along their tracks ("densely ionizing"). Low LET radiation such as X-rays or protons ($> 4\,\mathrm{MeV}$) is "sparsely ionizing", causing about two thirds of the damage indirectly [39, 40] via highly reactive radicals. [6, 41]

The DNA molecule has a double helical structure and consists of two strands, built up of sugar (deoxyribose) and phosphate groups and held together by hydrogen bonds between the four bases. The sequence of the approximately $6\,\mathrm{x}\,10^9$ base pairs in a (diploid) human cell, which are complementary on opposite strands - adenine with thymine, guanine with cytosine - specifies the genetic code. [42]

Common damages of the DNA molecule are base damages and breaks of one strand (single-strand break, SSB), with about 10^3 occurring per Gray in a cell. SSB present no serious danger to the cell as they are repaired readily and without loss of information with the opposite strand as template. Breaks of both DNA strands that are well separated (i.e. > 10 base pairs apart) are treated like individual SSB. [43]

Two strand breaks lying opposite each other (or < 10 base pairs apart) form a double-strand break (DSB). This is the most dangerous type of radiation-induced DNA damage and occurs about 35 times per Gray of low-LET radiation in each cell [44], with an additional quadratic increase in DSB at high doses (e.g. 1 % additional DSB at 100 Gy [26]) from SSB at opposite strands that lie close together by chance [45]. The frequency of DSB produced by heavy ions can be even higher due to an increased relative biological effectiveness (RBE)[4]. Unrepaired DSB can lead to programmed cell death (apoptosis) or permanent cell cycle arrest. Incorrect or incomplete repair can result in mutations or chromosomal aberrations, if wrong DSB ends from different

[3] deoxyribonucleic acid

[4] The RBE is defined as the ratio of the dose of a (low-LET) reference radiation (e.g. 250 kV X-rays) to the dose of the test radiation, causing the same biological level of effect [6].

chromosomes are linked, forming dicentric or acentric chromosomes for example [46]. Eventually this may lead to carcinogenesis [47].

In summary, an irradiated cell can either show no effect at all, undergo apoptosis, transformation or mutation, underlie a division delay, a reproductive failure, genomic instability or show adaptive or bystander responses, which are influenced by neighboring irradiated cells [6, 48]. After 1 Gy of radiation, only about 30 % of mammalian cells will die despite the large number of induced lesions due to the efficient DNA repair mechanisms [41].

2.2.2 Tumor treatment with radiation

The cell-damaging effects of ionizing radiation are exploited in the therapy of solid tumors to reduce or ideally even stop their growth. This so-called (local) tumor control, when all clonogenic tumor cells have been inactivated [41], is the main goal of the treatment, requiring the deposition of a sufficiently high and homogeneous dose in the tumor. Nevertheless, dose deposition in the surrounding tissue is inevitable, but should be kept to a minimum to reduce the risk of acute and long-term side effects in this healthy tissue. The "therapeutic window" is the difference between the dose required for tumor control and the normal tissue tolerance dose, leading to a "maximum probability of complication-free tumor control" [6]. The position and shape of the dose-response curves for tumor control (TCP curve) and for normal tissue complications (NTCP curve) (cf. Fig. 2.3) determine the optimal radiation dose for maximum tumor control probability with an acceptably low degree of side effects [6, 41]. The damage to normal tissues depends on the radio-sensitivity, the irradiated volume and the delivered dose [6]. It can be reduced by dividing the total dose into multiple fractions spread over time (fractionation), leading to repair of sublethal damage between the dose fractions and repopulation of cells [6]. By contrast, recovery and repair of tumor cells is less efficient after irradiation and reoxygenation and redistribution of the cell cycle phases between the fractions can even increase radio-sensitivity (5 R's of fractionated radiotherapy[(5)], [6]). Standard fractionation schemes are based on five daily treatments per week (1.8-2 Gy per fraction) and a total treatment time of several weeks [6, 41].

[(5)] Radio-sensitivity, Repair, Repopulation, Reoxygenation, Redistribution

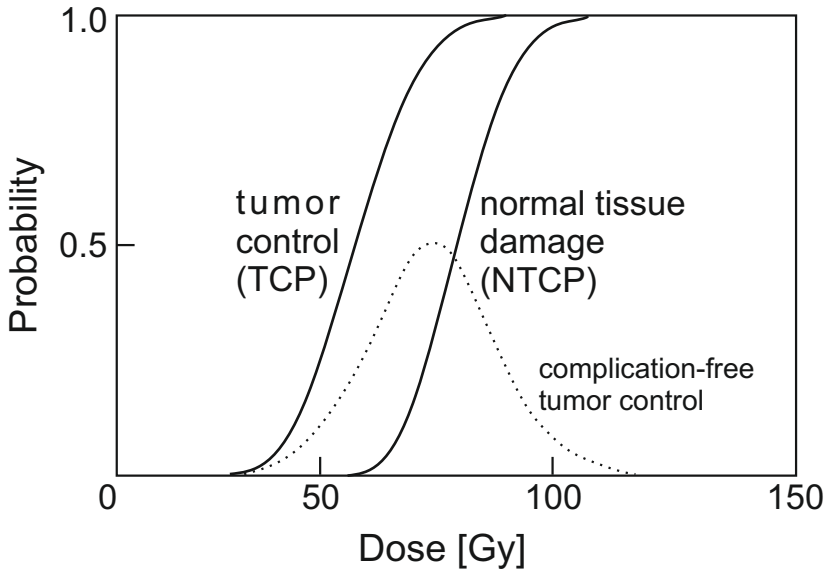

Figure 2.3: *Dose-response curves for tumor control (tumor control probability, TCP) and normal tissue damage (normal tissue complication probability, NTCP). The complication-free tumor control rate initially increases with dose, but falls again due to a steep increase in the incidence of normal tissue damage. Adapted from [6, 41].*

Chapter 3

The concept of proton micro- and minibeam radiotherapy

3.1 Normal tissue sparing in spatially fractionated radiotherapy

A known strategy for reducing radiation damage in normal tissue is by simply sparing (large) parts of it from irradiation, a method called "spatial fractionation", as opposed to time/dose fractionation. This means that the treatment area is divided into several smaller regions of not necessarily equal size and shape and of which not all receive the same high dose required for tumor control. Some regions can therefore receive much higher doses than by a homogeneous, unsegmented irradiation, while other, potentially larger regions, receive barely any dose ("peaks" and "valleys"). The mean or integrated dose of such a spatially fragmented irradiation field can be chosen equal to the corresponding homogeneous irradiation field (e.g. same total number of particles re-distributed over the irradiation field), but it can also be lower or higher in order to achieve a certain therapeutic index.

A higher tolerance for spatially segmented than for continuous radiation beams is attributed to undamaged, migratory cells adjacent to the radiation-injured areas [16, 41, 49, 50]. First implementations of this idea were already developed in the early 20th century, when Köhler in Germany (1909) [51] and then Liberson in the United States (1933) [52] performed irradiations through a metal grid or sieve, which divided the large irradiation field in several small beams that were interrupted by shielded areas [53]. Further grid studies in animals with X-rays [10], electrons [11], and protons [12] and extensive clinical experience indicated that small non-confluent areas of the skin and subcutaneous normal tissues can tolerate large radiation doses without significant acute or late normal tissue damage [53]. This is described by the "dose-volume effect"

(Withers et al. 1988, [13]), which means that the maximum tolerable doses before complications of radiotherapy appear, increase as irradiated tissue volumes are made smaller [22]. Especially organs with a parallel organization of functional subunits[(1)] such as lung, liver or kidney, but also the skin or oral mucosa with a high cellular migration capacity, profit from only partial irradiation as long as a tissue-specific threshold volume is not exceeded, leaving enough subunits to sustain the physiological organ function [41]. In these small irradiation volumes, very high doses (up to several thousands Gy) can be applied, which lead to the death of all hit cells but still do not limit the function of the whole organ. By contrast, relatively radio-resistant tissues like the spinal cord or the esophagus, which have a serial arrangement of functional subunits and therefore depend on the function of each individual subunit, can be "functionally inactivated by the irradiation of only a small volume" [41], making them highly vulnerable to "hot spots" of high doses. The serial organization of small blood vessels, however, adds a "serial factor" also for parallel organized tissues [41], making the vascular system another important factor for tissue tolerance in different irradiation schemes [16, 54, 55].

Despite the skin-sparing properties of megavoltage photon beams used in current radiotherapy centers compared to early orthovoltage applications, grid approaches are still in use in the treatment of massive and bulky tumors, or when re-treating recurrent cancers [53, 56, 57]. However, the resulting inhomogeneous dose in the tumor can potentially influence tumor control, as not all tumor cells are hit by sufficient doses.

New irradiation methods have emerged in the last decades which also exploit the concept of tissue sparing by spatial fractionation. While in grid therapy applications the field or segment sizes are up to 2 cm [57], microbeam radiation therapy (typically abbreviated MRT [16]) and minibeam radiation therapy (sometimes shortened MBRT [19]) use micrometer-sized (typically 20-200 μm [16]) and sub-millimeter beams ($\sim$ 500-700 μm [19]) of rectangular (planar) or radially symmetrical shape (pencil beams with circular or regular polygonal cross-sections). For planar beams the shorter dimension should not exceed 1 mm, while the other dimension can be arbitrarily long, which is assumed to provide similar tissue sparing as pencil beams of the same (smaller) dimension (patent to Slatkin et al. 1994 [16]).

The geometrical arrangement of the micro- or minibeams is described in a plane perpendicular to the beam direction and is typically chosen on a rectangular grid with equidistant spacing between the minibeams in each direction (typically 50-500 μm in MRT, up to several mm in MBRT [16, 57]). The optimum inter-beam or center-to-

[(1)] FSU: largest tissue volume that can be regenerated from one single surviving clonogenic cell [13, 41]

center distances are dependent on the dose profile of the minibeams and should leave sufficient unirradiated or minimally irradiated zones in the normal tissue through which the minibeams pass, to allow cells between the minibeams (e.g. endothelial cells[2] or oligodendrocytes[3] in the brain) to divide and repopulate tissues injured or ablated by the irradiation [16]. Due to the macroscopic dimensions of the tumor of several millimeters to centimeters, several hundred or thousand minibeams will be required to cover the target volume. The dose profile of the irradiation field shows a pattern of peaks and valleys and is often characterized by the peak-to-valley dose ratio (PVDR), which is the quotient of the dose in the (center of the) minibeams and the dose between the beams [19]. Large PVDR ratios are desired for efficient radiotherapy with low normal tissue damage, meaning peak doses which are lethal to most dividing cells and valley doses which are low enough to allow most normal cells to survive the radiation [16].

Within the normal tissue, this inhomogeneous dose distribution with peaks and valleys is supposed to reduce normal tissue toxicity, which is caused by the radiation-induced inflammatory mediators and DNA damage responses. Even though the biological mechanisms through which micro- or minibeams spare normal tissue are still not completely understood, the already mentioned "dose-volume effect" and the "microscopic prompt tissue repair effect", are often considered the relevant mechanisms [18, 22]. As long as the valley doses are close to zero, large parts of the tissue receive almost no dose, exploiting the "dose-volume effect" as in the grid approaches. The cells in the path of the micro-/minibeams receive very high doses causing high cell death rates in these regions, but migrating viable cells from the unirradiated regions adjacent to the irradiated site can infiltrate the damaged tissue and thus reduce tissue necrosis in the minibeam paths [16, 50]. This kind of repair mechanism is less efficient in large lesions, where a much wider margin of undamaged tissue around the lesion would have to supply these cells, meaning that vascular, connective tissue and other cells would have to migrate larger distances to the damage sites and penetrate these larger areas of damaged tissue, leading to accumulation of cellular debris and toxic materials in their center, causing even secondary tissue damage [50]. Furthermore, the destruction of sensitive cells can lead to the release of proteolytic (i.e. protein decomposing) enzymes, which in a small volume can diffuse and dilute into the adjoining undamaged tissue, but can accumulate in large volumes, causing further cell damage (e.g. cytolysis) [54].

The "microscopic prompt tissue repair effect" is specific for micro- and minibeam

[2] Cells lining the interior surface of blood or lymphatic vessels

[3] Type of non-neuronal cells for homeostasis, myelin production and support and protection for neurons in the brain and peripheral nervous system

radiotherapy with sub-millimeter beam diameters[4]. It describes the fast repair of capillary blood vessels in the direct path of the minibeams via regeneration of angiogenic cells from the undamaged regions in-between within days or even hours, which then can support and enhance the repair of other normal tissues in the minibeam paths [18, 22]. Especially in the brain, endothelial cells which were lethally irradiated by a minibeam are replaced by endothelial cells regenerated from adjoining, minimally irradiated endothelium of brain vasculature between the minibeams[5] [16, 58]. But also in the rectum and the intestines, the critical role of the vasculature in the development of radiation damage in normal tissues has been demonstrated [59].

For skin, however, the number of radiation-damaged capillaries may be of secondary importance, as the healing of skin lesions is a very complex process, which cannot be explained by only a vascular effect [50]. Rather the interface between injured and uninjured tissues seems of great importance, which is larger for small lesions. In the healing process of a large ulcerous lesion (after $> 25\,\mathrm{Gy}$), the outer rim on the border to unirradiated tissue becomes hyperplastic and hypertrophied (i.e. enlarged due to an abnormal increase in the number or size of the tissue cells), but thus survives, while the central area of the lesion becomes necrotic [50]. Perhaps similar mechanisms and factors protecting the borders of a large irradiated area are important for the tissue sparing of small areas of irradiated skin [50].

Further effects that might play a role in micro- and minibeam radiotherapy are the so-called radiation-induced bystander effects in cells not directly hit by radiation. They are mediated through direct physical cell contact (gap junction intercellular communication) or through secretion of diffusible signaling proteins into the surrounding medium (e.g. cytokines, which initiate multiple downstream signaling cascades)[56, 58]. The "classical" bystander effect [60–62], which leads to a decreased survival of unirradiated cells by communication with irradiated cells, may reduce the tissue sparing effect, especially at small inter-beam distances. But there might also be "beneficial" bystander effects which lead to tissue regeneration, when these signaling protein cascades promote migration, proliferation and differentiation of viable cells in the unirradiated regions between the minibeams [58]. In experiments using modulated radiation fields, it has been found that the survival of shielded, minimally irradiated cells increases, when they are communicating with cells irradiated with a high or lethal dose [48, 63]. This is attributed to repair mechanisms stimulated in the viable cells of the shielded region

[4] Curtis 1967: 1 mm diameter, 22 MeV deuteron beams (140 Gy) led to the complete destruction of the mouse cerebellum tissue in 240 days [55]

[5] Radiation damage to the neurons only occurs at enormous doses, as they never undergo cell division [55].

by the cell death in the irradiated region. Furthermore, survival of irradiated cells increased, when communication with cells receiving a small radiation dose took place. The low dose to the "shielded" region might have caused these cells to signal to the neighboring irradiated cells and thus increase their survival [48]. This might also explain the recovery after microbeam irradiation with valley doses as high as $\sim 20\,\mathrm{Gy}$ [58]. These two beneficial bystander effects were also found in in-vitro experiments in the absence of blood vessels, making an underlying vascular repair mechanism unlikely [48].

3.2 Tumor control in spatially fractionated radiotherapy

Grid approaches, MRT or MBRT using X-rays or heavy ions maintain the pencil beam/grid geometry in the complete beam path due to low scattering in tissue, leading to an inhomogeneous dose distribution also in the tumor (in unidirectional irradiations). The tissue sparing effect of spatially fractionated radiation beams is lower for tumor tissue than for normal tissue, which is attributed to a different, more radio-sensitive microvasculature which cannot easily recover from irradiation and therefore causes the loss of tumor blood perfusion and consequently influences tumor growth [57, 59, 64]. Tumor vasculature is generally less dense, often with less well-developed walls, larger and more variable diameters and higher vascular endothelial cell turnover rates, leading to less efficient recovery by proliferating and repopulating endothelial cells from the valleys [57, 59]. Furthermore, the fast intermingling of lethally irradiated cells (from the peak dose regions) and undamaged cells (from the valleys) within the tumor might increase intercellular communication [65] and thus lead to an overall reduced cell proliferation [66]. This means that the tumoricidal effect of spatially fractionated irradiation does not only arise from direct cellular damage in the irradiated high-dose regions, but involves functional tissue changes and maybe also bystander effects [66].

Nevertheless, complete tumor control is not reliably induced by spatially fractionated tumor irradiations, presumably due to the sparing of clonogenic tumor cells which allow repopulation and repair. Even though an increase in survival time (compared to unirradiated controls) by an inhomogeneous tumor dose distribution has been demonstrated in many animal studies, tumors (mainly of the brain) were not always ablated but often only their growth was retarded or suppressed [49, 59, 65–68]. This might be due to viable proliferating tumor cells surviving at the tumor margin, where nutrients can be supplied by adjacent normal blood vessels, enabling tumor recurrence or progression from the tumor periphery [67]. In general, tumor control rates increased

with radiation dose and especially the valley dose and inter-beam distances appeared to play a crucial role for tumor cure, as it determines the cell survival in the shielded regions between the micro-/minibeams [59, 64, 66–68]. The highest rates for tumor control were found at valley doses of $\sim$25-40 Gy, while valley doses below 20 Gy yielded $\lesssim$30 % tumor cure [59, 65, 67, 68]. However, normal tissue damage also increased with increasing valley doses and thus reduced the therapeutic index of the treatment [59, 68]. Normal (brain) tissue damage even led to death despite an ablated tumor [68]. Therefore, the aim of controlling the tumor with spatially fractionated irradiation as in unidirectional MRT often has to be compromised in favor of normal tissue sparing in order to achieve an overall improved outcome with maximum survival times.

However, also in spatially fractionated radiotherapy, a uniform dose distribution in the tumor can be generated in order to control the tumor as in conventional radiotherapy, while profiting from normal tissue sparing of the healthy tissue in the beam path. This can be achieved either by interlacing of beams from two or more directions[(6)] in the target volume, i.e. adjusting position and spacing of the beams such that the "gaps" in the irradiation fields are filled from another direction (patent to Dilmanian et al. 2012 [22]) or by using protons or light ions instead of X-rays as described in the next section.

3.3 Spatial fractionation using proton micro- and minibeams

The original concept of micro- or minibeam radiotherapy was not considered valuable for protons or other light ions due to their large angular straggling (Multiple Coulomb scattering[(7)]) and thus increasing beam diameters in depth [22]. Nevertheless, we consider this feature to be of great advantage, as the widening proton minibeams can be merged to form a homogeneous broad beam in the tumor just like in conventional radiotherapy (see Fig. 3.1), with all the well-established profits of tumor control with a homogeneous tumor dose while benefiting from spared shallow tissues close to the skin (cf. Zlobinskaya et al. 2013 [23], Dilmanian et al. 2015 [18]).

This new approach can also be applied to heavier ion species, e.g. when treating deeper targets (due to their lower angular straggling) or for radio-resistant tumors

[(6)] Only two orthogonal directions can be used in X-ray MRT due to the exponential depth-dose characteristics also behind the tumor which would destroy the peak-valley dose pattern.

[(7)] For the same range (tumor depth), heavier ions require a higher (initial) kinetic energy, which leads to lower scattering.

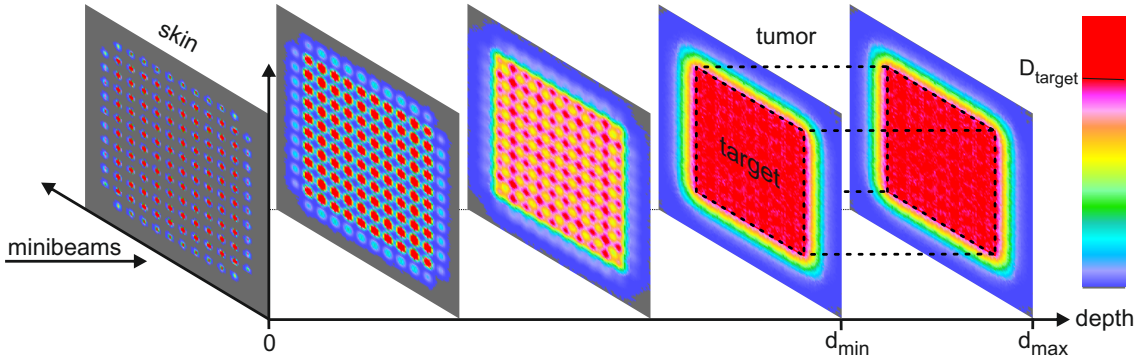

(a) *3D representation of the minibeam concept. Non-overlapping minibeams are applied on the patient's skin (depth 0) on a square grid and spread on their way towards the tumor (between d_{min} and d_{max}), forming a homogeneous dose in the target volume.*

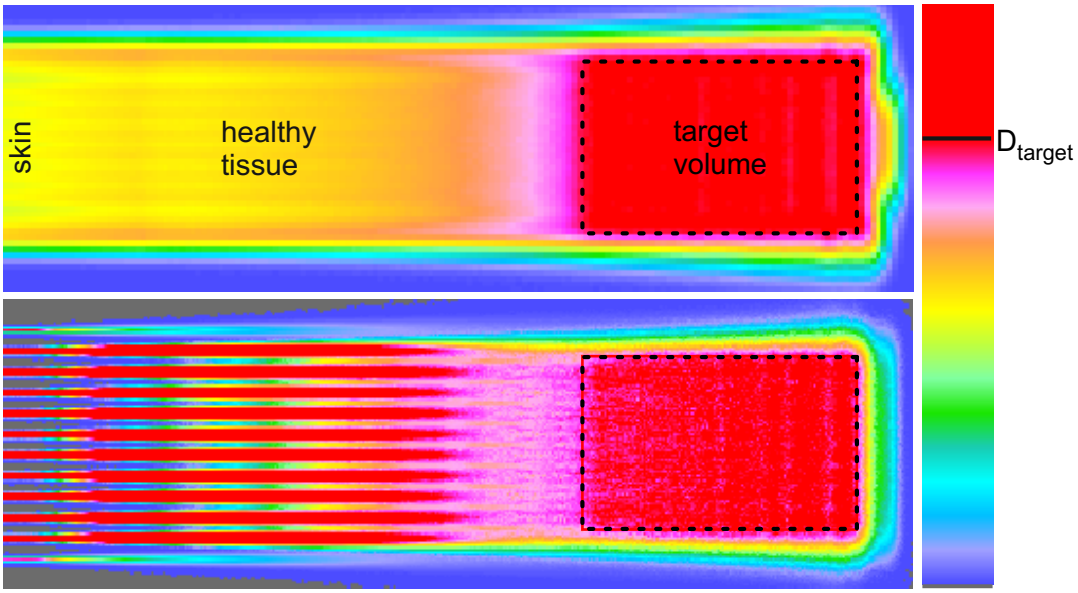

(b) *Comparison of homogeneous (top) and minibeam irradiation (bottom) of a target volume with a homogeneous tumor dose D_{target}. The profile is cut through a slice of minibeams in (a).*

Figure 3.1: *Schematic illustration of the concept of minibeam radiotherapy. Doses $\geq D_{target}$ are displayed in red.*

(due to their larger RBE), although an additional beam divergence might be required (cf. [18, 23]).

Proton micro- or minibeam irradiation is similar to conventional beam scanning techniques, where a millimeter-sized pencil beam is scanned on a rectangular grid covering the target area. In nearly all cases, the pencil beam can be characterized by a two-dimensional Gaussian for the lateral dose distribution with standard deviation σ

(often called beam radius or width) and full width at half maximum FWHM $\sim 2.35\,\sigma$. The center-to-center distance (*ctc*) between two adjacent points on the grid is typically chosen smaller than twice the radius of the pencil beam ($ctc \leq 2\sigma$), resulting in a nearly homogeneous dose distribution in the tumor, but also already in the skin of the patient [23]. In the proposed micro- or minibeam irradiations, the radius of the proton beam is much smaller, in the micrometer or at least sub-millimeter range[(8)], while the inter-beam distances remain in the millimeter range. Due to small angle scattering of the protons and initial beam divergence, the minibeams spread laterally while passing through normal tissue and merge together at the depth of the tumor (or earlier if desired, cf. Fig. 3.1 and 3.2). The inter-beam distance has to be optimized to obtain a dose coverage of the target between 95% and 107% of the prescribed tumor dose [69] (cf. section 3.4) if no other beam divergence is assumed, but could be enlarged further when introducing additional beam divergence that results in a larger beam at the tumor site [23]. The number of protons in one minibeam is the same as in the case of larger pencil beams applied on the same grid, and thus results in a homogeneous tumor irradiation with the same average dose that is reached with a scanned pencil beam or broad beam.

As already described in section 3.1, the inhomogeneous dose distribution with peaks and valleys in the normal tissue is supposed to reduce normal tissue toxicity. In the skin and in other shallow tissues underneath, large parts of the tissue receive almost no dose, as the valley doses are close to zero if the minibeams are non-overlapping, profiting from the "dose-volume effect"[(9)]. The cells in the path of the minibeams receive much higher doses than the mean tumor dose[(10)], but can be replaced by migrating viable cells from the unirradiated adjacent regions [16, 23, 50]. Also the mentioned "microscopic prompt tissue repair effect" due to fast vascular repair in the paths of sub-millimeter beams might contribute to the better tolerance of normal tissue to proton minibeam irradiation. In the skin, however, the healing of lesions seems to be more dependent on the size of the lesion (and thus the size of the interface between injured and uninjured tissues) than on the effect of the vascular repair (cf. section 3.1, [50]).

Potential clinical applications of proton minibeams include brain tumors (particularly pediatric), head and neck tumors (sparing the parotid glands), tumors near the eye socket and spinal cord tumors of children, or other tumors where sparing of shal-

[(8)] The discrimination between micro- and minibeams is set to $\sim 100\,\mu$m FWHM.

[(9)] Due to the widening of the minibeams and thus the smoothing of the lateral dose distribution with increasing tissue depth, normal tissue toxicity increases towards the tumor.

[(10)] The maximum dose in the minibeams decreases with increasing minibeam size.

low tissues proximal to the tumor is beneficial [18]. Tumors of the lung or the liver might profit from hypofractionated proton minibeam irradiations (i.e. at higher doses per fraction) as the tissue sparing of chest and abdomen wall would allow much higher doses to the tumor [18]. However, breathing or cardiac motions or external movements might require stereotactic devices in certain cases [16]. Due to the close similarity of this idea to conventional scanning beam applications, the "only" requirement for clinical implementation would be the smaller beam dimensions, whereas beam scanning, treatment planning and other procedures would need only minor adaptations and developments. However, the generation of sub-millimeter proton beams at (existing) radiotherapy plants will also pose a (manageable) challenge.

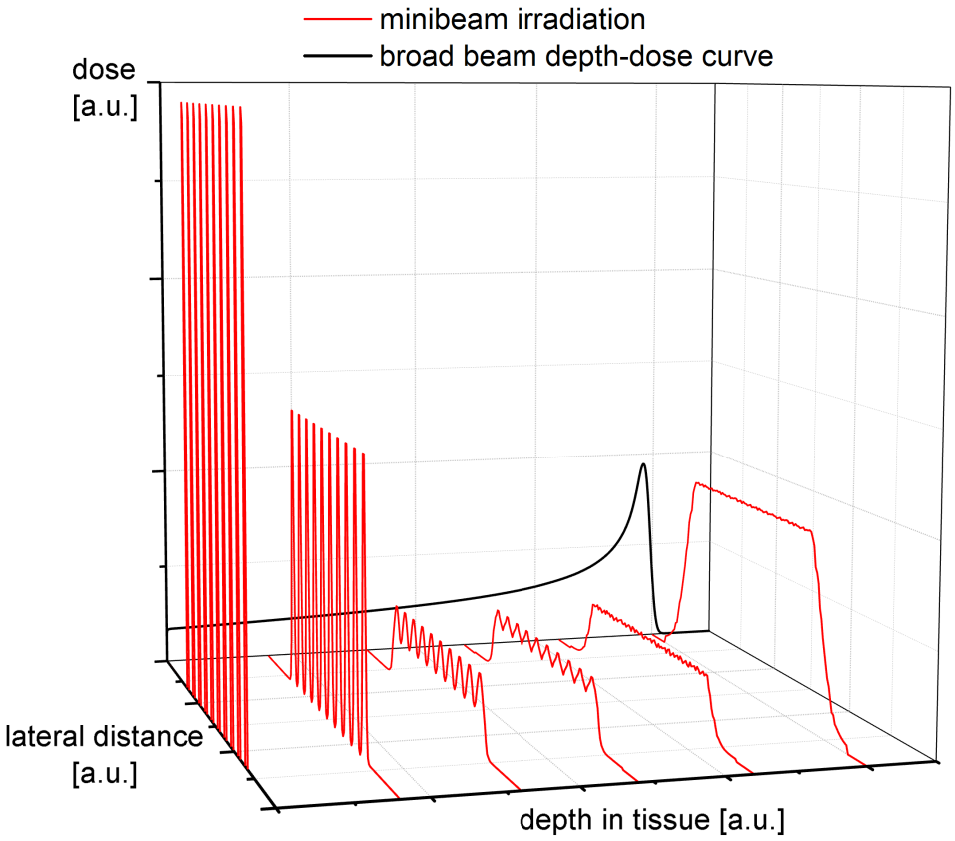

Figure 3.2: *Schematic illustration of the concept of minibeam radiotherapy (2D). Non-overlapping minibeams (red) (of only one energy for simplicity) are applied on the patient's skin (depth 0) and spread on their way towards the tumor, forming a homogeneous dose at their Bragg peak (at d_{max}, cf. black depth-dose curve on the central axis of a broad beam of the same energy), but also at a lower depth d_{min} of the tumor. For simplification, only the central part of the irradiation field, where all beamlets have equal heights and border effects do not play a role, is displayed.*

3.4 Treatment planning for proton minibeam radiotherapy

3.4.1 General considerations

In order to obtain maximum tissue sparing while still controlling the tumor with the prescribed homogeneous dose (within 95-107 % [69]), the inter-beam distances (*ctc*) and the minibeam sizes, e.g. characterized by the standard deviation σ_0 for Gaussian beams, have to be optimized for the given tumor depth and thickness (t, in beam direction), i.e. for the smallest and largest depth of the target volume, d_{min} and d_{max}. In a real patient, different tissue or bone densities need to be taken into consideration, as proton scattering will change in materials of different atomic number, e.g. bone will lead to a larger spread than muscle tissue of the same thickness [57].

For simplicity, all calculations performed in this section will be based on a (rectangular) water tumor in a water phantom which is irradiated from one or two directions with non-divergent minibeams with equidistant center-to-center distances *ctc* (in x and y, for simplicity). The introduction of an additional beam divergence would allow for the enlargement of the *ctc* distances while still obtaining a homogeneous dose distribution in the target volume due to the increased beam sizes at the tumor site. Irradiation from several directions would allow dose reduction in each beam while keeping the same minibeam parameters leading to a homogeneous tumor dose in every single beam direction. Only the irradiation from two opposite directions would enable an additional increase in inter-beam distances (by $\sqrt{2}$) when the minibeams from the one direction are shifted by ($ctc/2$, $ctc/2$) in x and y, but would require a high delivery and positioning accuracy (see Fig. 3.5, g and h).

In the following, the term "beam" will describe all minibeams coming from one direction, covering the lateral dimensions of the target volume (in x- and y-direction). The beam is divided laterally into $m \times n$ (Gaussian) minibeams of size σ_0 (standard deviation) with equidistant *ctc* distances in x and y. In axial direction (z), each minibeam (or generally called pencil beam) consists of several sublets, i.e. protons of different energies E, which cover the axial dimension of the target with the Spread-Out Bragg Peak. Protons with the lowest energy E_{min} "stop" at the proximal side of the target volume (at d_{min}) while the sublets with the highest energy E_{max} should have a range of d_{max}. The proximal side of the target (d_{min}) determines the depth in which all proton minibeams (or more precisely, all sublets) have to overlap homogeneously. This is a very important constraint, as an inhomogeneous dose distribution for just one proton energy (at any depth within the tumor) will destroy the homogeneous dose

distribution of all other sublets. As the angular straggling decreases with increasing energy (cf. equation 2.4), protons with E_{max} will have spread the least at d_{min} and will therefore determine the condition for the *ctc* distances:

$$ctc \leq 2\sigma'_{E_{max}}(d_{min}) \tag{3.1}$$

with $\sigma'_{E_{max}}(d_{min})$ being the total width of the radial dose distribution of the minibeam sublets of energy E_{max} in the depth d_{min}. The radial dose distribution can be approximated by a Gaussian distribution with standard deviation σ

$$D(x,y) \propto \frac{1}{2\pi\sigma^2} \exp\left(-\frac{x^2+y^2}{2\sigma^2}\right) \tag{3.2}$$

The total width of the radial dose distribution in a certain depth is set together by the initial beam width σ_0 and the width of the lateral dose spread (due to MCS, secondary electrons, etc.) in the respective depth $\sigma_E(d)$ according to:

$$\sigma'^2_E(d) = \sigma_0^2 + \sigma_E^2(d) \tag{3.3}$$

as the convolution of two Gaussian distributions is again normally distributed with the given standard deviation [70].

For a more precise dose calculation, the radial dose distribution in depth d should be approximated by two Gaussian distributions (see section 2.1.2[11]),

$$D_2(x,y) \propto \frac{h_1(d)}{2\pi(\sigma_0^2+\sigma_1^2(d))} \exp\left(-\frac{x^2+y^2}{2(\sigma_0^2+\sigma_1^2(d))}\right) + \frac{h_2(d)}{2\pi(\sigma_0^2+\sigma_2^2(d))} \exp\left(-\frac{x^2+y^2}{2(\sigma_0^2+\sigma_2^2(d))}\right) \tag{3.4}$$

where $\sigma_1 < \sigma_2$ and the relative heights of the two Gaussians $h_1(d)$ and $h_2(d)$ add up to 1 for a normalized distribution (cf. Fig. 3.4). For the determination of an appropriate *ctc* distance, the smaller Gaussian (σ_1) should be used in equation 3.3, as the wider Gaussian only improves the homogeneity.

The easiest approximation for equation 3.1, which will definitely lead to a homogeneous tumor dose independent of the initial minibeam size is

$$ctc \leq 2\sigma_{E_{max}}(d_{min}) \tag{3.5}$$

where only the radial dose distribution of the protons with the highest energy at the proximal side of the target volume (i.e. at depth d_{min}) is considered. When using the two Gaussian approximation, again σ_1 should be taken for optimization of *ctc* in

[11] The second Gaussian reflects nuclear interactions as well as large-angle Coulomb scattering.

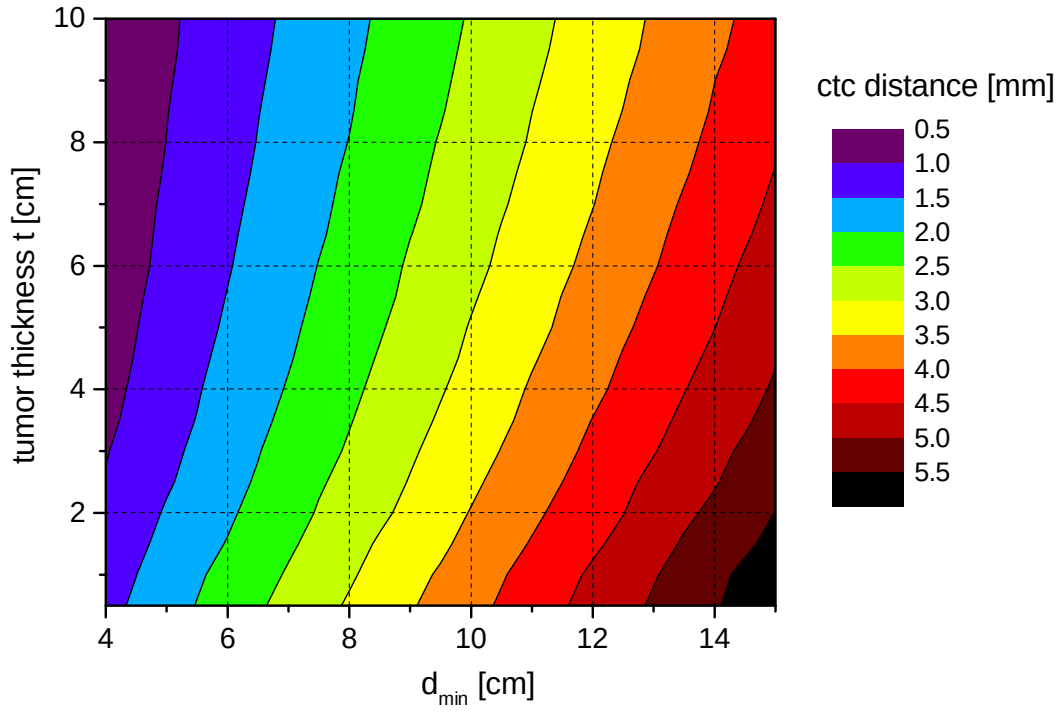

Figure 3.3: *Maximum center-to-center distances (ctc) for treating target volumes of different thickness (t) at various (proximal) depths (d_{min}) with a homogeneous dose (considering parallel incoming minibeams). For minibeam sizes $\sigma_0 > 0$ or additional beam divergence larger ctc distances might be possible. Optimization of ctc based on the σ_1 data of the "Two Gaussian" model in LAP-CERR.*

eq. 3.5. Figure 3.3 displays the maximum *ctc* distances which can be applied to treat a tumor of thickness t at a depth of d_{min} (to $d_{max} = d_{min} + t$), assuming initial minibeam sizes $\sigma_0 = 0$ (based on the σ_1 data of the "Two Gaussian" model implemented in LAP-CERR). For typical tumor thicknesses and depths, the *ctc* distances are in the millimeter range, with larger inter-beam distances for deeper-lying tumors.

The initial minibeam size (σ_0) should be chosen as small as (technically) possible in order to gain as much as possible from the dose-volume effect, which appears to be more important than the relative number of irradiated cells. However there might be a lower limit, under which there is no medical advantage of further reducing the minibeam size (see Outlook).

3.4.2 Calculation of treatment plans using LAP-CERR

The radial dose distribution of the protons in a certain depth, which is required for all these optimizations, can be obtained from analytical formulas (cf. section 2.1.2), from particle Monte Carlo simulations (e.g. using Geant4) or from measurements in a suitable setup. The data used in this work is from the database of LAP-CERR, which contains Gaussian approximations (with one or two Gaussian functions) of Geant4-simulated proton dose distributions[12] ("One Gaussian" or "Two Gaussian" model) [71].

The treatment planning system CERR (Computational Environment for Radiotherapy Research)[72] is an open source radiation therapy tool for photon irradiations written in MATLAB [73], which was extended for protons[13] and heavier ions in the group of Prof. Dr. Jan Wilkens at the Klinikum rechts der Isar, Munich [71, 74]. It allows three-dimensional dose calculations for computed tomography (CT) images of real patients, but also the generation of simpler phantoms, as was employed here (cf. Appendix A). For the target and non-target structures in the phantom, doses and penalties are defined and the software optimizes the relative weights of the proton sublets (i.e. protons of the same energy) to obtain a homogeneous dose in the target volume under the constraints for the non-target structures.

The "One Gaussian" and "Two Gaussian" dose data for 100 MeV (range $\sim 7.65\,\mathrm{cm}$) protons[14] is displayed in Fig. 3.4. The width σ of the radial dose distribution is zero in the first centimeter due to the limited Geant4 resolution in radial direction of 0.1 mm, which does not allow fitting of the radial dose spread up to this depth (cf. [71]). The fit of the second Gaussian is only possible from a certain (energy-dependent) depth [71] and leads to a sudden increase in σ_2 and a sudden decrease in σ_1, which until that depth have the same value. This can result in a sudden "thinning" of small minibeams ($\sigma_0 \lesssim 200\,\mu\mathrm{m}$) which is not physical but is difficult to handle differently. For more precise dose calculations and refined models in the future, the resolution of (Geant4) simulations would have to be increased to obtain the dose spread also in the first centimeter and a continuous extension of the widths and heights of the second Gaussian towards smaller depths analogous to analytical models might become helpful or even necessary.

[12] The G4EmStandardPhysics option3, the G4HadronQElasticPhysics and the G4HadronInelasticQBBC modules are used to describe electromagnetic and elastic and inelastic hadronic interactions [71].

[13] LAP: laser-accelerated protons

[14] The Geant4 simulations were run for an initial beam width σ_0 of 2 mm [71].

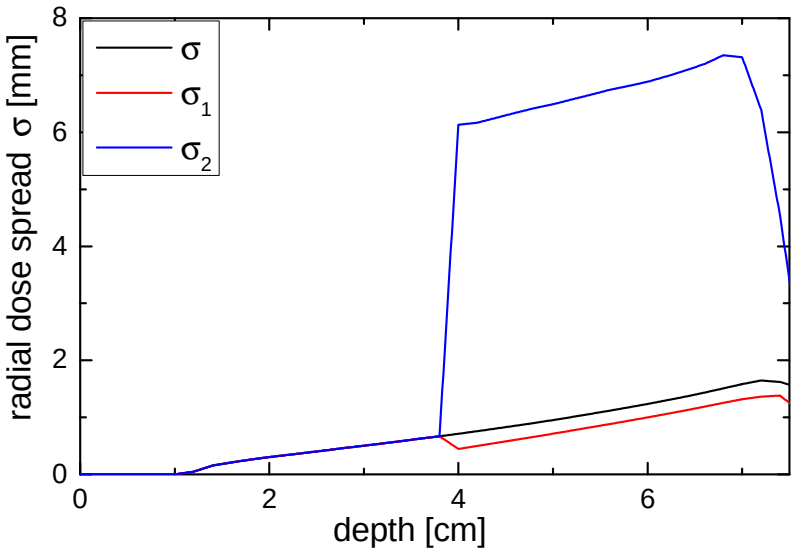

(a) *Width of the radial dose distribution of a 100 MeV proton beam in different depths (in water), as fit result using one (σ) and two (σ_1, σ_2) Gaussians.*

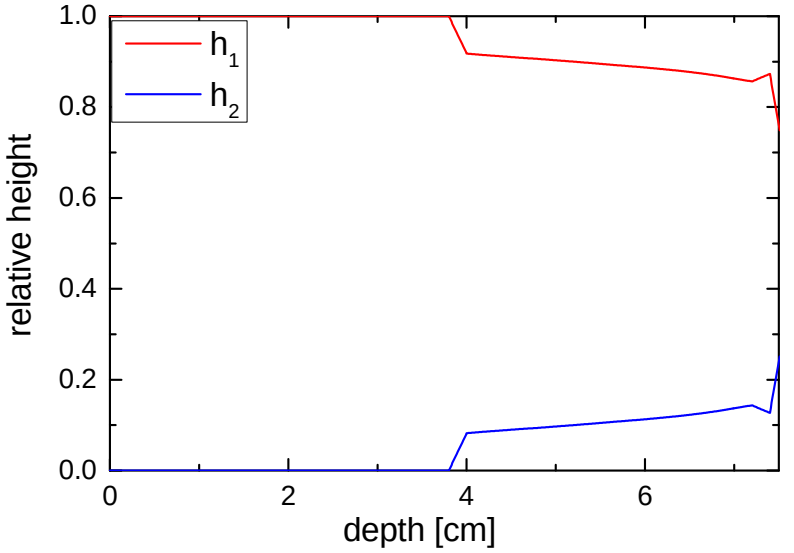

(b) *Relative heights of the two Gaussian distributions from the "Two Gaussian" fit of the radial dose distribution of a 100 MeV proton beam.*

Figure 3.4: *Radial dose distribution of proton beams in different depths in water ("One Gaussian" and "Two Gaussian" widths and relative heights). The exemplary proton energy is 100 MeV with an associated range of 7.65 cm (data implemented in LAP-CERR).*

Two model target volumes of different sizes and depths in a (water) phantom were generated for illustration of the concept of proton minibeam radiotherapy with LAP-CERR. Figure 3.5 displays the first target of size $3\,\mathrm{x}\,3\,\mathrm{x}\,5\,\mathrm{cm}^3$ which is situated at a depth of 10.6-15.6 cm underneath the skin and is irradiated from one side with 144 minibeams of $\sigma_0 = 250\,\mu\mathrm{m}$ size (i.e. FWHM $\sim 0.6\,\mathrm{mm}$) and *ctc* distances of 3.6 mm or from two sides with the same total number of minibeams but *ctc* distances of $\sqrt{2}\times 3.6 = 5\,\mathrm{mm}$ (cf. [23]). The smaller target volume of size $1.5\,\mathrm{x}\,1.5\,\mathrm{x}\,2.5\,\mathrm{cm}^3$ (Fig. 3.7) is at a lower depth of 7-9.5 cm and is covered with 100 minibeams with initial size $\sigma_0 \sim 80\,\mu\mathrm{m}$ (i.e. FWHM $\sim 180\,\mu\mathrm{m}$) and 1.8 mm *ctc* distance (cf. [17]). The treatment plans were calculated with the "One Gaussian" and the "Two Gaussian" model of the lateral spreads, leading to better results in greater depth for the "Two Gaussian" parametrization, as especially close to the Bragg peaks the wider tails of the proton distributions come into play. However, in the region, where σ_2 starts to become relevant, the truth lies somewhere between both models. Nevertheless, the simulations demonstrate the applicability of proton minibeam irradiations for typical tumor sizes and depths, yielding a homogeneous dose in the target volume.

For the dose distributions in Fig. 3.5 and 3.7 the color scale was chosen such that all doses equal or larger than the prescribed target dose (D_{target}) are displayed in red. This allows to visualize all regions with high doses, however the absolute values remain unknown. For example in the skin, the dose in the minibeams is about 10-20 times higher than the dose to the target volume. In order to illustrate also the absolute doses, dose profiles through the minibeams or in-between for different depths can be used (cf. Fig.3.6).

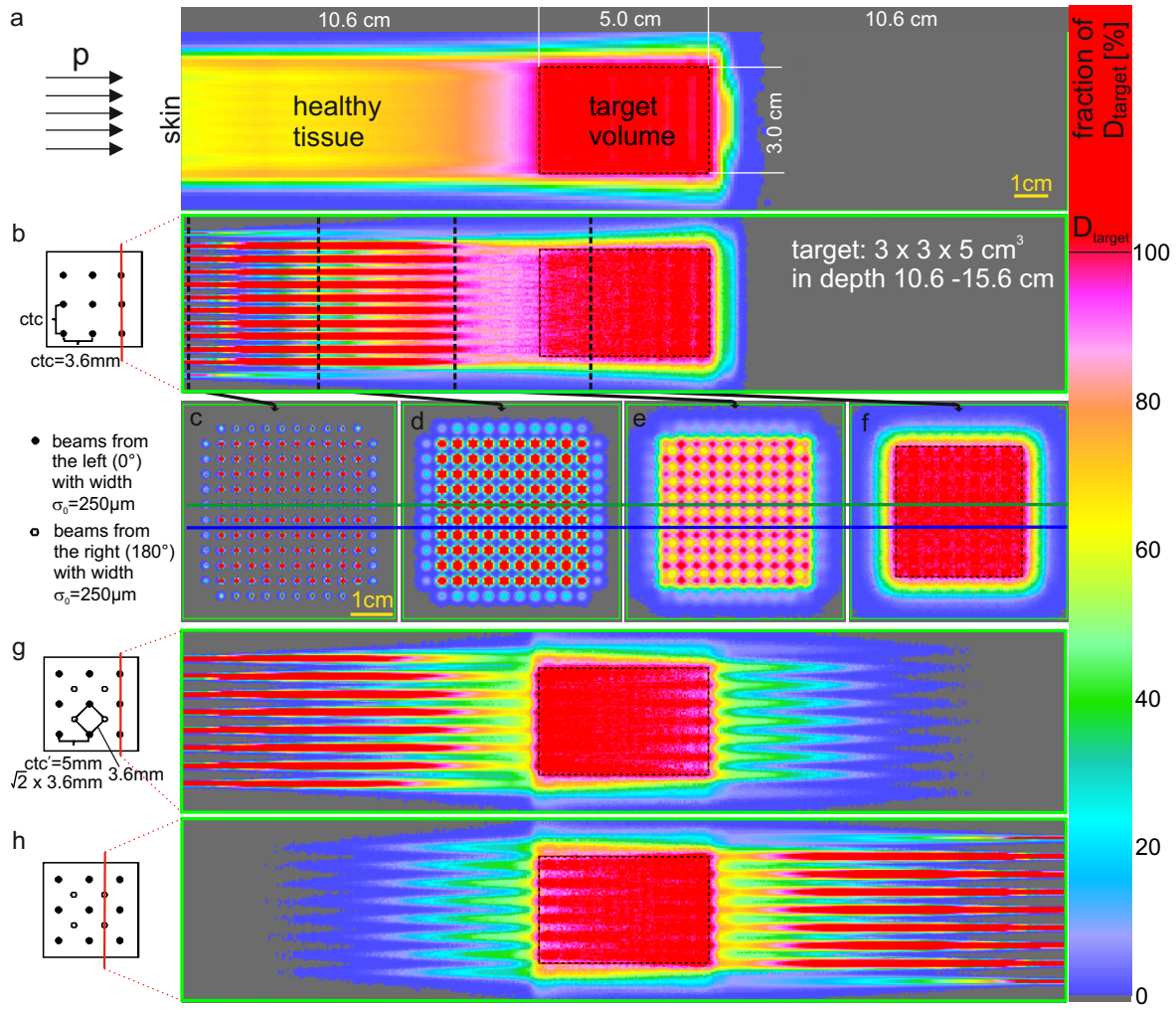

Figure 3.5: *Dose distributions for homogeneous and minibeam proton irradiation of model target 1. The target is situated at a depth of 10.6-15.6 cm and is irradiated homogeneously with a dose D_{target} (= 100 % on the color bar) by homogeneous broad beams (a) or minibeams (b) from one direction (beams from the left) or two opposite directions (g and h). The minibeams with initial sizes $\sigma_0 = 250\,\mu m$ have a center-to-center distance ctc of 3.6 mm. The dose in the minibeams is larger than the target dose, e.g. in the skin by a factor of approx. 16 (doses $\geq D_{target}$ are red on the color bar). However, the gray area in-between the minibeams receives no dose at all. Lateral dose distributions are displayed for the skin (c), 4 cm depth (d), 8 cm depth (e) and in the target volume (f). Cuts through the minibeams (green line) and in-between (blue line) are displayed in Fig. 3.6. [23]*

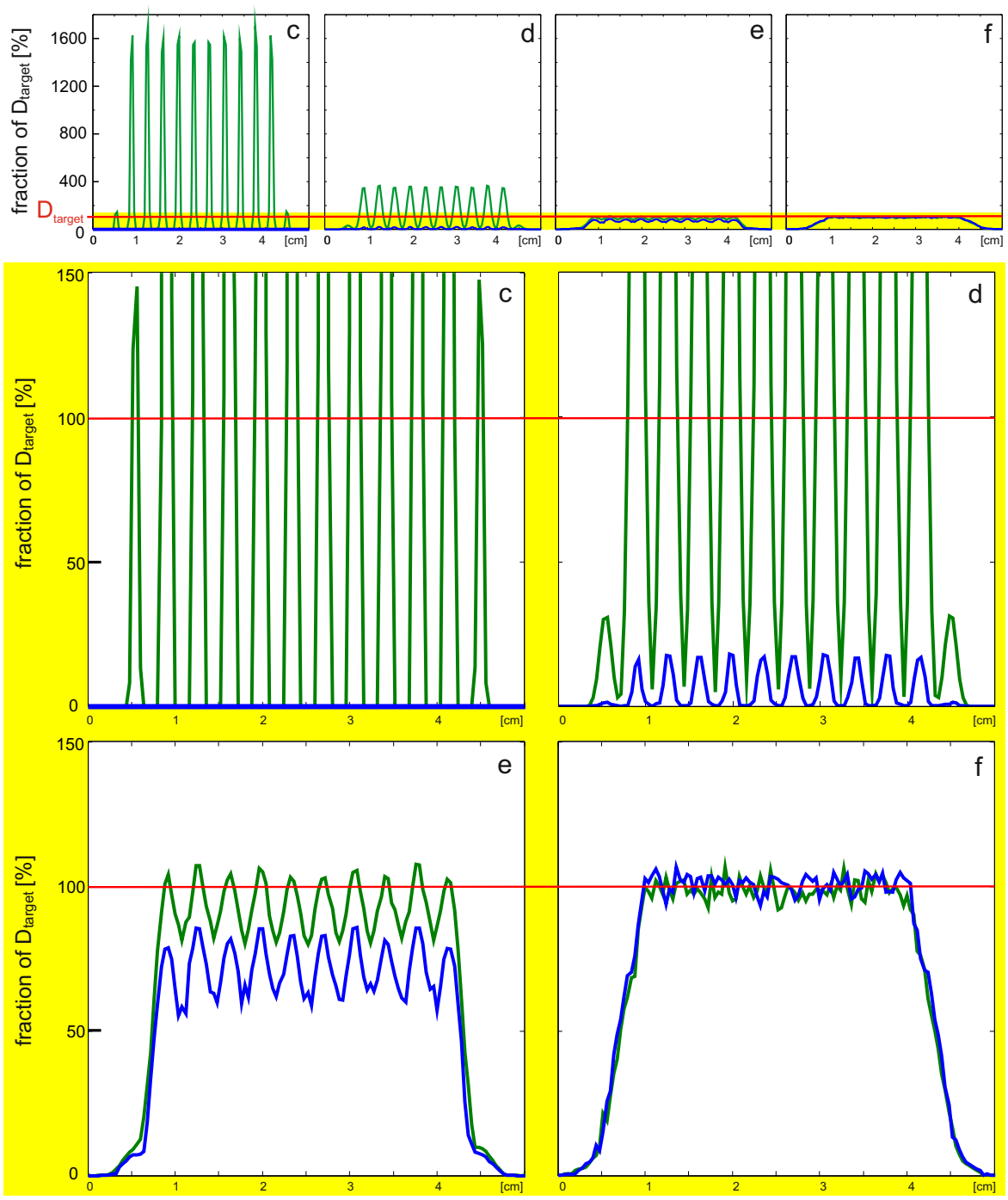

Figure 3.6: *Dose profiles for the minibeam proton irradiation of model target 1. Cuts through the lateral dose distributions of Fig. 3.5 (c-f) through the minibeams (green line) and in-between (blue line) are displayed for the complete dose scale (upper images) and enlarged for doses up to 150 % of the target dose D_{target} (yellow region). Letters are chosen as in Fig. 3.5, i.e. dose profile through the skin (c), in 4 cm depth (d), in 8 cm depth (e) and in the target volume (f).*

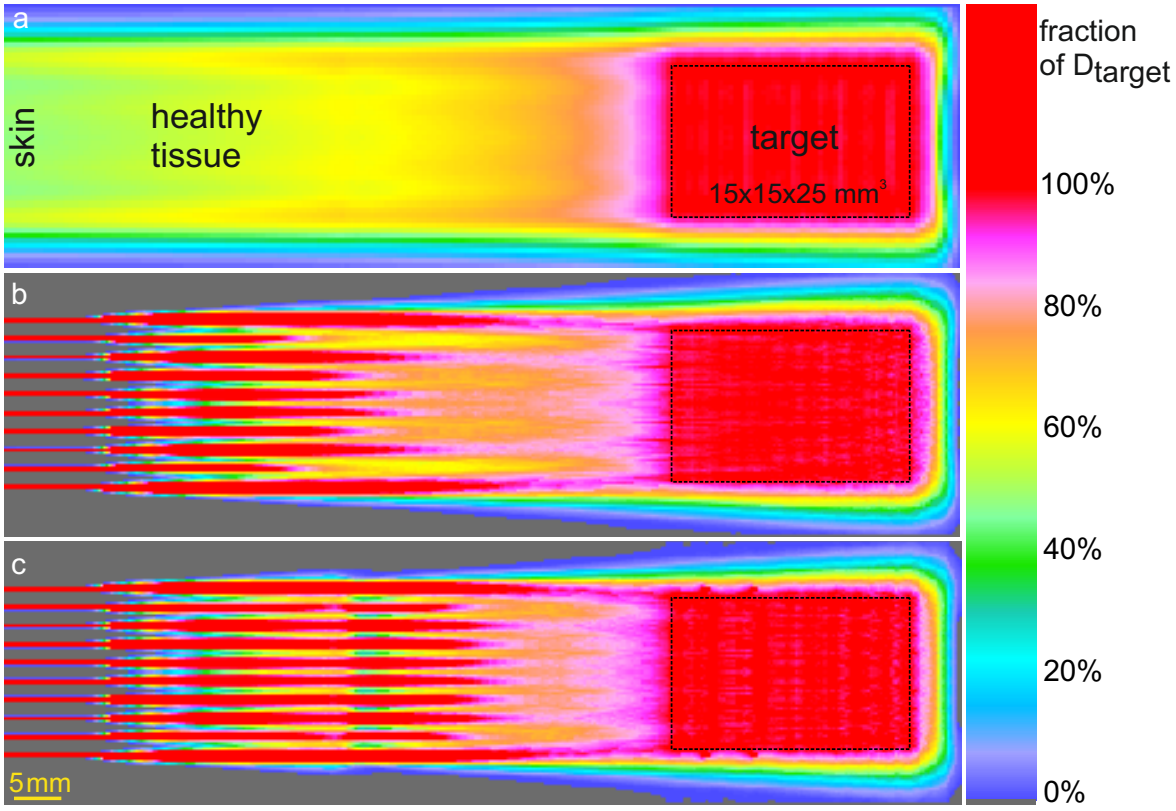

Figure 3.7: *Dose distributions for homogeneous and minibeam proton irradiation of model target 2. The target volume is situated at a depth of 7-9.5 cm and is irradiated homogeneously with a dose D_{target} (= 100 % on the color bar) by homogeneous broad beams (a) or minibeams (b, c) from one direction (beams from the left). Panel (b) shows the simulation of the minibeam scattering using the "One Gaussian" model, while panel (c) is the treatment plan using the "Two Gaussian" fit. The minibeams with initial sizes $\sigma_0 = 77\,\mu m$ (i.e. FWHM $\sim 180\,\mu m$) have a center-to-center distance ctc of 1.8 mm. The dose in the minibeams is larger than the tumor dose, e.g. in the skin by a factor of about 20-30 (doses $\geq D_{target}$ are red on the color bar). However, the gray area in-between the minibeams receives zero dose. [17]*

3.5 Conclusions

Proton minibeam radiotherapy is an implementation of spatial fractionation which is supposed to lead to normal tissue sparing in the entrance channel in front of the tumor and especially in the skin. In contrast to micro- or minibeams of X-rays, a homogeneous dose distribution can be obtained in the tumor due to lateral scattering of the protons on their way towards the tumor, leading to a merging of the initially non-overlapping minibeams into an unsegmented field in the target volume.

The simulations using LAP-CERR demonstrated the feasibility of the minibeam concept in simple models. Typical inter-beam distances which lead to a homogeneous tumor dose lie in the millimeter range, with larger possible distances for deeper-lying tumors. The (initial) size of the minibeams should potentially be as small as technically feasible to exploit the dose-volume effect. However, the (lower and upper) limits of the minibeam dimensions which are required to reduce normal tissue damage are still to be determined.

For more complex irradiation geometries (e.g. through different tissue densities), the different scattering properties have to be integrated in the treatment planning system, i.e. proton straggling in different materials needs to be known with much higher accuracy than for conventional planning. Furthermore, the relationship between proton scattering and electron densities of different tissues, as measured in CT images, needs to be determined. For complex tumor shapes, the layer (of the body) with the largest tumor dimensions or with the closest proximity to the skin has to be chosen for optimization of the minibeam dimensions, or the *ctc* distances might even be adapted individually for different parts of the target volume.

The experimental application of the minibeam method in two different skin models to examine side effects in comparison to conventional homogeneous irradiation will be presented in the next chapters.

Chapter 4

Proton irradiations at SNAKE

All experimental examinations of the proton minibeam concept were performed at the ion microprobe SNAKE in Munich, where different-sized micro- and minibeams and homogeneous irradiation fields can be generated for the irradiation of in-vitro and in-vivo skin models. The utilized proton energy of 20 MeV (with an associated range of 4.6 mm) is much lower than typical energies applied in radiotherapy of up to 250 MeV, but leads to the same skin responses (at a certain radiation dose), as the size of the minibeams in the skin is basically constant and not significantly affected by the increased scattering of low energy protons compared to higher energy protons.

4.1 The ion microprobe SNAKE

The Munich ion microprobe SNAKE [75], which is installed at the 14 MV Tandem accelerator in Garching, can be used for material analysis via hydrogen microscopy [76] as well as for radiation biology experiments. Irradiation of single defined cell nuclei and of more complex samples like skin tissues or even animals with single or counted ions offer a wide range of options for radiobiology research [17, 23, 77–81]. SNAKE provides protons and heavier ions with a wide range of energies (protons up to 28 MeV, heavy ions up to 300 MeV), which can be focused to a sub-micrometer spot size, allowing a defined dose deposition in the user-defined irradiation field [26, 44].

The SNAKE beamline for biological experiments (without intermediate focus) is displayed in Fig. 4.1. Ions are generated with a negative charge of q = - e and accelerated toward the positively charged terminal in the center of the van-de-Graaff accelerator (maximum terminal voltage 14 MV), where they pass a carbon stripper foil [82], stripping electrons from the outer shells in a statistic manner, which results in different positive charge states. Consequently, they are repelled from the positive terminal and accelerated a second time by the terminal voltage. The following 90°analyzing

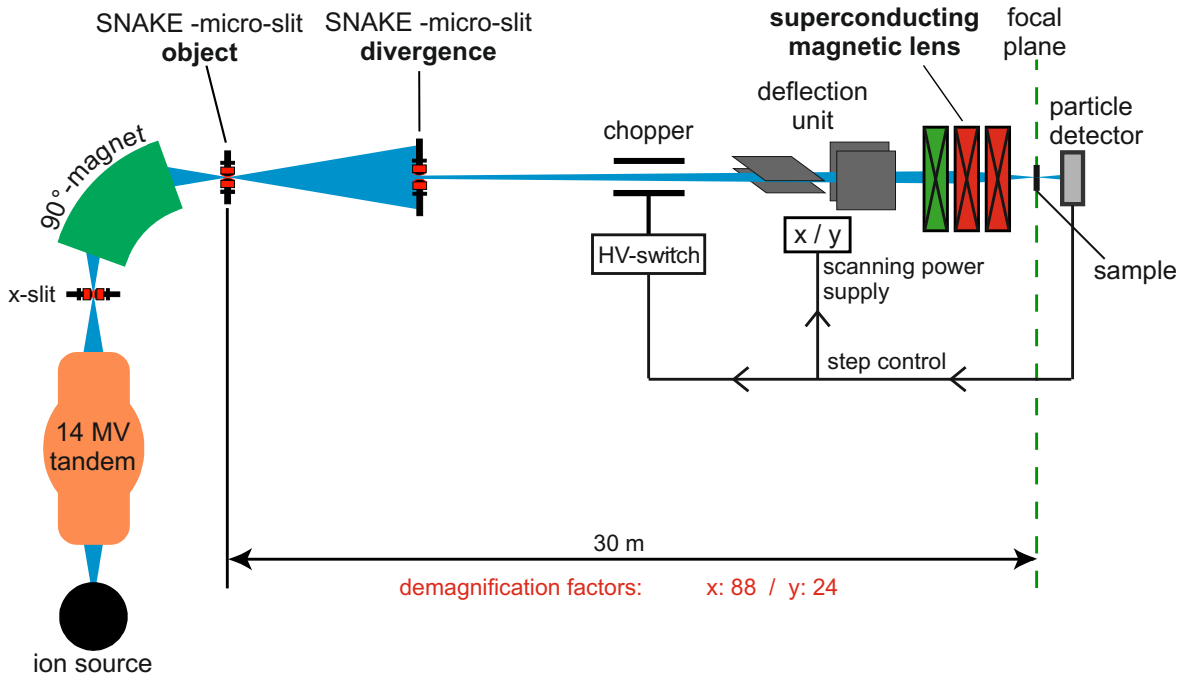

Figure 4.1: *SNAKE beamline for microbeam irradiations: Ion beam preparation with slit systems and superconducting multipole lenses to a spot size of approx. 500 nm. Detection of the single ions after traversal of the sample (positioned in the focal plane) to control chopper (beam switch) and electrostatic scanning plates (lateral beam position). [77, 84, 86]*

magnet transmits only ions with the desired magnetic rigidity (ratio of momentum and charge ($p/q = B \times r$)), producing a monoenergetic beam of the desired nuclide and charge state. The lateral position of the beam can be shifted by an electrostatic scanning unit, which allows for the preparation of various mm-wide irradiation patterns. A helium-cooled triplet of superconducting multipole lenses [83] can be used to focus the ion beam in the focal plane, with a demagnification of 1/100 in x and 1/25 in y, leading to a beam spot of less than 1 µm size [84]. The "object" microslit system in the focal plane of the bending magnet defines the object for demagnification and confines the ions within a diameter of 10-30 µm. Together with the "divergence" slit system that limits the divergence of the beam to about ±10 µrad its relative energy spread is reduced to 10^{-5}. Behind the helium cryostat, where the ions leave the vacuum through a 7.5 µm Kapton foil (beam exit nozzle), the samples can be positioned in the focal plane of the lens for irradiation. [84–86]

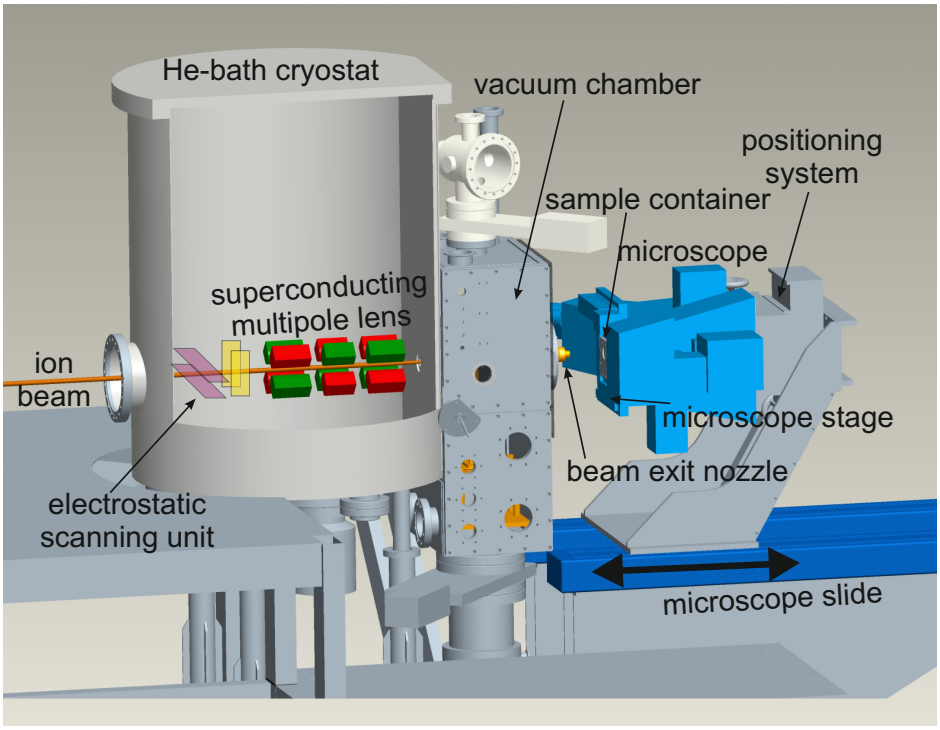

Figure 4.2: *CAD drawing of the SNAKE irradiation setup: The superconducting multipole lenses are situated in a helium bath cryostat together with the electrostatic scanning unit. The ion beam leaves the vacuum through a 7.5 µm thick capton foil at the beam exit nozzle. The samples in specially designed containers are mounted onto the sample holder of a 90° tilted fluorescence microscope. The microscope can be moved along the beam axis via a motorized slide and the sample can be moved orthogonal to the beam axis by the microscope stage. From [84].*

4.2 Irradiation setup

The irradiation setup, developed in two PhD theses ([84, 87]) is depicted in Figure 4.2. The fluorescence microscope (Zeiss Axiovert 200M, Carl Zeiss AG, Oberkochen) installed behind the beam exit nozzle can be used for positioning and moving the irradiation sample in all three directions, allowing direct contact to the exit nozzle, if required for high beam resolution. The samples are mounted to the microscope stage in specially designed containers, which differ significantly between cell or tissue samples or even mice (cf. section 5.2 and 6.4). During irradiation, beam exit nozzle and container can be heated to 37 °C allowing long-term live cell observations as well as heat control for living, anesthetized animals. Behind the sample, a BC-418 plastic scintillator is installed for ion detection together with a photomultiplier tube (PMT; Hamamatsu R7400P), which is positioned in the objective revolver of the microscope. The PMT

signal triggers a high voltage chopper which deflects the beam from the sample after the desired number of ions have reached the scintillator (single ion preparation), allowing the delivery of a defined, arbitrary dose to the sample. [86]

The detector signal is also used to control the deflection unit which enables the fast scanning of the beam via electrostatic scanning plates. The maximum deflection is limited by the electric rigidity to about $500\,\mathrm{x}\,500\,\mu\mathrm{m}^2$. Larger irradiation fields can be stitched together by mechanic movement of the sample in the microscope stage, with a precision better than $3\,\mu\mathrm{m}$ [26].

4.2.1 Homogeneous proton irradiations

For the generation of homogeneous irradiation fields with randomly applied ions, a function generator can be connected to the electrostatic deflection unit to actively scan the ions to a rectangular field of up to several $100\,\mu\mathrm{m}$ edge length. These can be stitched together by moving the sample in the microscope stage to produce homogeneous fields of several mm size and rectangular or quasi-circular shape, but also to irradiate rectangular spots (later called minibeams) in defined distances (cf. Fig. 4.3).

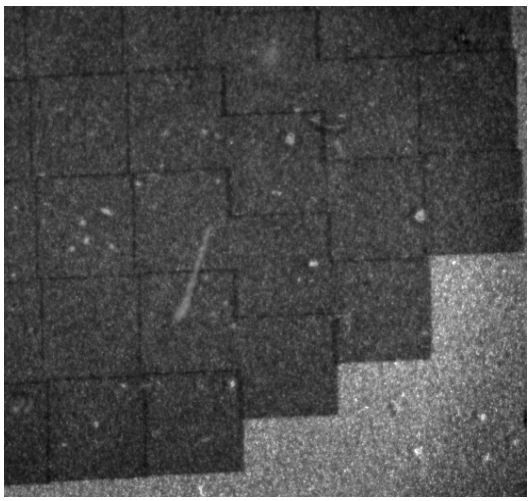

(a) *Generation of a homogeneous irradiation field by stitching 500 µm scan fields (moving the sample in the microscope stage).*

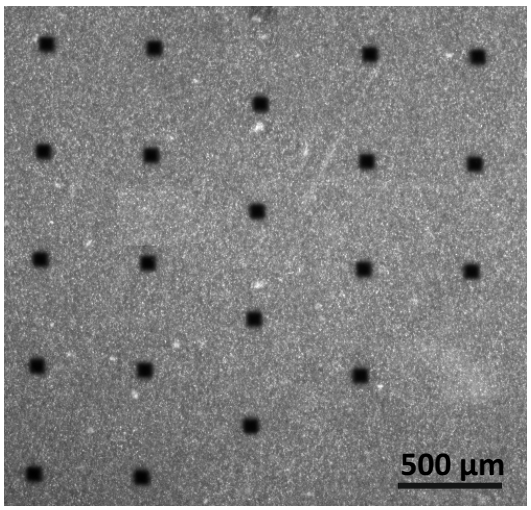

(b) *Minibeam irradiation with $50\,\mathrm{x}\,50\,\mu m^2$ spots in $500\,\mu m$ distance.*

Figure 4.3: *Homogeneous field and minibeam irradiation, visualized using radiochromic Gafchrom films.*

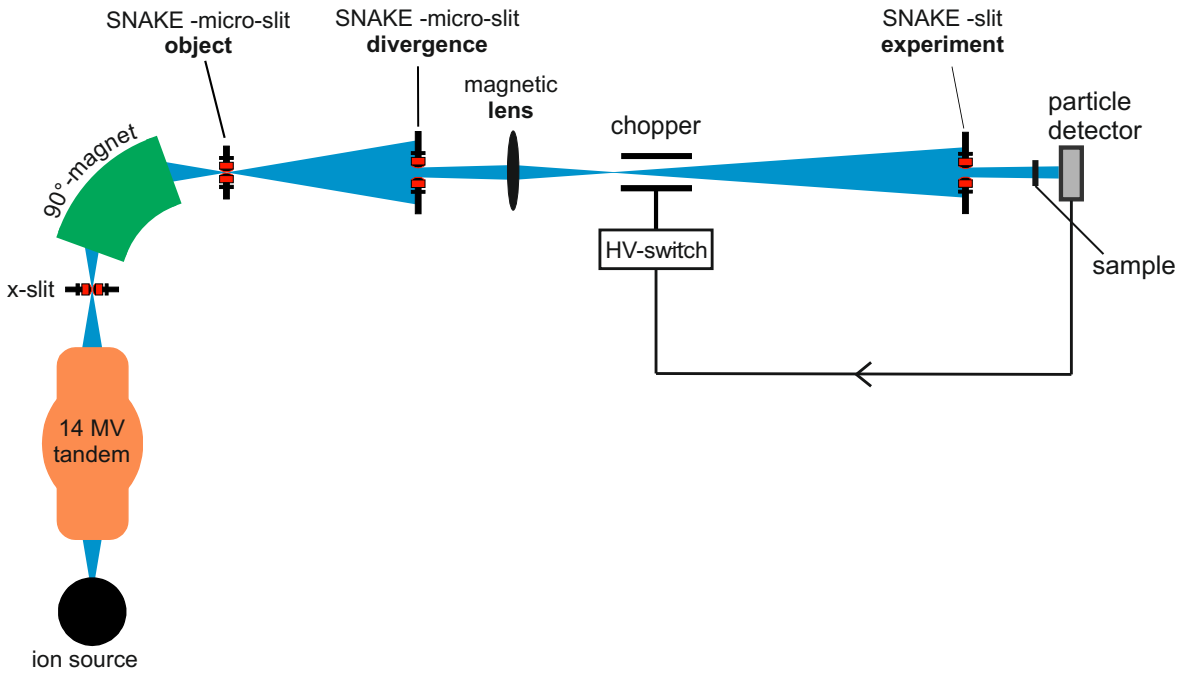

Figure 4.4: *SNAKE beamline for homogeneous irradiations: Ion beam preparation with slit systems and an additional intermediate focus, but without the multipole lenses, allowing field sizes of several mm. Detection of the single ions behind the sample to define the applied dose and to control the chopper (beam switch) as for microbeam irradiations (Fig. 4.1).*

An alternative way to generate mm-sized homogeneous fields is by switching off the focusing lens and cutting down the unfocused beam by slit systems. For fields larger than approximately 9 mm diameter a different photomultiplier with a larger active area has to be mounted behind the sample instead of the pre-installed one and a larger beam exit nozzle has to be mounted. However, as the four object slits (of which 2 define the x slit and the other 2 the y slit) are shifted along the beam direction, there is an angle-dependence of the beam intensity which leads to an inhomogeneity in the dose along the x and the y direction. Introducing an intermediate focus by a magnetic lens leads to an angular magnification, such that the phase space at the object which is accepted at the experiment slits has smaller angles and thus reduces the dose variation in x and y ($\sim \pm 1\,\%$ between center and edges of a 7x7 mm^2 field) (cf. Fig. 4.4).

4.2.2 Proton minibeam irradiations

Using the electrostatic scanning plates, only square or rectangular minibeams can be generated. These can be set on a rectangular matrix with defined distances by moving the sample with the microscope stage. In order to produce Gaussian-shaped minibeams, the focused microbeam can be widened to the desired size by adding an aluminum sheet with defined thickness behind the beam exit nozzle which scatters the ions to larger angles and reduces their energy. This nearly Gaussian angular distribution can be translated into a lateral spread with Gaussian shape in an air-gap between the aluminum sheet and the sample. The width of the beam can be adjusted by the length of the air-gap, i.e. the distance between Al and sample, which can be changed by moving the sample away from the exit nozzle (by a distance d) with the microscope slide (cf. Fig. 4.5) [25].

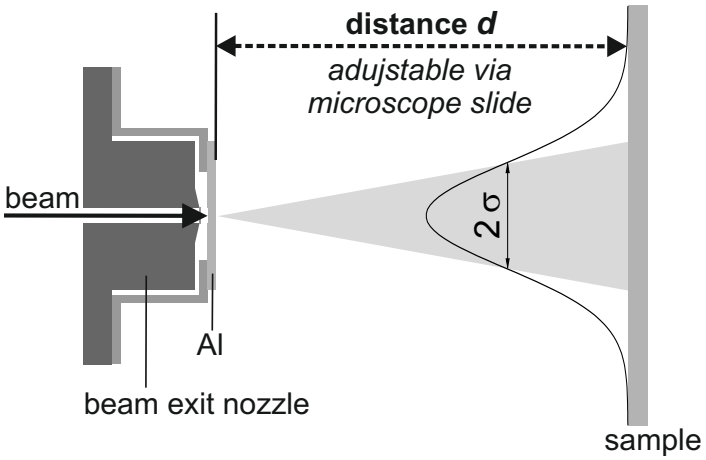

Figure 4.5: *Generation of Gaussian-shaped minibeams: Mounting of a 200 µm aluminum sheet directly behind the beam exit nozzle to generate minibeams with Gaussian distribution of variable size σ, by adjusting the distance d between sample and Al. [25]*

In this work, 200 µm aluminum was used to produce proton minibeams of Gaussian shape with different widths, e.g. $\sigma \approx 260\,\mu m$ after a $d = 19\,mm$ air-gap. Calibration curves for various distances d between aluminum sheet and sample were recorded using radiochromic Gafchrom films at the position of the sample in three independent experiments and beam times. The number of protons had to be adapted to the sensitive range of the films. The gray values of the two-dimensional irradiation patterns on the films were calculated into radiation doses using a dose calibration curve (cf. [88]) and were fitted using a 2D Gaussian (Fig. 4.6).

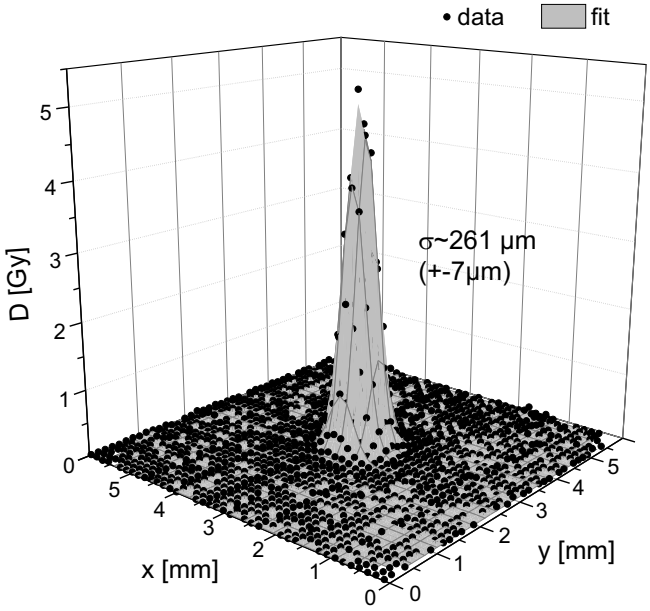

(a) *Minibeam dose distribution 19 mm behind the Al (measurement and 2D Gaussian fit). The dose had to be reduced to 1/3 of the experiment dose to fit the sensitivity range of the film.*

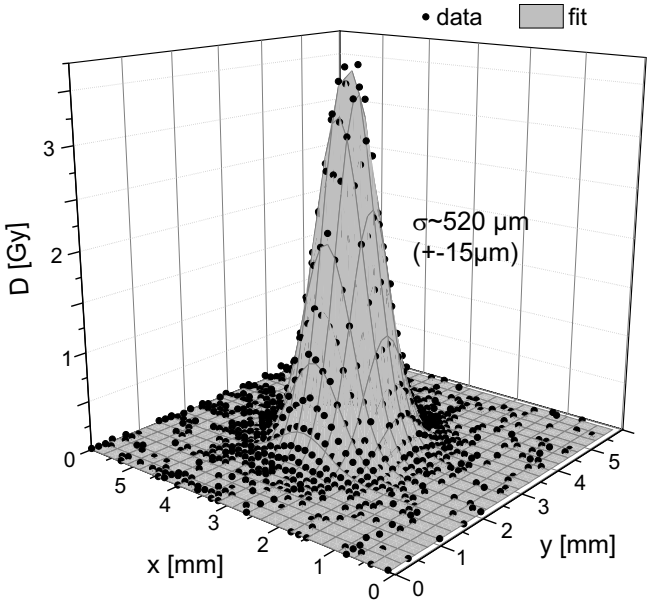

(b) *Minibeam dose distribution 38 mm behind the Al (measurement and 2D Gaussian fit).*

Figure 4.6: *Dose distributions of Gaussian-shaped minibeams, measured with Gafchromic films positioned 19 mm (a) and 38 mm (b) behind the 200* µm *Aluminum sheet.*

The width σ of the Gaussian-shaped proton distributions is plotted versus the corresponding air-gap d in Figure 4.7, showing a linear dependence with an angle divergence m of approximately 13 mrad ($\sigma = m \times d + t$, with values for m and t in Table 4.1). The different offsets t in the three independent experiments are probably due to systematic uncertainties from the definition of the zero-position ($d = 0$). To account for the energy loss in the aluminum, protons were accelerated to 21 MeV for these experiments to obtain the same energy of 20 MeV at the sample as in all other experiments of this work (cf. SRIM calculations [29]).

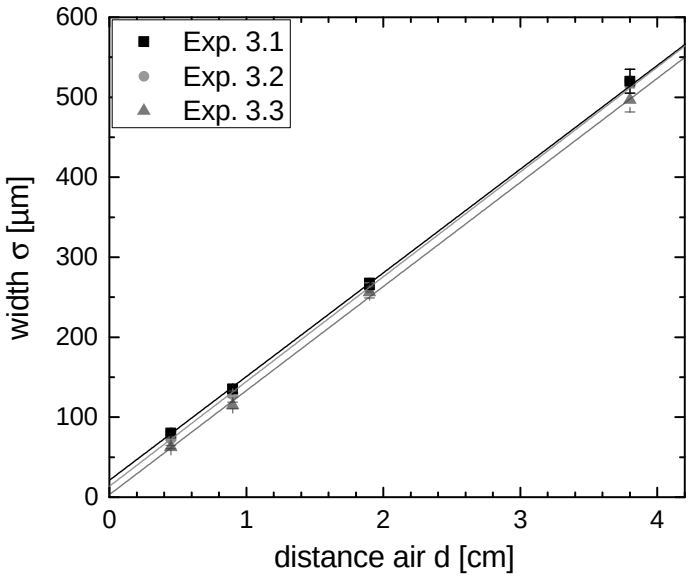

Figure 4.7: *Calibration curve for beam widening: Width of the proton distributions measured at different distances behind the aluminum sheet: Gaussian distributions at 4.5, 9, 19 and 38 mm behind the aluminum were analyzed with Gafchromic films in three independent experiments (Exp. 3.1-3.3). [25]*

Experiment	**3.1**	**3.2**	**3.3**
m	(13.0±0.4)x10^{-3}	(13.1±0.4)x10^{-3}	(13.6±2.8)x10^{-3}
t [μm]	21.1±2.8	13.6±2.8	3.1±2.8

Table 4.1: *Fit parameters of the calibration curves for beam widening in Fig. 4.7 (three independent experiments). The linear dependence of the beam width σ on the distance d between sample and aluminum shield is given by $\sigma = m \times d + t$.*

4.3 Experimental procedure

Before any sample irradiation, the beam has to be prepared for the microbeam mode or the unfocused homogeneous mode, respectively. Therefore, a scintillation crystal (CsI(Tl) or YAG) is mounted at the irradiation site in the focal plane of the microscope, allowing the visualization of the beam. For microbeam preparation, the currents through the superconducting lens are varied such that the beam is focused optically to sub-micrometer dimensions. The scintillator is also utilized for the calibration of the electrostatic scanning plates and the verification of the actual zero point beam position [84, 85]. To prepare the square minibeams, the scintillator is used to determine the beam dimensions, which can be adjusted via the voltage of the function generator controlling the scanning unit. When preparing homogeneous fields without the superconducting lens, the scintillator crystal also serves to measure the exact field size, which can be adjusted by the microslit system directly before the lens.

For irradiation, the samples are placed onto the microscope table and the desired area of irradiation is selected using phase contrast microscopy or simply by determining the center of the sample. Typically, the sample is positioned in contact with the beam exit nozzle and the photomultiplier-scintillator detector in the objective revolver is positioned behind the sample for particle counting.

For irradiation fields larger than approximately 500x500 μm^2, the Zeiss AxioVision Visual Basics Application plugin "scan field extension" (German: Scanfelderweiterung) can be used, which controls the microscope stage in order to stitch together rectangular or quasi-circular irradiation fields of adjustable scan field and total field size.

Quality assurance of the irradiations is additionally performed using Gafchromic films (EBT2 or EBT3) to validate absolute dose (for comparison with counted particles per area) and beam size and shape. Irradiated areas on the film darken corresponding to the applied dose and can be read out using conventional flat bed scanners and a reference curve (cf. [88]).

Chapter 5

Study in an in-vitro human skin model

First experimental investigations on the effects of micro- and minibeam irradiations in comparison to conventional homogeneous broad beam irradiations were undertaken in an in-vitro human skin model. These skin tissues are built up of epidermis and dermis just like real human skin and are therefore suitable for the detection of genetic damage and acute responses following exposure to ionizing radiation.
Different shapes (square vs. Gaussian), sizes (10 µm to approx. 1 mm) and distances (0.5-1.8 mm) of micro-/minibeams were analyzed and compared to homogeneous irradiations of the skin. Experimental setup and results have already been published in Zlobinskaya et al. 2013 [23] and Girst et al. 2015*b* [25], where irradiations were still termed "microchannel irradiations" instead of minibeam irradiations. The comparative study of X-ray and proton micro-/minibeam irradiations in the same human skin model, conducted at the European Synchrotron Radiation Facility (ESRF, Grenoble, France) and at SNAKE is published in Girst et al. 2015*a* [24], but only the proton data will be presented in this work.

5.1 Skin model and culture

The skin model used for this study is the full-thickness EpiDermFT^{TM} EFT400 from MatTek Corporation, Ashland, MA, USA (cf. [23, 89]). The three-dimensional human skin model has a diameter of 1 cm and a thickness of 600-900 µm and consists of an epidermal and a dermal layer (see Fig. 5.1), like human skin. The epidermis terminates with the visible stratum corneum (cornified layer), followed by stratum granulosum, stratum spinosum and the highly-proliferating stratum basale (basal layer), just like in in-vivo skin (cf. [90]). The dermal layer underneath is composed of a collagen matrix

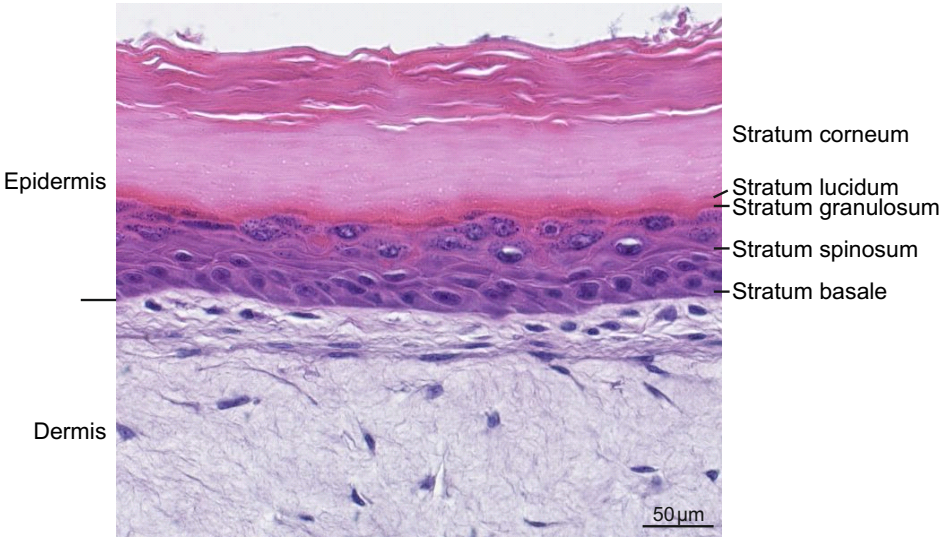

Figure 5.1: *Histological section of the skin model EpiDermFT^{TM}.*

containing fibroblasts. The epidermal keratinocytes and the dermal fibroblasts are derived from normal human, genetically unmodified cells from neonatal skin/foreskin or adult skin. The skin model is metabolically and mitotically active, with similar morphological and growth characteristics as in-vivo skin [89]. Therefore, the model is well suited for analyses of proliferation, genetic damage and production of inflammatory proteins (cytokines) after irradiation with protons or photons.

The tissue samples are cultured on special cell culture inserts (Costar Snapwell single well tissue culture plate inserts) with the dermal layer lying on a microporous membrane (Fig. 5.2). This membrane is permeable to nutrients from the culture medium and allows nutrition of the skin by diffusion, unlike in in-vivo skin where nutrients are supplied via the blood. The skin samples are shipped on medium-supplemented, agarose gels at 4 °C [89]. Directly after arrival, the cell culture inserts are placed in 6 or 12-well plates and supplied with 2 ml New Maintenance Medium (NMM, MatTek

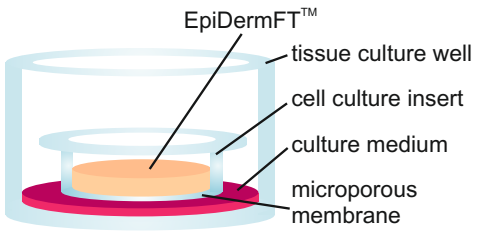

Figure 5.2: *Skin sample culture: EpiDermFT^{TM} cultured in a cell culture insert in a 6 or 12-well, supplied with culture medium.*

Corporation, Ashland, MA, USA), with 10 µl/ml fungin added against mold formation. At 37 °C and in a humidified atmosphere of 5 % CO_2 the skin can be cultured up to 14 days, changing the medium every 24 or 48 hours [89].

5.2 Irradiation modes

For irradiations at SNAKE, the cell culture inserts were placed in specially-designed irradiation containers and positioned in an upright position directly in front of the beam exit nozzle (max. distance of 0.1 mm), with the dermis facing the beam. The containers consist of two stainless steel plates, fitting the size of the sample holder at the microscope stage (68 x 93 x 5.4 mm^3, Fig. 5.3). A 6 µm Mylar foil is stretched and fixed onto the first plate (lid), covering the circular hole. A second Mylar foil is glued to the outer face of the bottom plate to protect the insert, which is placed in the cut-out. Under the laminar flow, the skin sample in the culture insert is positioned on the bottom plate, all medium is removed from the skin and the lid is screwed to the bottom. The closed design is meant to avoid drying and contamination [23, 79]

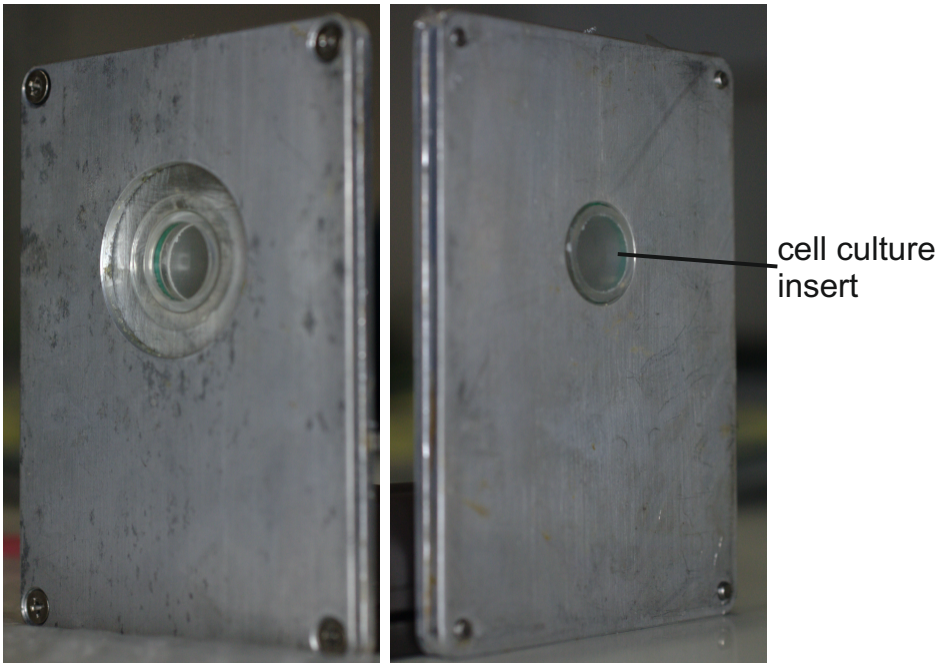

Figure 5.3: *Skin sample holder: EFT400 skin samples cultured in cell culture inserts (Fig. 5.2) are placed between two stainless steel plates (6.8 x 9.3 cm^2) with circular holes for the inset, protected by Mylar foil.*

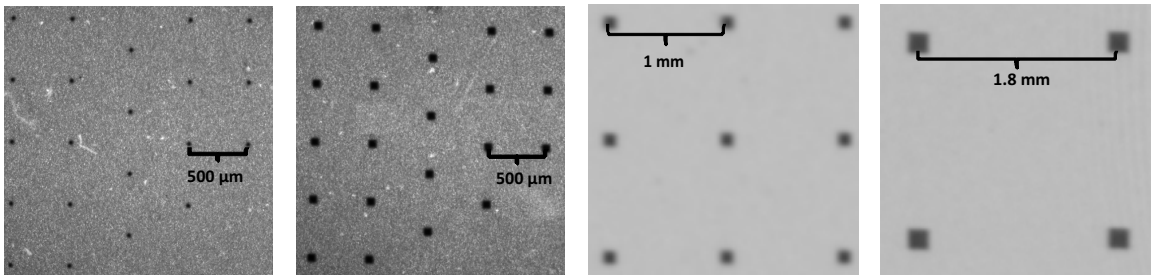

10x10	50x50	100x100	180x180
10 x 10 µm² MB	50 x 50 µm² MB	100 x 100 µm² MB	180 x 180 µm² MB
500 µm distance	500 µm distance	1 mm distance	1.8 mm distance
1 180 136 p / MB	1 180 136 p / MB	4 720 544 p / MB	15 294 563 p / MB
5000 Gy / MB	200 Gy / MB	200 Gy / MB	200 Gy / MB
0.04 %	1 %	1 %	1 %

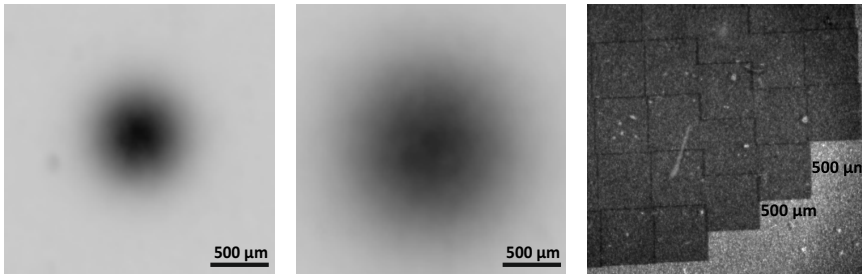

WB	OB	HF
widened MB (σ ~ 260 µm)	overlapping MB (σ ~ 520 µm)	homogeneous field
1.8 mm distance	1.8 mm distance	
15 294 563 p / MB	15 294 563 p / MB	1 180 136 p / 500x500µm²
		2 Gy
25 %	38 %	100 %

Figure 5.4: *Visualization of all applied irradiation modes with corresponding abbreviations and descriptions. The last line represents the fraction of the skin receiving a dose ≥ the average dose of 2 Gy. MB minibeams, p protons*

An overview of all utilized irradiation modes is given in Fig. 5.4. The first microbeam irradiations were performed with beams of 10x10 μm^2 and 50x50 μm^2 size, using the same inter-beam distances of 500 µm and a total (close to) circular irradiation area of 16.75 mm^2 in both cases (Exp.1). This meant a coverage of 0.04 % and 1 % of the area with doses of 5000 and 200 Gy, respectively. In total, 79,069,112 counted 20 MeV protons (LET ≈ 2.66 keV/ µm) were used, resulting in the same average dose of 2 Gy as in the homogeneous case. The dose uncertainty is approximately 4 % and

arises mainly from the uncertainty of the field size (approx. 2 % in each dimension) and the accuracy of the LET value (1-2 % [91]). Counting uncertainties due to pileup events in the scintillator detector (< 0.5 %) and from protons undergoing large-angle scattering within the skin sample so that they did not reach the detector (< 0.01 %) also contribute to the total dose uncertainty (cf. [23]). Valley dose measurements using Gafchromic film (Fig. 5.5) revealed that for the 50x50 mode 93 % of the irradiation area received a dose ≤ 1 % of the mean dose (i.e. ≤ 0.02 Gy). In order to get valley doses in the sensitive range of the films, 50 times the number of protons usually delivered to the 50x50 µm^2 had to be applied (i.e. a mean dose of 100 Gy). [23]

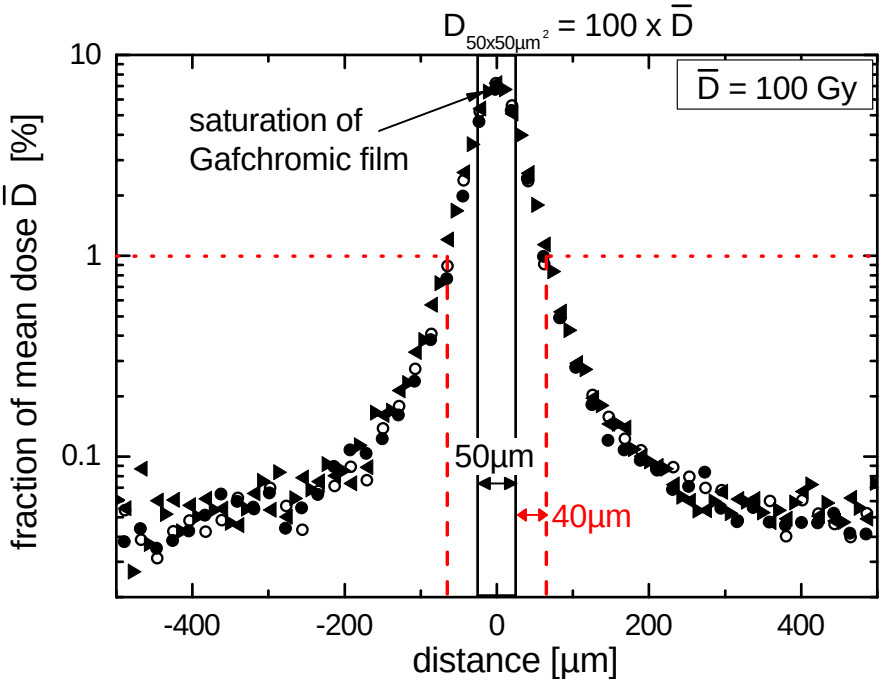

Figure 5.5: *Dose distribution of 50 x 50 µm^2 minibeam irradiation. Gafchromic film was irradiated on two 50 x 50 µm^2 fields with 50 times the number of protons used in the skin experiments (i.e. 59,006,800 protons) to investigate valley doses. For both fields, x- and y-projections of the dose values were determined and displayed as fractions of the mean dose (x: full and open circles, y: triangles). The dose fall-off below 1 % of the mean dose (red dotted line) occurs at a distance of approximately 40-50 µm from the border of the irradiated field (red dashed line) (scanner resolution ~ 21 µm, film polymers ~ 20 µm). This means that ~ 93 % of the area contains less than 1 % of the average dose, i.e. less than 0.02 Gy in the skin experiments. The saturation of the Gafchromic film within the irradiated 50 x 50 µm^2 field, where the dose is 100 times the mean dose, is indicated by an arrow. [23]*

In the next experiments (Exp.2), the minibeam sizes were enlarged to 100x100 μm^2 and 180x180 $\mu m^{2(1)}$ and center-to-center distances were chosen such that again 1 % of the area was irradiated, meaning 1 mm and 1.8 mm, respectively. This was the largest distance compatible with the size of the skin samples, so that still up to 5x5 minibeams could be fit onto the sample. The average dose was again chosen to 2 Gy so that results could also be compared to earlier findings. For biological endpoints using the complete skin tissue (e.g. cytokine expression), the same total number of protons were applied to the skin in all irradiation modes, while for endpoints using only a punched area of the tissue within the irradiated field, the average dose in the punched field was held constant.

In order to simulate the widening of the minibeams with increasing depth in tissue on the path towards the tumor, beam dimensions were systematically enlarged from 180 µm to 1.2 mm FWHM, while keeping the same inter-beam distances of 1.8 mm (Exp.3). Even though the tissue in the intermediate region between skin and tumor might be different from skin with respect to radiosensitivity (skin is early-reacting), we still decided to utilize the previously used human skin model as representative of normal tissue (instead of e.g. lung or muscle tissue), as only this allowed the direct and quantitative comparison of the effects of different minibeam sizes. Gaussian shaped minibeams of the desired dimensions were generated by spreading a focused proton microbeam in 200 µm Aluminium and leaving a defined distance between Al sheet and sample, as described in detail in Chapter 4.2. The thus produced minibeams had a size of $\sigma \approx 260$ µm ("widened beams", WB), as in 1/3 of the depth of the model tumor 1 ($d_{tumor} = 10.6$-15.6 cm, see Chapter 3.4), and 520 µm ("overlapping beams", OB), as at 2/3 of the tumor depth, and were analyzed in comparison to the square minibeams of 180x180 μm^2 size (called 180x180* due to the Aluminum) and a homogeneous proton irradiation at 2 Gy. The number of protons per minibeam were the same for all three minibeam modes (15,294,563), but resulted in different absolute doses due to the increasing beam sizes. Also the relative fraction of the the total area irradiated with a dose equal to or higher than 2 Gy increased with minibeam size, from 11±2 % for the square beams to about 25 % and 38 %, respectively (cf. [25]). The experiments were performed in three independent beam times (Exp.3.1-3.3). [25]

(1) The results of the 180x180 μm^2 irradiation mode are published in Girst et al. 2015*a* [24] under the abbreviation "LC".

5.3 Biological endpoints

In order to evaluate acute immune responses to proton radiation in different irradiation modes, inflammatory cytokine levels in the culture medium of the EpidermFT^{TM} skin tissues, measured by standard enzyme-linked immunosorbent assay (ELISA) methods, were analyzed. Genetic damage was evaluated using the micronucleus test with cytokinesis-block and tissue viability was determined with the MTT[(2)] test.

5.3.1 MTT tissue viability test

The MTT assay is a colorimetric test for quantitative measurement of the metabolic activity of enzymes in living mammalian cells and thus a measure for viability, proliferation and cytotoxicity [92]. MTT and other positively charged tetrazolium salts have been used to identify viable cells in histo- and biochemical applications for many years [92, 93]. Upon reduction, tetrazolium salts are transformed from weakly colored or colorless substrates into purple colored formazan products. Most MTT is reduced intracellularly by enzymes of the mitochondria (succinate dehydrogenase) and the endoplasmatic reticulum (NADH and NADPH) of viable cells, but not of dead cells or tissue culture medium [92, 93]. Under defined growth conditions, dye reduction is proportional to the number of viable cells (in exponential growth phase), allowing the determination of cell viability or proliferation from the amount of reduced MTT [92, 93]. However, the produced formazan per cell depends on the level of energy metabolism, which differs between cell types and activation level, meaning that viable cells in a resting state cannot always be clearly distinguished from non-viable or dead cells [92, 93]. Thus, the assay rather measures enzyme activities related to cell metabolism, but is, nevertheless, used frequently in cancer research to investigate cytotoxic effects [93]. Therefore, the MTT test is also utilized in this work to examine the tissue reactions following different irradiation modes, interpreted as cell or tissue viability. Even though the test cannot distinguish if a value of 50 % compared to negative controls means a reduction of metabolism by 50 % in all cells or a reduction of viable cells with full metabolism to only half of the initial number, it still implies a better tolerance to the applied irradiation than to an irradiation mode yielding 30 %. For comparability of results, the following parameters should be kept constant in all experiments: MTT concentration, incubation time, number of cells (i.e. same size of tissue samples) and metabolic activity (which is e.g. temperature dependent) [92].

The utilized MTT assay was the MTT-100 kit provided by MatTek, including frozen MTT concentrate (MTT-100-CON), MTT diluent (MTT-100-DIL) and Extractant So-

[(2)] 3-(4,5-dimethylthiazol-2-yl)-2,5-diphenyl tetrazolium bromide

lution (MTT-100-EXT) for extracting the insoluble formazan crystals [89, 94]. After 48 hours of post-irradiation incubation, the tissue samples were washed twice with PBS (phosphate-buffered saline; Sigma Aldrich, Germany) and the central 3-5 mm of the irradiated area were cut using a biopsy punch. The cut samples were placed in 6-well plates with 300 µl of MTT solution per well, made from MTT concentrate and diluent according to manufacturer's instructions [94]. The plates were incubated for three hours at 37 °C and 5 % CO_2. Then the samples were transferred into fresh wells and immersed in 2 ml of extractant solution and the plates were sealed with Parafilm to avoid evaporation. Extraction of the purple formazan from the cells must take at least two hours at room temperature with gentle shaking or can be performed overnight without shaking and in the dark, as all MTT substrates are light-sensitive. After removing the samples from the wells, the extracted solution is mixed by pipetting up and down. 200 µl of each sample is transferred into 96-well plates for reading the optical density (OD) at 570 nm and 650 nm in a photospectrometer (spectrometer EL808 (BioTek)). Background absorbance at 650 nm was subtracted from ODs at 570 nm to obtain the corrected OD values. These were normalized to untreated controls to determine the viability (percentage) of each tissue sample. [23, 94, 95]

MTT testing was performed by the group of PD Dr. Thomas Schmid at the Klinikum rechts der Isar (Munich).

5.3.2 Cytokine expression detection by ELISA tests

Cytokines are small, soluble proteins which play an important role in cell signaling, especially in the immune system. They are produced by various cell types including immune cells, mast cells, endothelial cells, but also keratinocytes and fibroblasts of the skin. Cytokines participate in all aspects of immunity and inflammation, i.e. development and operation of the immune system, cell proliferation, differentiation, recruitment and activation, and regulation of interactions with extracellular matrix proteins [96]. They are mediators of local and distant communication between cells, tissues and organs. Therefore, cytokines are also involved in the response of skin to ionizing radiation and closely related to acute and chronic radiation-induced skin toxicities; immediately after exposure, a cascade of cytokines is initiated, persisting over all stages of the cutaneous radiation syndrome and leading to late radiation damage [96]. The most important cytokines in the radiation response of skin cells are interleukins IL-1, IL-6 and IL-8, tumor necrosis factor TNF-α and transforming growth factor TGF-β, but also chemokines such as eotaxin [3, 96, 97]. Matrix metalloproteases (MMP) are enzymes which degrade essential parts of the basal membrane and the extracellular matrix, stimulated by mediators like IL-1, TNF and TGF-β [96, 98]. They are involved

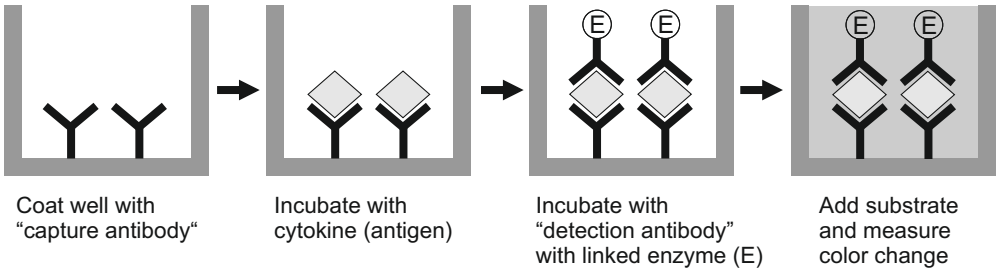

Figure 5.6: *Schematic illustration of the double antibody “sandwich” ELISA for cytokine detection: The wells of a microtiter plate are coated with a known amount of “capture antibody”. In a second step, the (diluted) sample with the unknown cytokine concentration is added and incubated. After removal of unbound cytokines in a washing step, the plates are incubated with the “detection antibody” with the linked enzyme. Addition of a substrate, which reacts with the enzyme, leads to a measurable color change (cf. [99]).*

in the migration of fibroblasts and keratinocytes and increased levels of MMP are often found in chronic wounds [98]. As no visual inflammatory response such as reddening or blistering can be induced in the in-vitro skin model EpiDermFT^{TM}, cytokine release into the culture medium was used as alternative measure for acute inflammation after different irradiation modes. Interleukin IL-6, TGF-β and Pro-MMP1 were chosen as representatives for radiation-induced and up-regulated inflammatory proteins and quantified in the culture medium using commercially available ELISA kits (R&D systems, Minneapolis, MN) [23].

The enzyme-linked immunosorbent assay ELISA is an antibody-based detection procedure to qualitatively or quantitatively determine the abundance of proteins or other antigens, based on an enzymatic color change [100]. ELISA was introduced in the 1970s and is the standard method to measure cytokines [99]. In an indirect, double antibody “sandwich” ELISA (see Figure 5.6), the “capture antibody” is attached to the bottom of each well of a microtiter plate to specifically bind the antigen (cytokine of interest), while the second, enzyme-linked “detection antibody” also binds to the antigen (at a different epitope to avoid interference) and allows detection and quantification when an added substrate (e.g. H_2O_2 plus tetramethylbenzidine) is converted by the enzyme into a color signal [99]. Absorbance (here: at 450 nm), which is proportional to the amount of bound antigen, can be read using a microplate reader (spectrometer EL808 (BioTek)), and quantified on the basis of calibration curves with known concentrations [23]. Depending on the approximate protein concentration in the medium (pre-analyzed in dilution series), samples collected every other day after

irradiation had to be diluted with MNN medium to fit the sensitive range of the assay. Between each binding step, plates had to be cleaned using the supplied Wash Buffer (buffered surfactant with preservatives; R&D systems) to remove unbound antibodies and proteins. ELISA can only measure one cytokine at a time and is largely dependent on kits' quality and operator skills, so in order to reduce further systematic errors, all tests were performed by Dr. Olga Zlobinskaya using the DuoSet kits of the same manufacturer (R&D systems).

5.3.3 Genetic damage detection by the micronucleus test

Due to higher survival rates of cancer patients from improving treatment options, the risk of developing radiation-induced secondary cancers is gaining increasing importance, especially for young patients [101]. A common method for determining genetic damage as a measure for cancer risk is the in-vitro micronucleus (MN) test [102]. The assay detects chromosome damage or abnormalities caused for instance by ionizing radiation or carcinogenic chemicals. Mis- or unrepaired double-strand breaks in the DNA or defects in the spindle can cause chromosome rearrangements, breaks or even loss of whole chromosomes [102, 103]. This can lead to the formation of small, interphase-like nuclei termed "micronuclei", when these chromosomes or fragments without centromeres (acentric fragments) are not incorporated into the two daughter nuclei during mitosis, but are enclosed in their own nuclear envelope [102, 104, 105]. Obviously, this can only occur when cells containing acentric fragments and/or whole chromosomes which are unable to move to the spindle poles, undergo nuclear division. In order to identify the cells that have undergone only one division, the cytokinesis-block (CB) method has been established: cells having completed one nuclear division are prevented from cytoplasmatic division by the use of cytochalasin-B (cyt-B), an inhibitor of microfilament assembly [102, 104]. Therefore, they can be recognized from their binucleated appearance (see Fig. 5.7, lower left image). Cells that should not be scored are multinucleated cells, apoptotic or necrotic cells, and cells without intact nuclear or cytoplasmatic membranes and where the two nuclei are overlapping or not approximately the same size or staining intensity [102, 105]. The criteria of Fenech for scoring micronuclei are a diameter of less than 1/3 of the main nuclei, no connection or overlap to the main nuclei and similar staining intensity [102, 105].

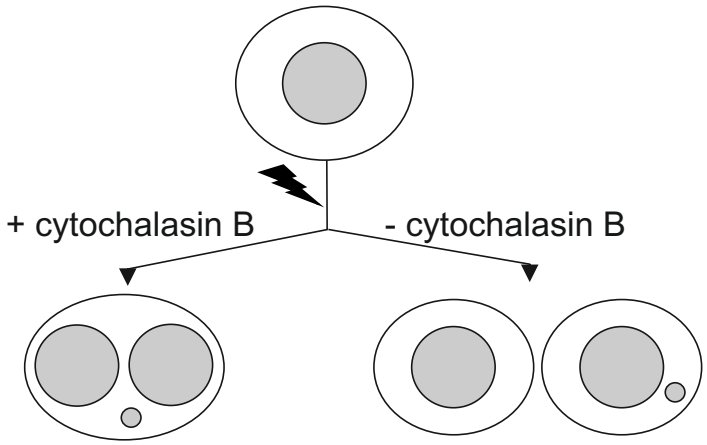

Figure 5.7: *Micronuclei induction: After irradiation (or treatment with carcinogens) micronuclei (MN) can form when whole chromosomes or acentric fragments are not included in the daughter nuclei. Treatment with cytochalasin-B inhibits division of the cytoplasm after nuclear division, resulting in binucleated cells with MN in the common cytoplasm. Without cytochalasin-B, MN can be found in the cytoplasm of the daughter nuclei (cf. [105]).*

The protocol for MN analysis used in this work is based on the procedure developed by Curren for the epidermal model Epiderm^{TM} [106]. Directly after irradiation, 3 mg cyt-B per ml culture medium was added to the samples. About 48 hours later, keratinocytes were isolated from the tissue samples following the methods of Curren and Mun [79, 106, 107]: Tissue samples (within the tissue culture inserts) were placed in 5 ml EDTA (0.1 %) for 15 minutes. Then the tissues were separated manually from the microporous membrane and the dermis was removed from the epidermis, as dermal fibroblasts were excluded from analysis due to their low abundance. The epidermal tissues were transferred in new 12-wells containing 1 ml trypsin/EDTA solution and incubated at 37 °C for 20 minutes. Trypsinized cells were collected from the solution and single cell solutions were prepared and transferred to conical tubes (15 ml) with 8.5 ml RPMI culture medium, supplemented with 10 % FBS (fetal bovine serum) to neutralize the trypsin. After centrifugation and removal of the supernatant, samples were treated hypotonically using 75 mM KCL for 3 min. Then the cells were fixed in methanol/acetic acid (3:1) and the cell suspensions were stored at 2-8 °C for minimum 72 hours. After centrifugation, a drop of each cell solution was pipetted onto clean, dry microscope slides and, after drying, stained with acridine orange (20 µg/ml). Slides were scored under a fluorescence microscope, counting at least 500 binucleated keratinocytes with well-preserved cytoplasm and detached micronuclei (0-4 MN). MN were always counted by Thomas Schmid to avoid inter-person variability.

5.4 Results of the in-vitro skin study

5.4.1 Tissue viability

Cellular viability of the cut out skin tissue was quantified 40 h (Exp.1+2) and 10 days (Exp.3) after irradiation using the colorimetric MTT assay. The later time point for the third experiment was given by the termination of the ELISA experiment, when the skin samples were not required to stay in culture any longer and could therefore additionally be used for the evaluation of tissue viability at this time. The punched area had a diameter of 3 mm in Exp.1, but was increased to 5 mm in experiments 2 and 3, due to the larger inter-beam distances. However, this is unlikely to cause significant changes in the evaluated area, as the absolute difference between the areas is not very large and still less than half of the total skin was utilized.

Viability compared to untreated controls CO was determined for all irradiation modes in triplicates in each (sub-)experiment. Pooled mean values and standard errors are given in Table 5.1. Experiment 1 compared the very small minibeams of 10x10 and 50x50 μm^2 size to homogeneously irradiated skin samples, showing a significantly enhanced tissue viability of (74±5) % and (92±7) % for the two minibeam modes in comparison to only (49±7) % for homogeneous irradiation ($P < 0.05$) [23]. The same result was obtained using larger beams of 100x100 and 180x180 μm^2 size, where tissue viability was (83±3) % in both cases[(3)] compared to (40±3) % after homogeneous irradiation, showing no significant difference to the smaller minibeams using the unpaired t-test ($P > 0.05$). Figure 5.8 summarizes the results of experiments 1 and 2, using the pooled values of both experiments for CO, HF and 50x50 μm^2 (six samples each), as these irradiation modes were utilized in both experiments and yielded similar values which were not significantly different from each other ($P > 0.05$).

Proton irradiations using larger, Gaussian-shaped minibeams (WB and OB, cf. 5.2) were also compared to homogeneous irradiation and to square minibeams of 180 µm edge length (Exp.3.2+3.3, Table 5.1). As the MTT assay was only performed 10 days after irradiation, values are not directly comparable to previous results, as the tissues were found to have a lower viability than shortly after irradiation (reduction by approx. 25 % in untreated controls). This might also explain the differences between the two independent experiments for some of the irradiation modes. Nevertheless, cell viability in minibeam irradiated tissues was still higher for all three minibeam modes

[(3)] The results of the 180x180 mode are published in Girst et al. 2015*a* [24] under the abbreviation "LC".

Irradiation mode	Exp.1	Exp.2	Exp.1+2 pooled	Exp.3.2	Exp.3.3	Exp.3.2+3.3 pooled
CO	100±5	100±1	**100±4**	100±2	100±2	**100±4**
HF	49±7	40±3	**44±6**	33±1	32±2	**33±3**
10x10	74±5		**74±5**			
50x50	92±7	79±1	**86±7**			
100x100		83±2	**83±2**			
180x180		83±2	**83±2**	73±2	98±2	**85±10**
WB				74±2	76±2	**75±6**
OB				64±3	82±2	**74±7**

Table 5.1: *MTT test results for Experiment 1, 2 and 3 including pooled values. Cell viability (%) relative to untreated negative control (CO) with standard error of the mean (SEM). HF homogeneous field, WB widened beams ($\sigma \approx 260\,\mu m$), OB overlapping beams ($\sigma \approx 520\,\mu m$)*

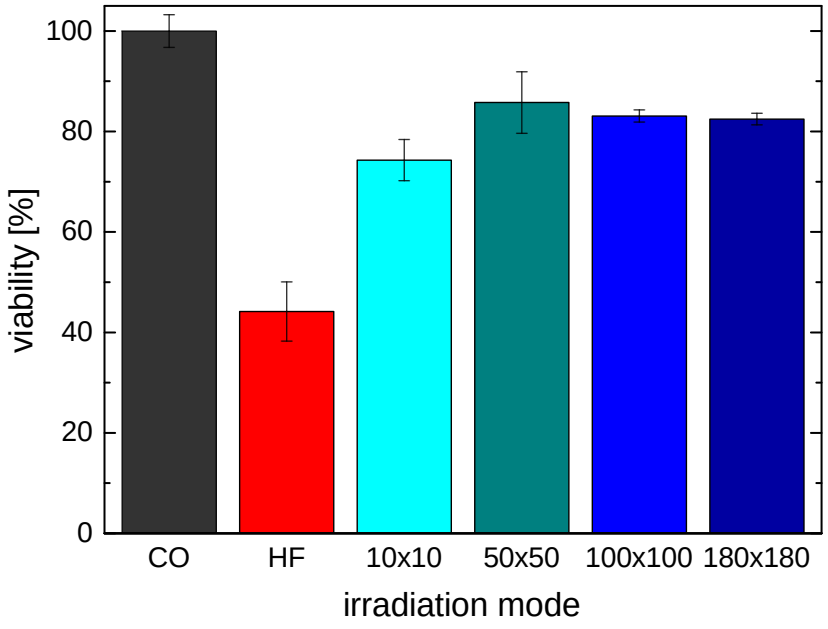

Figure 5.8: *Tissue viability measured by the MTT test 40 h after irradiation: Viability relative to untreated controls (CO) for experiments 1 and 2 (pooled values for 50x50 μm^2 and homogeneous irradiation HF). Error bars represent standard error of the mean.*

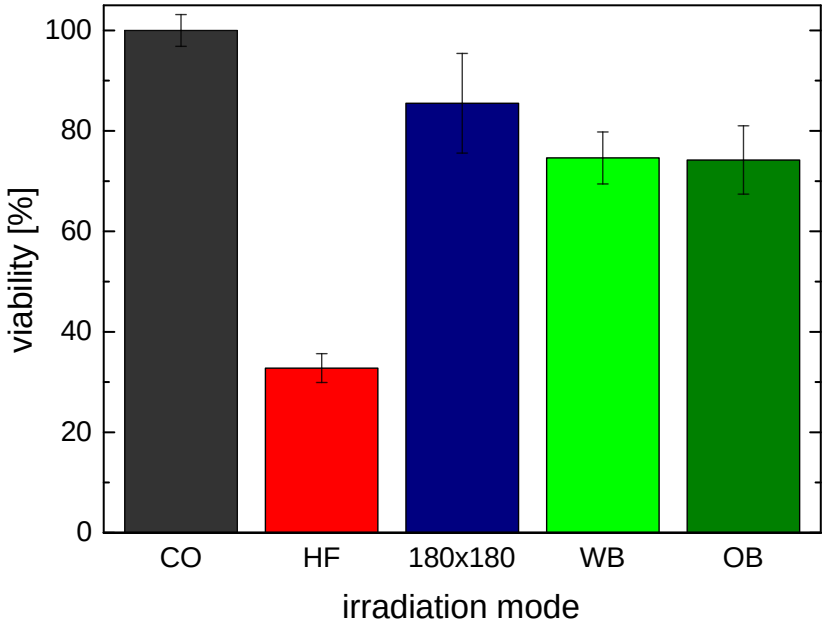

Figure 5.9: *Skin tissue viability measured by the MTT assay 10 days after irradiation: Percentage viability relative to untreated controls (CO) for experiment 3 (pooled values of Exp.3.2+3.3). Error bars represent standard error of the mean.*

than in homogeneously irradiated samples ($P < 0.05$). While the smallest minibeams yielded similar results as in Exp.2 with (85±10) %, widened minibeams with a size of $\sigma \approx 260\,\mu m$ resulted in (75±6) % and overlapping beams of 520 µm in (74±7) % relative to CO (see Fig. 5.9). These values are not significantly lower than in the square minibeam mode. [25]

Skin tissue irradiated with square minibeams of 10 to 180 µm edge length and Gaussian beams of up to 1.2 mm FWHM resulted in only a small decrease in cell viability compared to untreated controls, without any significant variation between the different sizes and irradiated fractions of the applied minibeam modes, while homogeneous irradiation reduced tissue viability by more than half.

5.4.2 Expression of pro-inflammatory cytokines

The inflammatory cytokines TGF-β, IL-6 and Pro-MMP1 were quantified in the culture medium of irradiated and sham-treated EpiDermFT^{TM} skin tissues every other day for 14 days following irradiation with 10x10 and 50x50 μm^2 minibeams and homogeneous field (Exp.1). Protein levels were significantly increased after all irradiations compared to unirradiated controls (CO), as displayed in Fig. 5.10. However, homogeneous irradiation lead to higher levels of TGF-β and IL-6 throughout the 14 observation days in comparison to both minibeam irradiations. Furthermore, Pro-MMP1 expression in the supernatant of the skin samples decreased significantly faster from 6 days after irradiation by minibeams than after homogeneous irradiation. No significant qualitative or quantitative difference could be detected in the cytokine response of the two minibeam irradiations. [23]

Unfortunately, no meaningful results could be obtained for larger minibeams in experiments 2 and 3.

The expression of pro-inflammatory cytokines is often an indicator for acute adverse effects initiated by irradiation [108, 109]. TGF-β is activated by ionizing radiation and is therefore a predictive marker for radiation-induced inflammation [97, 110]. Another pro-inflammatory biomarker is interleukin 6 which is produced by epidermal keratinocytes following irradiation of the skin [98, 111]. Pro-MMP1 belongs to the family of matrix metalloproteinases which play an important role in wound healing [111]. Therefore, a decreased expression of these cytokines in the skin as measured for the minibeam irradiations indicates a reduced inflammatory response and potentially less acute side effects in comparison to conventional broad beam radiotherapy. [23]

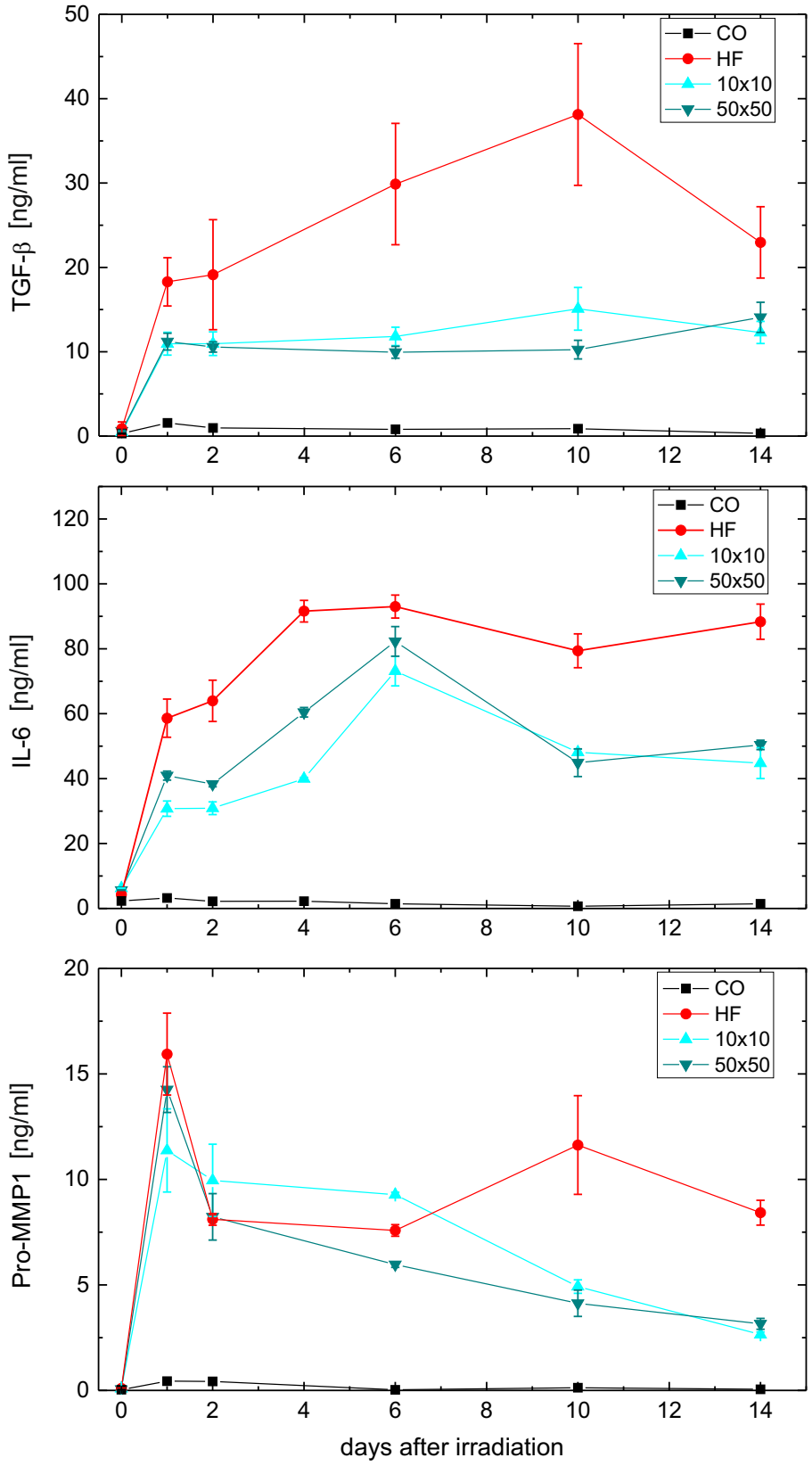

Figure 5.10: *Levels of inflammatory cytokines TGF-β, IL-6, and Pro-MMP1 in culture media after 10x10 μm^2 and 50x50 μm^2 minibeam and homogeneous irradiation (HF), measured over 14 days (SE of the mean are indicated by vertical error bars). CO sham-treated controls.*

5.4.3 Genetic damage

Micronucleus induction, a measure for genetic damage after exposure to ionizing radiation, was analyzed in the epidermal kerationcytes of the cut out skin tissues 48 hours after irradiation using the cytokinesis-block method. Tables B.1-B.6 in the supplement present the detailed results of the MN induction in binucleate keratinocytes of experiments 1-3 (each divided into two sub-experiments in two independent beam-times), while Tables 5.2 and 5.3 summarize the pooled results, grouped according to irradiation mode. Pooled values could be determined for each irradiation mode from at least 6 samples from two beam-times, as the results from the sub-experiments showed no major differences.

Irrad. mode	**Analyzed cells**	**MN per CB cell (± SE)**	**Intercellular MN distribution**				**DMF (± SE)**
			0	**1**	**2**	**3**	
HF	8974	**0.070±0.004**	8549	262	123	40	**1.21±0.15**
10x10	3000	**0.022±0.004**	2598	25	9	8	**0.23±0.11**
50x50	3000	**0.030±0.005**	2939	38	16	7	**0.40±0.12**
100x100	3000	**0.030±0.005**	2947	27	16	10	**0.39±0.12**
180x180	3000	**0.015±0.003**	2819	20	7	4	**0.09±0.09**
180x180*	2908	**0.025±0.004**	2856	35	12	5	**0.29±0.11**
WB	2771	**0.042±0.005**	2688	58	17	8	**0.64±0.14**
OB	2933	**0.056±0.006**	2830	64	28	15	**0.93±0.17**

Table 5.2: *Micronucleus (MN) frequency and distribution in cytokinesis-blocked (CB) binucleated keratinocytes induced by 2 Gy of 20 MeV protons in 7 irradiation modes: homogeneous irradiation (HF) versus minibeam irradiations of different square sizes (10-180 μm edge length) and Gaussian shape ($\sigma \approx 260\,\mu m$ (WB) and $\sigma \approx 520\,\mu m$ (OB)). Dose modification factors (DMF) were calculated like RBE from comparison with X-ray dose response curve (Fig. 5.12). 180x180* is minibeam irradiation through the 200 μm Aluminum sheet. Pooled values were determined for the three samples from each sub-experiment and then pooled with the results from the other sub-experiment (bold).*

Exp. number	Irrad. mode	Analyzed cells	MN per CB cell (± SE)	Intercellular MN distribution			
				0	1	2	3
Exp. 1.1	HF	1500	0.067±0.009	1427	51	16	6
Exp. 1.2	HF	1500	0.073±0.009	1421	55	17	7
Exp. 2.1	HF	1500	0.075±0.009	1428	39	26	7
Exp. 2.2	HF	1500	0.064±0.009	1435	41	17	7
Exp. 3.1	HF	1453	0.072±0.009	1385	38	23	7
Exp. 3.2	HF	1521	0.068±0.009	1453	38	24	6
Σ 1+2+3	**HF**	8974	**0.070±0.004**	8549	262	123	40
Exp. 1.1	10x10	1500	0.024±0.006	1477	14	5	4
Exp. 1.2	10x10	1500	0.021±0.005	1481	11	4	4
Σ 1.1+1.2	**10x10**	3000	**0.022±0.004**	2598	25	9	8
Exp. 1.1	10x10	1500	0.030±0.006	1469	20	8	3
Exp. 1.2	50x50	1500	0.031±0.006	1470	18	8	4
Σ 1.1+1.2	**50x50**	3000	**0.030±0.005**	2939	38	16	7
Exp. 2.1	100x100	1500	0.028±0.006	1475	13	7	5
Exp. 2.2	100x100	1500	0.031±0.006	1472	14	9	5
Σ 2.1+2.2	**100x100**	3000	**0.030±0.005**	2947	27	16	10
Exp. 2.1	180x180	1500	0.016±0.004	1484	10	4	2
Exp. 2.2	180x180	1500	0.015±0.004	1335	10	3	2
Σ 2.1+2.2	**180x180**	3000	**0.015±0.003**	2819	20	7	4
Exp. 3.1	180x180*	1436	0.029±0.006	1409	16	8	3
Exp. 3.2	180x180*	1472	0.021±0.005	1447	19	4	2
Σ 3.1+3.2	**180x180***	2908	**0.025±0.004**	2856	35	12	5
Exp. 3.1	WB	1462	0.047±0.008	1417	28	11	6
Exp. 3.2	WB	1309	0.037±0.007	1271	30	6	2
Σ 3.1+3.2	**WB**	2771	**0.042±0.005**	2688	58	17	8
Exp. 3.1	OB	1398	0.057±0.008	1354	27	11	10
Exp. 3.2	OB	1535	0.056±0.008	1476	37	17	5
Σ 3.1+3.2	**OB**	2933	**0.056±0.006**	2830	64	28	15

Table 5.3: *Micronucleus (MN) frequency and distribution in cytokinesis-blocked (CB) binucleated keratinocytes induced by 2 Gy of 20 MeV protons in 7 irradiation modes: homogeneous irradiation (HF) versus minibeam irradiations of different square sizes (10-180 μm edge length) and Gaussian shape ($\sigma \approx 260\,\mu m$ (WB) and $\sigma \approx 520\,\mu m$ (OB)). 180x180* is minibeam irradiation through the 200 μm Aluminum sheet. Pooled values were determined for the three samples from each sub-experiment and then pooled with the results from the other sub-experiment (bold).*

Figure 5.11 visualizes the pooled results for all irradiation modes, revealing a significant difference between homogeneous irradiation and all minibeam irradiations except for the largest beams of 1.2 mm FWHM (OB). All these minibeam modes (without OB) were not significantly different from each other, except for the 180x180 μm^2 beams[(4)] with the largest inter-beam distance of 1.8 mm. Nevertheless, when these minibeams were applied to the skin through the 200 µm Aluminum sheet required for generation of the Gaussian minibeams in Exp.3 (therefore termed 180x180*), an increase in the micronuclei yield was measured, resulting in values in the range of all other minibeam modes (except for OB). This probably arises from the increased valley doses between the minibeams caused by proton scattering in the Aluminum, leading to an (irradiated fraction of approx. 11 % instead of 7 %, (cf. section 5.2). [23, 25]

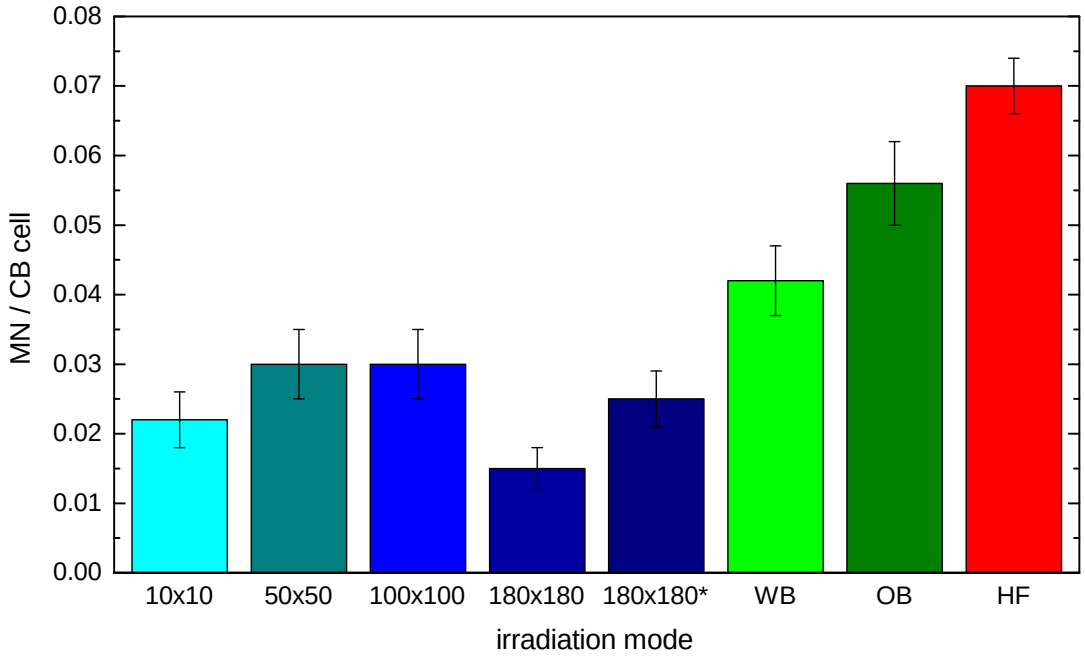

Figure 5.11: *Micronucleus (MN) frequency in binucleated (CB) epidermal keratinocytes 48 h after irradiation. Pooled data from at least 6 samples in two independent beam-times with standard error. Minibeam irradiation sorted according to beam size (from 10x10 μm^2 to $\sigma \approx 520\,\mu m$ (OB)) and homogeneous irradiation (HF). Irradiation with 180x180 μm^2 minibeams with (180x180*) and without (180x180) Aluminum sheet.*

[(4)] The results of the 180x180 mode are published in Girst et al. 2015*a* [24] under the abbreviation "LC".

The micronucleus frequencies determined for the square minibeams of 0.015-0.030 MN/CB cell (without Al) are higher than expected from the 7 % of the area receiving doses larger than 1 % of the mean dose (i.e. ≥ 0.02 Gy), which would allow only 7 % of the HF yield, i.e. values of 0.07×0.070 MN/CB cell = 0.005 MN/CB cell, assuming a non-linear dose-effect curve for the high doses in the minibeams, where most cells do not undergo division anymore and thus cannot form micronuclei. This increase could be due to the bystander effect found in intercellular communication, which has already been demonstrated in this skin model [60–62] and in other experiments analyzing out-of-field effects [112, 113]. [23]

For quantification of the genetic damage in comparison to a homogeneous X-ray irradiation, a reference curve was obtained from irradiation with 200 kV X-rays at different doses (Table 5.4, Fig. 5.12, [23]). A linear dose-response curve was determined for the MN induction in keratinocytes of the in-vitro skin model, as has been described for peripheral blood lymphocytes in-vivo [104]. The coefficients obtained from a weighted least-squares approximation to the measured X-ray data for the linear increase of MN per CB cell (y) with dose D,

$$y(D) = c + a \cdot D \tag{5.1}$$

were $a = (0.0247 \pm 0.0020)$ Gy^{-1}, $c = 0.0107 \pm 0.0021$, and the correlation coefficient between a and c cor (a, c) = -0.535. [23]

Dose [Gy]	**Analyzed cells**	**MN per CB cell (± SE)**	**Intercellular MN distribution**			
		y	**0**	**1**	**2**	**3**
0	1000	0.011±0.004	991	7	2	0
0.5	1000	0.020±0.006	985	11	3	1
1	1000	0.036±0.007	971	24	3	2
2	1000	0.069±0.011	952	32	11	5
4	1000	0.103±0.013	925	55	12	8

Table 5.4: *Micronucleus (MN) frequency and distribution in cytokinesis-blocked (CB) binucleated keratinocytes induced by different doses of 200 kV X-rays [23]*

The dose modification factor (DMF) is defined equivalent to the relative biological effectiveness (RBE), as the ratio of the dose of a reference radiation (D_{ref}, here: 200 kV X-rays) and the tested radiation (D_{test}, here: 20 MeV protons in different irradiation modes) for induction of the same effect. D_{ref} is determined by inversion of the linear

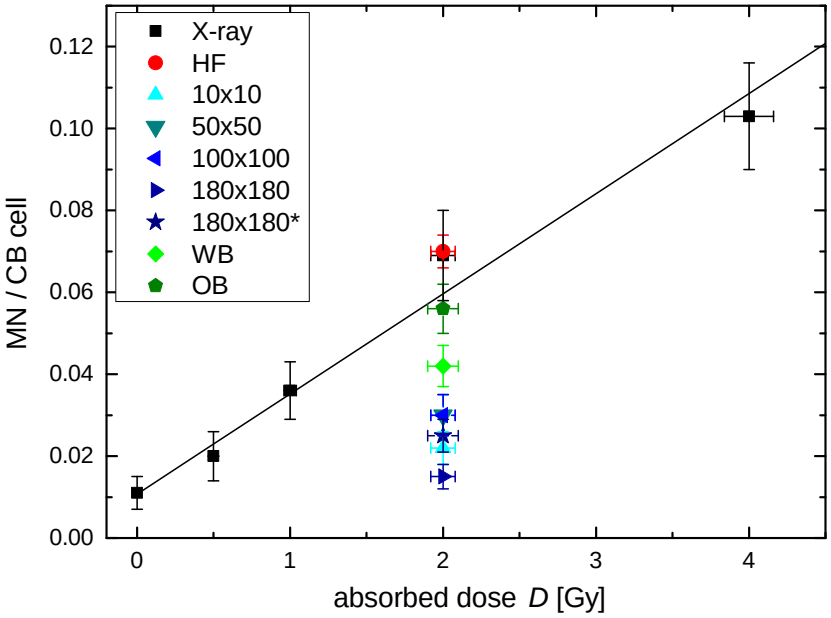

Figure 5.12: *Linear dose-response curve for micronuclei (MN) induction in cytokinesis-blocked (CB) binucleated keratinocytes by 200 kV X-rays (black squares). Additionally, the mean MN frequencies from proton irradiation in a homogeneous (HF) and 7 minibeam modes are shown. Irradiation with 180x180 μm^2 minibeams were performed with (180x180*) and without (180x180) Aluminum sheet. Vertical and horizontal error bars represent the standard error of the mean. [23]*

dose effect curve $y(D)$. The standard errors of the DMF do not only account for the parameter errors, but also for the correlation between the parameters.

For the homogeneous irradiation, the resulting $DMF_{HF} = 1.21 \pm 0.15$, meaning no significantly different MN induction compared to X-ray irradiation. For the square minibeams, the determined dose modification factors were $DMF_{10x10} = 0.23 \pm 0.11$, $DMF_{50x50} = 0.40 \pm 0.12$, $DMF_{100x100} = 0.39 \pm 0.12$, $DMF_{180x180} = 0.09 \pm 0.09$ and $DMF_{180x180*} = 0.29 \pm 0.11$. The larger Gaussian minibeams resulted in DMF of $DMF_{WB} = 0.64 \pm 0.14$ and $DMF_{OB} = 0.93 \pm 0.17$. [23, 25]

The genetic damage and thus risk of secondary tumors induced by minibeam irradiations was analyzed in a human skin model but can also be applied to other normal tissue cells underneath the skin (e.g. muscles), as the radiation response on a cellular base is not expected to differ much between cell types when the same average dose is used - the absolute numbers of micronuclei might be different but the trend is similar. Even though the widening of the minibeams with increasing depth in tissue results

in increasing micronuclei frequencies (demonstrated in Exp.3), there is still a significant reduction for non-overlapping channels (as WB) compared to homogeneous broad beams and also the almost homogeneously overlapping channels (OB) never exceeded the genetic damage induced by a homogeneous dose distribution. Therefore, minibeam irradiation is not expected to yield higher genetic damage anywhere in the entrance channel compared to broad beams. [25]

5.5 Conclusion

The human in-vitro skin model EpidermFT^{TM} was used to compare minibeam irradiation of different beam sizes and shapes to conventional homogeneous proton irradiation of the same average dose (2 Gy) with respect to acute side effects and potential genetic damage. Tissue viability after irradiation was measured by the MTT test and was significantly higher in tissues irradiated with minibeams of either size in comparison to homogeneously irradiated tissues, where viability was reduced to less than half compared to unirradiated controls. Acute inflammation, quantified via the release of pro-inflammatory cytokines (IL-6, TGF-β, Pro-MMP1) into the culture medium, was lower after minibeam irradiation than after homogeneous irradiation, pointing towards reduced acute adverse effects after radiation therapy. Genetic damage in normal tissue, which is closely related to the risk of developing mutations and might eventually lead to secondary tumor induction, was analyzed with the micronucleus test in the epidermal keratinocytes of the skin model. Minibeam irradiations with beams up to 180x180 μm^2 size induced less than half of the micronuclei produced by homogeneous irradiation (0.015-0.030 vs. 0.070 MN/CB cell). Increasing the size of the minibeams and therefore the fraction of irradiated skin (receiving a dose higher than the mean dose of 2 Gy) led to an increasing number of MN per divided cell, but never exceeded the genetic damage induced by a homogeneous dose distribution.

These results suggest a reduction of acute radiation effects in the skin and subjacent tissues and a decreased risk of genetic damage induced by the irradiation of healthy tissue in front of the tumor when using proton minibeams instead of conventional homogeneous broad beams. Nevertheless, a validation of these in-vitro results in an in-vivo model with functioning immune system and higher complexity including blood vessels and further cell types is irreplaceable before the concept can be introduced in radiation therapy and will be subject of the next chapter.

Chapter 6

Study in an in-vivo mouse ear model

After the first experimental applications of minibeam radiotherapy in an in-vitro human skin model, indicating reduced side effects compared to homogeneous broad beam irradiations, further experiments are required in an in-vivo model to investigate the effects of minibeams in a more authentic and complex skin model with vasculature and all naturally occurring cell types. Furthermore, a working immune system is of great importance for the acute inflammatory response to ionizing radiation [114]. Therefore, the ear of healthy adult BALB/c mice was chosen as a representative of murine skin, with two skin layers covering the cartilage of the ear on both sides. The applied minibeams had a size of 180x180 μm^2 and the inter-beam distances were 1.8 mm, just like in Experiment 3 of the skin study and in the model treatment plan for a 2.5 cm tumor in a depth of 7-9.5 cm in section 3.4.2. For the determination of a suitable dose to compare homogeneous and minibeam irradiation, a pilot study with different homogeneous doses of X-rays was conducted. Most of this mouse study has already been published in Girst et al. 2015*c* [17].

6.1 Animal model and ethics statement

The animal study was performed using 10- to 12-week-old female BALB/c mice (Charles River Laboratories, Germany; Fig. 6.1) according to German federal law and with approval of the German regional animal ethics committee. The mice were housed and cared for in a temperature-regulated animal facility at the Klinikum rechts der Isar (Munich), exposed to a 12-hr light/dark cycle, with ad libitum access to food and water. [17]

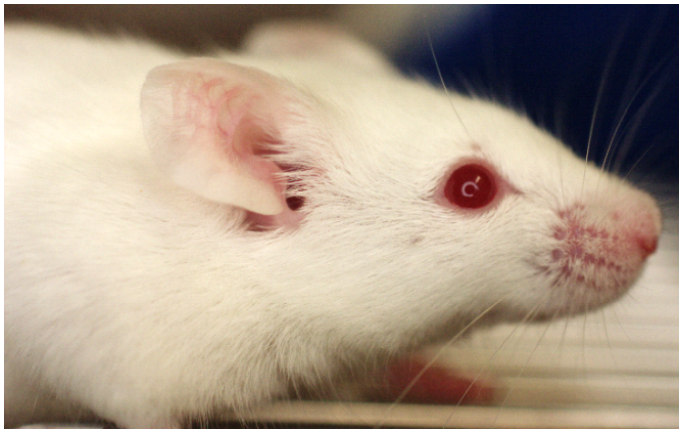

Figure 6.1: *Mouse model: Adult female BALB/c mouse.*

Mouse ears were chosen as a model for murine skin due to the small ear thickness of only about 250 µm, which allows the detection of 20 MeV protons (range in water $\approx$4.6 mm) directly behind the ears, without the need to pull away the skin from the body as necessary e.g. for the irradiation of the skin on the back. As the protons do not stop in the ear, no undesired ancillary effects are expected, as well as allowing a precise and basically constant dose application across the ear profile. Ears have two layers of skin tissue separated by a layer of cartilage, allowing to monitor skin reactions on both sides simultaneously. The existence of this cartilage layer and the lack of a fat layer underneath the dermis are unique to the skin of the ear [115]. Nevertheless, single fat cells can be found in the ear as well (see Fig. 6.2). However, these properties are not expected to lead to an altered radiation response compared to skin of other body parts. [17]

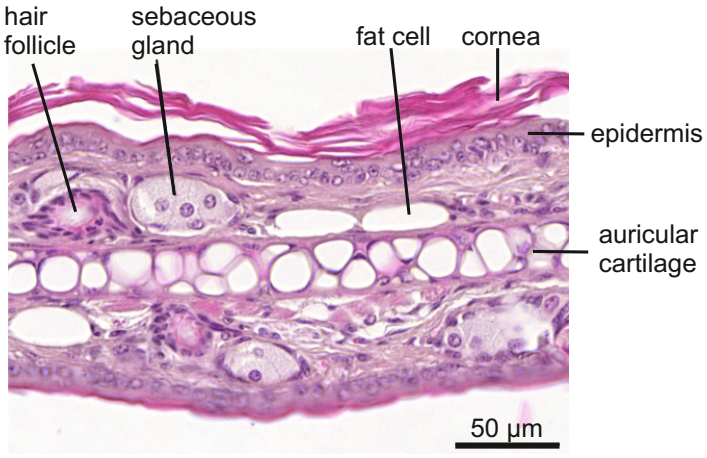

Figure 6.2: *Histological section through the ear of a BALB/c mouse. [17]*

The major difference between human and murine skin is the greater thickness of the epidermis and especially the stratum corneum in humans [90]. Radiation-induced skin reactions are similar in both species, but require approximately twice the dose for mice, due to a more cellular dermal papilla and typically smaller irradiation fields [114].

The white BALB/c mice were selected because of their relatively large ears of approximately 1 cm diameter and the presence of only few and very thin and light-colored hair, facilitating the monitoring of ear reactions. BALB/c has been found to have a higher radio-sensitivity than other inbred mouse strains due to a deficiency in DNA repair, with lethal (whole-body) doses of $LD_{50(30d)} \sim 5$ Gy compared to e.g. ~ 6 Gy for C57BL mice [116, 117].

For the pilot study with photons, 7 dose groups (2, 5, 10, 20, 40 and 60 Gy) with 6 mice each were used, with one group being sham-irradiated controls (0 Gy). For the proton study comparing minibeam (MB) and homogeneous irradiation (HF), 34 animals were irradiated for monitoring over approximately 90 days[(1)] to elucidate the acute radiation response, 12 MB, 12 HF and 10 sham-irradiated controls (CO). Another 18 mice were used for histological analysis at 15, 25 and 36 days after irradiation (3 MB and 3 HF at each time point). [17]

During all irradiations, mice were under general anesthesia, which was induced by intraperitoneally injected MMF (medetomidine (0.5 mg/kg), midazolam (0.5 mg/kg) and fentanyl (0.05 mg/kg)). The antagonist AFN (atipamezole (2.5 mg/kg), flumazenil (0.5 mg/kg) and naloxone (1.2 mg/kg)) were administered subcutaneously max. 45 minutes after induction of the anesthesia. [17]

6.2 Biological endpoints

The acute response following the irradiation with X-rays or protons was monitored for the first three months after radiation exposure. Visible or measurable changes of the irradiated ear such as swelling, reddening or desquamation were scored and correlated with the histological findings at 3 time points after irradiation.

[(1)] The cut-off time between early and late effects has arbitrarily been set to 90 days after the start of radiotherapy [41]

6.2.1 Ear thickness measurements

For the measurement of the thickness of treated (right) ear and the untreated (left) ear a specially adapted electronic external measuring gauge (C1X079, Kröplin GmbH, Schlüchtern, Germany) was obtained, with measuring contacts of 6 mm diameter (Fig. 6.3). During measurement, one person held the mouse while a second person performed the measurements of both ears in triplicate. Measurements were performed by Judith Reindl most of the time to avoid inter-person variability.

Figure 6.3: *Measuring gauge for ear thickness determination (C1X079, Kröplin GmbH).*

6.2.2 Skin reaction scoring

Radiation-related skin reactions are usually not evident immediately after exposure, as damage is induced in the cells of the deeper basal layer, so that there is a time-lag before the superficial skin layers are affected [118]. The latent time of early effects is mostly independent of the applied dose, while severity and duration are dependent on dose and the size of the irradiated area [41]. Visible reactions resulting from irradiation were categorized as erythema, desquamation, changes of ear morphology and hair loss. Erythema is the reddening of the skin after injuries, inflammation or infections, due to increased blood flow in dilated or congested superficial capillaries [119]. Desquamation is the peeling of the cornified layers of the epidermis in scales [119]. Dry desquamation is an "atypical keratinization of the skin due to the reduction in the number of clonogenic cells within the basal layer of the epidermis" [90], while moist desquamation, with leakage of serum or other moist exudate [118], is the "loss of the epidermis

due to the sterilization of a high proportion of the clonogenic cells within the basal layer", "associated with the loss of the reproductive integrity of stem cells" [90]. Moist desquamation is more likely to appear in skin that is under friction or has folds. In humans, this is typically found at 2-3 weeks after the begin of radiotherapy due to the turnover time of the human epidermis of 20-56 days, compared to 8-10 days for mice [41, 120]. A crust is a layer of dried exudate (typically pus or blood) and peeled off cells from an open wound, occurring in the context of moist desquamation when the damaged tissue starts to heal [118, 119].

Changes in the morphology of the ear, such as waviness, bends and stiffness, depended critically on the exact location of the irradiation field on the ear, which however was not possible to standardize for the differently sized and shaped ears of the irradiated mice. Therefore, this endpoint was not included in the skin score for the acute reaction, but only recorded for completeness. Hair loss, which often occurs as an unpleasant side effect of radiotherapy, was monitored as further skin reaction, but, as a non-inflammatory response occurring only after the decline of erythema and desquamation, was not added to the skin score. Therefore, the score consisted only of the two parts erythema (Score A) and desquamation (Score B), rated in four grades each (see Table 6.1, modified from [121]), which were added up to a total skin score [17]. The non-linear scale for the erythema score arises from the additional grade "mild erythema" between the first two grades (no and definite erythema) of the otherwise linear scale (with equal maximum as desquamation), to allow further discrimination of the skin responses.

Score A	**Erythema**	**Score B**	**Desquamation**
0	no	0	no
0.5	mild erythema	1	dry desquamation
1.5	definite erythema	2	crust formation
3	severe erythema	3	moist desquamation

Table 6.1: *Skin score for erythema (A) and desquamation (B). The total skin score is obtained by adding up Score A and B.*

6.2.3 Histology

For a better understanding of the underlying cellular processes leading to ear swelling and other visible skin responses, histological sections were prepared for three time-points after irradiation in the proton study. At the time point of interest, animals were sacrificed and ears were dissected, placed in plastic cassettes and stored in formalin at 4 °C overnight. On the following day, ears were placed in a tissue processor at the department of Pathology (Klinikum rechts der Isar, Munich, Germany) where they ran through increasing concentrations of alcohol for dehydration of the tissues and infiltration of paraffin into the tissues. The paraffin-embedded samples were cut in 3 µm sections and stained with hematoxylin and eosin (H&E stain) for examination. [17]

6.2.4 Micronuclei induction in blood lymphocytes as biomarker for irradiation

For the determination of chromosome damage induced by homogeneous and minibeam irradiation, the micronucleus test with cytokinesis-block (cf. section 5.3.3) was performed in the blood lymphocytes of the irradiated mice at the end of the monitoring phase of 90 days. The MN protocol was adopted from Fenech and Morley [122]: blood samples, obtained from heart puncture, were heparinized (0.3 ml) and added to RPMI culture medium (4.7 ml; Sigma, Germany), supplemented with foetal calf serum (10 %; Sigma, Germany), phytohemaaglutinin (1.5 %, Invitrogen, Germany), penicillin (100 IU) and streptomycin (100 µg/ml). Cells were blocked from cytoplasmatic division with cytochalasin B (3 µg/ml; Sigma, Germany) at 21 h after sample preparation and harvested 27 h later following the standard MN protocol. Lymphocytes from the mouse blood were harvested and fixed in methanol/acetic acid (3:1) overnight. Staining was done with 100 mg/ml acridine orange in a phosphate buffered solution (pH 7). Scoring of micronuclei in at least 500 cells with binucleate appearance (CB cells) was performed according to the criteria of Fenech and Morley [102] by Thomas Schmid.

6.3 X-ray pilot study

The aim of the pilot study was the determination of a dose-effect curve for skin reactions of the ear in the first three months after irradiation, in order to chose an appropriate dose for the proton study comparing homogeneous and minibeam irradiation and for comparison of the proton and X-ray irradiations in the same skin model. Ear swelling and visible skin reactions like reddening and desquamation were taken as endpoints for this preliminary experiment.

6.3.1 Experimental setup

All irradiations were performed at the RS225 (Xstrahl Ltd) of the Klinikum rechts der Isar (Munich), using 70 kV X-rays. The setup is shown in Fig. 6.4. The definition of the irradiation field was via a 4 mm thick tungsten collimator with an aperture of $7.2 \times 7.2\,mm^2$ size, which was positioned over the center of the mouse ear. For irradiation, the mice were placed in a specially designed holder (Fig. 6.4, design drawings in Appendix C), where they were lying on their side and the right ear was fixed to the elevated plateau of the holder (Fig. 6.4b). In the area where the ear is positioned, a perspex insert is embedded in the Aluminum holder to ensure similar absorption and reflection characteristics as the ear tissue for a correct dose application. [17]

The mice were shielded from radiation by a custom-made "lid" of 3 mm tungsten, sparing only the right ear of the mouse on the plateau (Fig. 6.4c). The tungsten collimator was fixed on the ear table with the square aperture above the central part of the ear, protecting the rest of the ear from unintended irradiation.

During irradiation, the X-ray machine was heated to 32 °C to avoid undercooling of the anesthetized mice in the preheated Al holder. Air slits in the lying area of the holder ensured oxygen supply during the up to 13 minutes of irradiation. The exposure values of the machine were set to 70 kV, 10 mA and a table height of 250 mm (approx. source-target distance), to enable the required high dose rates which allowed irradiation of up to 60 Gy in less than 15 minutes. Positioning of the holder in the machine was performed with the help of a laser cross line to an accuracy of a few millimeter. Irradiation times were entered according to the desired X-ray dose based on a dose rate of 0.08 Gy/s, which was determined at the ear position using Gafchromic films and ionization chamber by Prof. Dr. Jan Wilkens. The chosen dose range was based on previous experiments of Law et al. [121], which however irradiated the complete ear. Therefore, the doses selected for the pilot study were 0, 2, 5, 10, 20, 40 and 60 Gy.

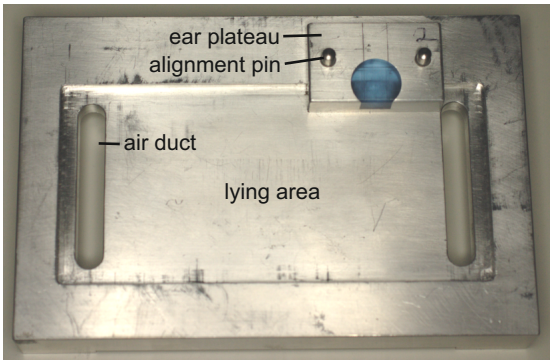

(a) *Aluminum base plate of the holder. Ear plateau with (blue) perspex insert and two alignment pins for positioning of the tungsten collimator. Cut-out lying area with air ducts.*

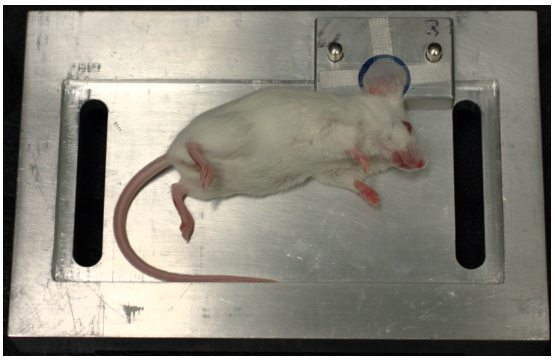

(b) *The mouse is lying on its side in the lying area with the ear on the plateau.*

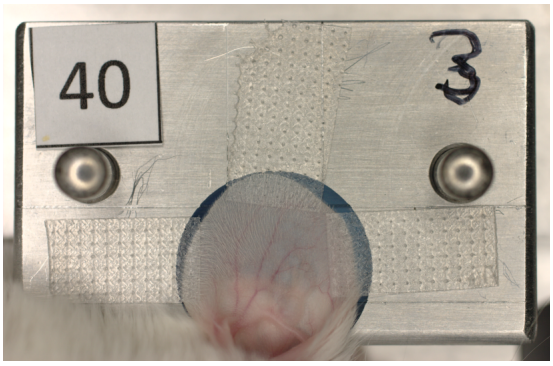

(c) *The ear is centered on the perspex insert of the designated plateau and fixated using skin tape. Mouse number (40) and holder number (3) are added for identification purposes.*

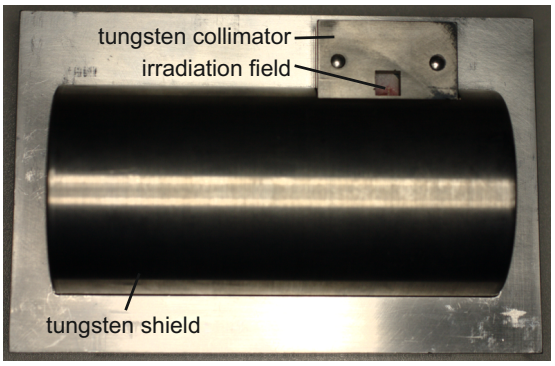

(d) *The tungsten collimator with the square aperture of 7.2 x.7.2 mm^2 is mounted to the ear plateau and the half-cylindrical tungsten shield is positioned in the cut-out of the base plate, protecting the mouse from irradiation.*

Figure 6.4: *Custom-made mouse holder for X-ray irradiations at the Klinikum rechts der Isar. The mouse is lying on its side with only the central 7.2 x 7.2 mm^2 exposed to radiation and the rest of the body protected by a tungsten shield.*

6.3.2 Results of the X-ray pilot study

The aim of the pilot study with broad beam X-ray irradiations of the central 7.2 x 7.2 mm^2 of the mouse ear was the generation of a dose-effect curve for the used skin model as a reference for the main study comparing proton broad beam and minibeam irradiation. Acute inflammatory response, i.e. skin reactions and swelling of the ear were examined for the first 90 days following irradiation. [17]

The mean ear thickness of each dose group is plotted in Fig. 6.5 for the whole monitoring time. The ear thickness data of each individual mouse of a dose group can be found in Appendix D. No increase in ear thickness could be detected for mice irradiated with doses ≤ 5 Gy at any time after irradiation. For ears irradiated with 10 Gy and 20 Gy X-rays, a small increase of less than 100 µm was measured, with the maximum swelling at about 20 days after irradiation. After 40 and 60 Gy, ear thickness increased from about 260 µm to up to 0.9-1 mm at about 4 weeks after irradiation, with single ears even exceeding the 1 mm. Ears increased and declined faster in thickness after 60 Gy than after 40 Gy with a shift of the time course of about 3-5 days, but the final ear thickness of about 320 µm reached after 75-80 days did not differ between the two doses. [17]

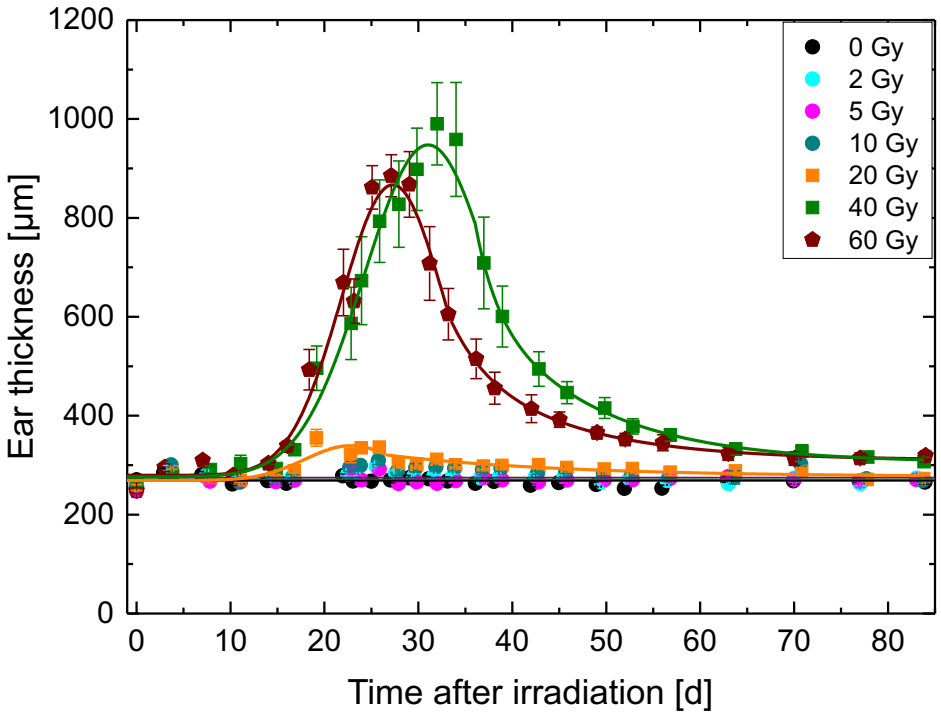

Figure 6.5: *Ear thickness (mean and SEM) of the treated ears measured for 90 days following irradiation with 7 X-ray doses (on day 0). [17]*

Skin reactions were scored on the inner and outer face of the ear. The maximum of the two scores was averaged for the mice of each dose group and plotted in Fig. 6.6. Significant erythema and desquamation (mainly crust formation) of the ear only developed after doses ≥ 40 Gy, with only mild erythema resulting from 20 Gy X-rays (cf. Figures 6.6a and 6.6b). These results are in good agreement with the study of Law [121], where ears of CFLP mice irradiated with ~ 20 Gy showed erythema, but desquamation only occurred for doses > 20 Gy (X-ray). In humans, threshold single doses are 6 Gy for erythema, 14 Gy for dry and 18 Gy for moist desquamation [123]. [17]

Skin reddening and desquamation of the observed mice ears developed in a similar time pattern for the highest doses and was therefore summed up to one skin score in Fig. 6.6c. The highest occurring skin response about 4 weeks after exposure was equal after 40 and 60 Gy, but was reached 1-2 days earlier after 60 Gy. [17]

Photographs were taken once a week for two mice per dose group to visualize skin reactions (day 22/23 shown in Fig. 6.7, time course after 60 Gy in Fig. 6.8). Hair loss in the irradiated square field was first detected 4-5 weeks after irradiation with doses ≥ 40 Gy (Fig. 6.9) [17].

Taking all obtained results into account, a dose of 60 Gy X-ray was selected for the comparative study of proton mini- and broad beam irradiation, leading to significant and measurable inflammation in the mouse ear using X-ray broad beams.

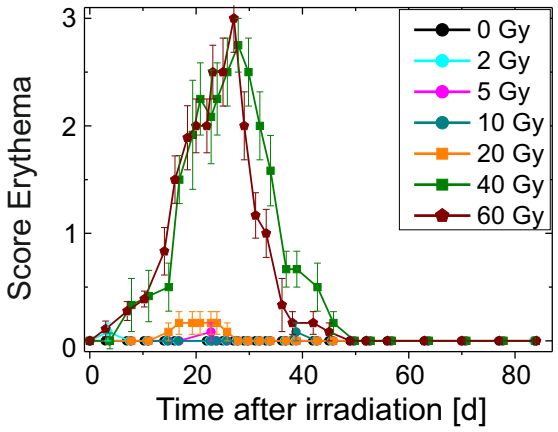

(a) *Skin reddening (erythema) of the treated ears scored with Table 6.1 (A).*

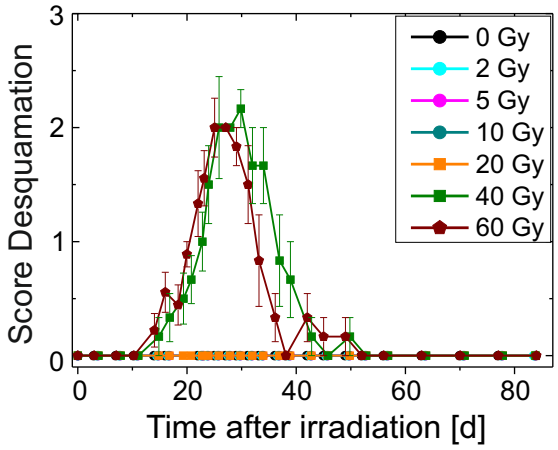

(b) *Desquamation of the right ears scored with Table 6.1 (B).*

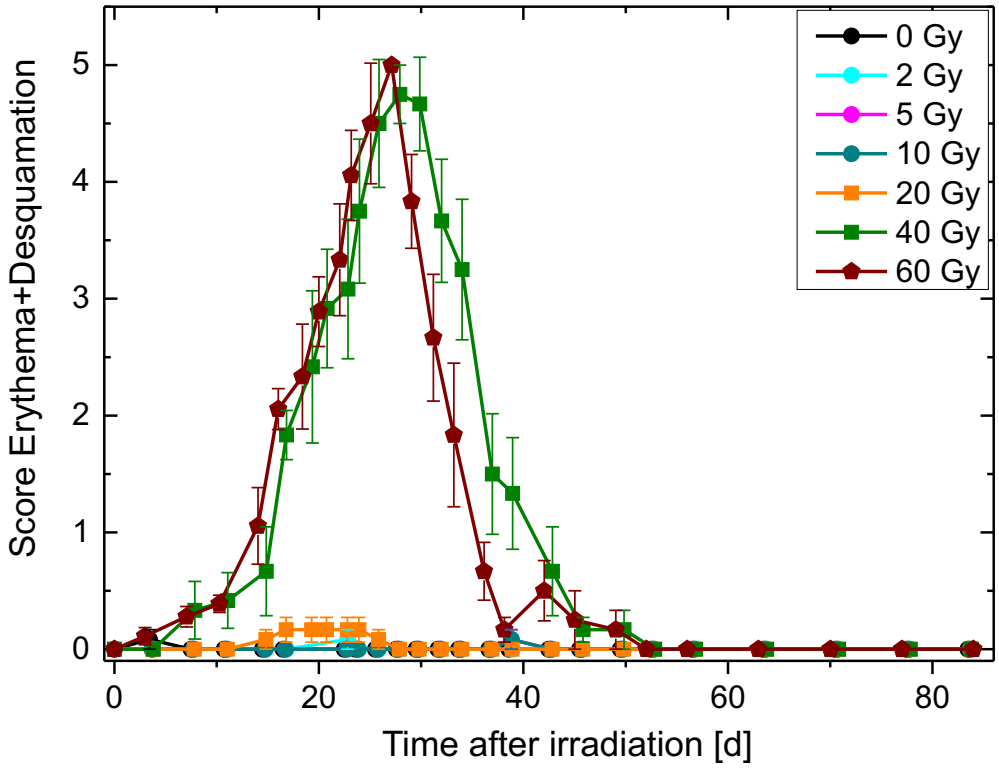

(c) *Complete skin response, i.e. erythema and desquamation, adding up scores A and B of Table 6.1. [17]*

Figure 6.6: *Skin reaction of the treated right ears monitored for 90 days following irradiation with 6 X-ray doses and sham-irradiated controls (0 Gy).*

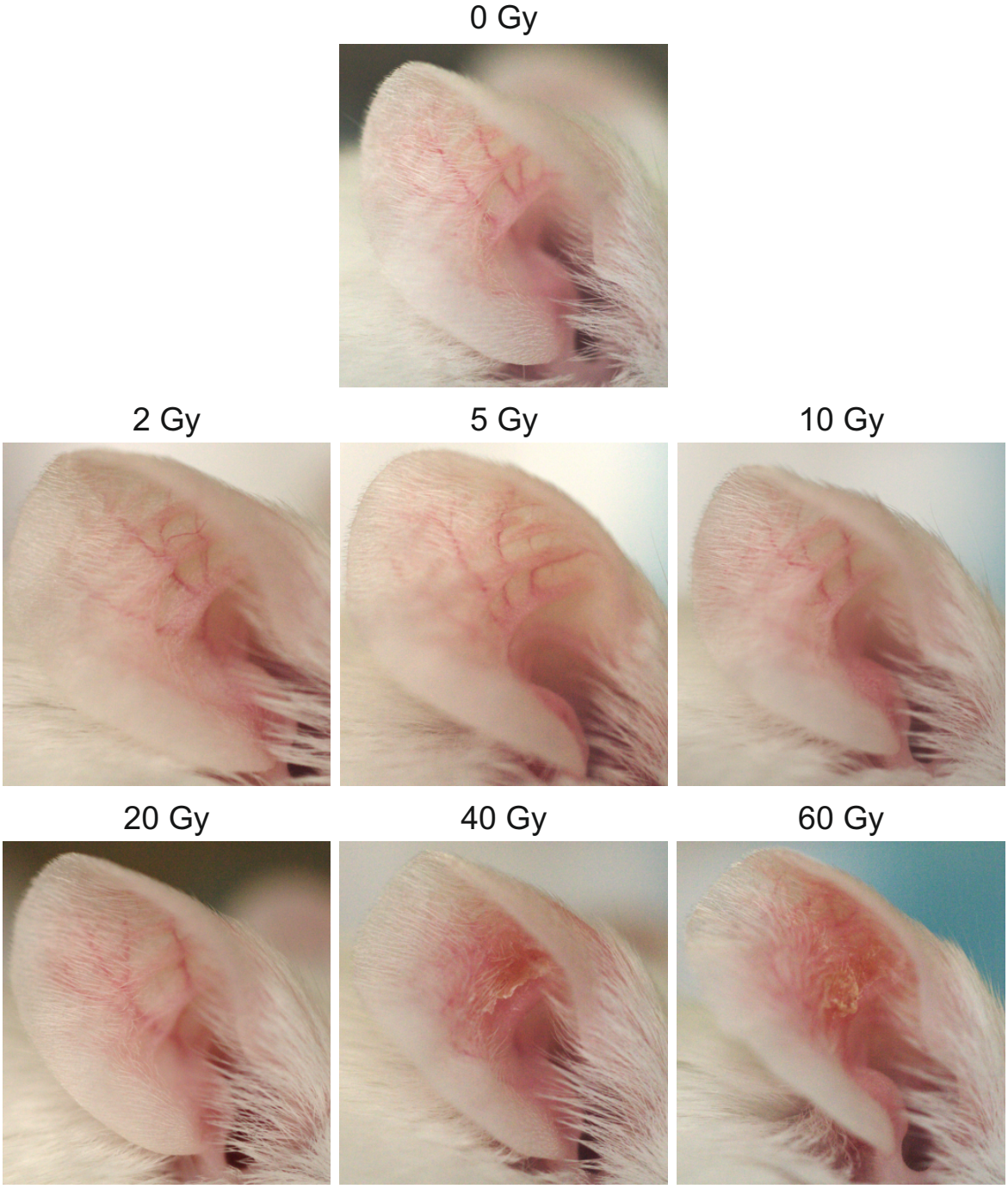

Figure 6.7: *Photographs of mouse ears 3 weeks (i.e. 22 or 23 days) after X-ray irradiation with 6 different doses and controls (0 Gy).*

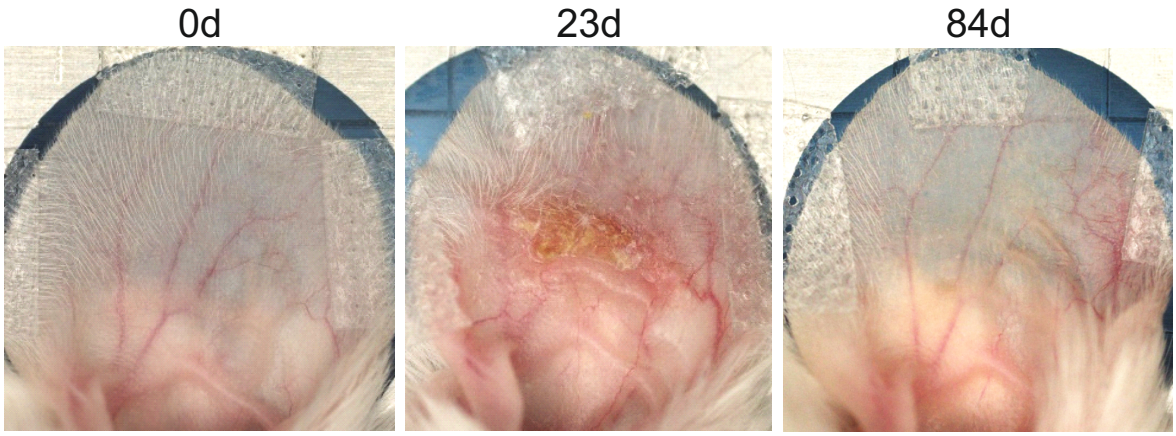

Figure 6.8: *Time course of the skin response after 60 Gy X-ray irradiation (at 0d): waviness, erythema and crust formation at day 23 after irradiation and hair loss in the square irradiation field at day 90 after irradiation.*

Figure 6.9: *Hair loss in the irradiated square field after 40 and 60 Gy X-ray irradiation.*

6.4 Proton irradiation modes

All irradiations were performed under general anesthesia of max. 45 minutes using MMF and AFN (cf. section 6.1). The central part of the right mouse ear was irradiated in a specially developed holder while the mouse was lying on its right side (cf. Fig. 6.10, [124]). The temperature-controlled holder was mounted directly behind the beam exit nozzle in a special adaption to the microscope stage. The rear of the ear was facing the beam, unlike for the X-ray irradiations, where the beam first hit the inside of the ear. However, this is not supposed to lead to significant differences as the thickness of the ear is very small, allowing to approximate the dose as constant across the whole ear profile (increase in LET towards back side of the ear $< 0.08\,\mathrm{keV/\,\mu m}$, i.e. dose increase $< 3\,\%$). [17]

Every proton traversing the ear hit a scintillator-photomultiplier detector attached directly to the mouse holder behind the ear (Hamamatsu H8134P, i.e. R5610P in Mu-metal housing and mounted connecting cables, active area 15 mm diameter) to allow irradiation of large homogeneous fields like in the X-ray study. With the number of counted protons and the measured field and minibeam sizes, the dose was calculated using the LET value of $2.66\,\mathrm{keV/\,\mu m}$ at the ear. However, because of the high particle count rates in the MHz range, which were required for irradiation times of less than 30 minutes and anesthesia below 45 minutes, the dead time of the detection electronics which lead to increased pile-up events had to be corrected using Gafchromic film dosimetry. This was done by entering the number of protons which lead to a certain dose in a defined irradiation field into the counting module and measuring the actually obtained dose with the Gafchromic film. The ratio of the higher measured dose and the defined dose was used to correct for pile-up. A piece of Gafchromic film fixed behind the ear also allowed visualization of the irradiated pattern and verification of correct execution (see Fig. 6.11). [17]

Two different setups were required to prepare the beam for the focused minibeam mode and for homogeneously applied protons. In both cases, the same total number of counted protons (7.34×10^9 p) was applied within an area of $51.84\,\mathrm{mm^2}$ resulting in a mean dose of the specified value of 60 Gy. For the homogeneous irradiations this was achieved with the microprobe's slit system, while a microbeam had to be prepared using the superconducting lens and scanned with the electrostatic deflection unit for the minibeam irradiations (cf. chapter 4). As the vertical and horizontal slits are not perfectly orthogonal, the homogeneous field was not exactly square (cf. Fig. 6.11a) with edge length 7.2 mm as with X-rays, but chosen such that the resulting field had the same total area of $(7.2\,\mathrm{mm})^2$. For the minibeam mode, 4×4 square minibeams of

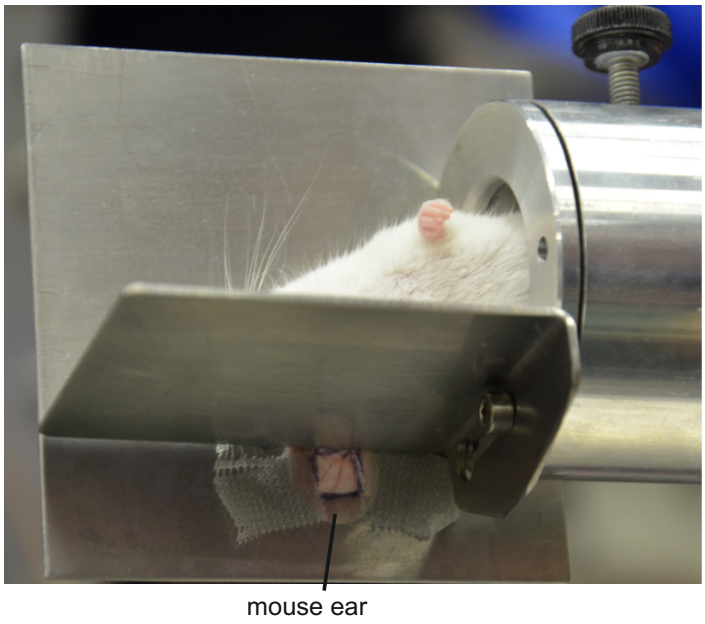

(a) *The mouse is lying in the tube-like jig on its right side with the ear positioned in front of the square hole in the steel plate, allowing the protons to directly hit the ear.*

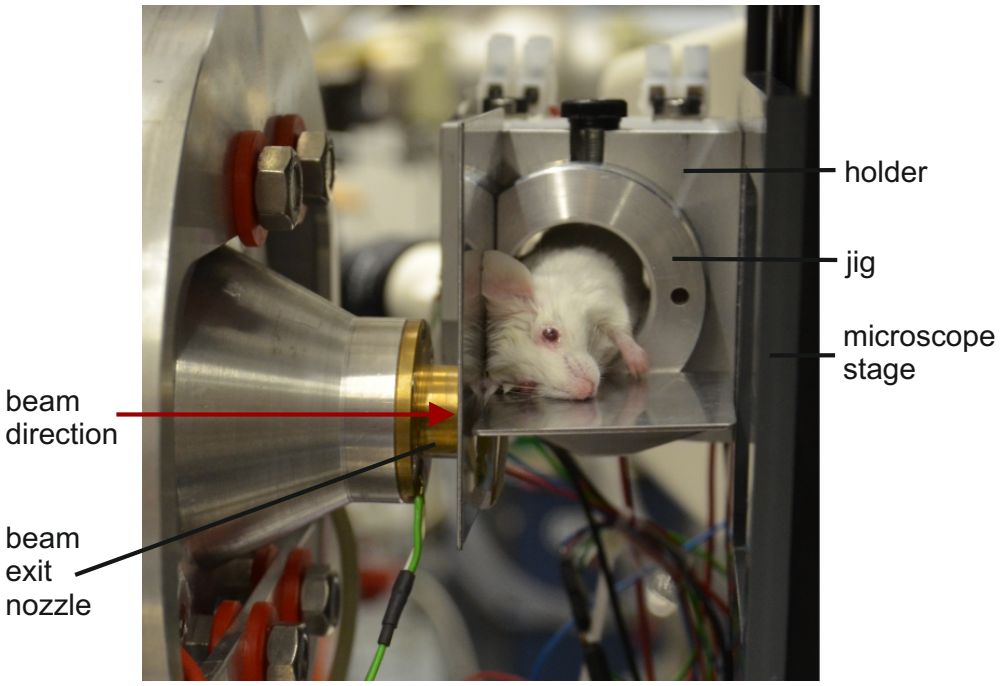

(b) *The jig is placed in the heatable holder mounted to the stage of the microscope. The hole in the steel plate is positioned directly in front of the beam exit nozzle.*

Figure 6.10: *Mouse holder for proton irradiations.*

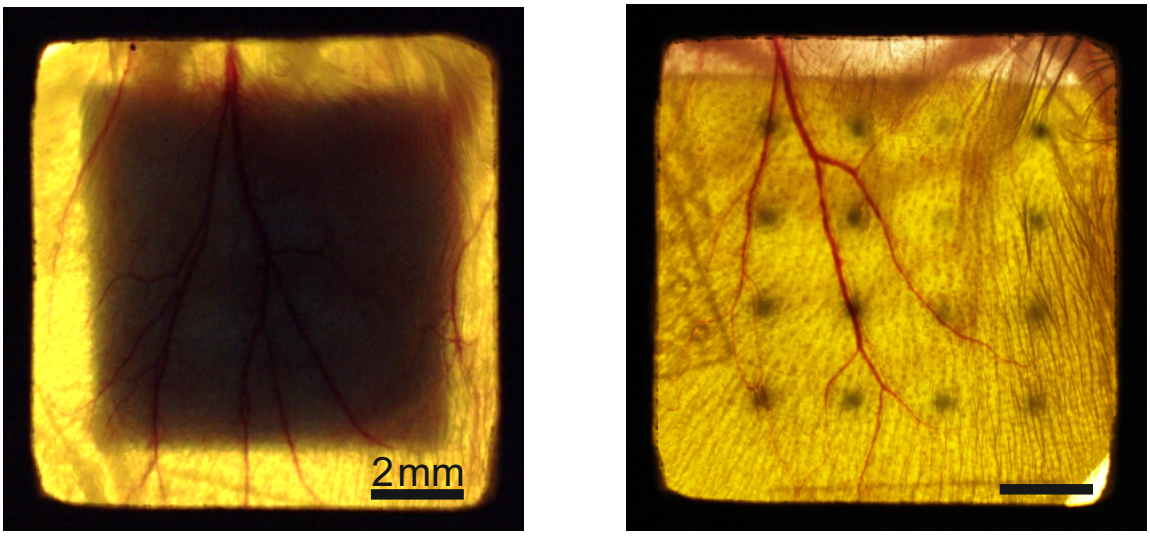

(a) *Homogeneous irradiation with 60 Gy in a field of 51.84 mm².*

(b) *Minibeam irradiation with 16 beams at 180 x 180 µm² in a distance of 1.8 mm.*

Figure 6.11: *Irradiation modes of the proton study: Photography of Gafchromic film positioned behind the mouse ear immediately after irradiation with homogeneous field (a) and minibeams (b). Note the wrong dimensions on the film due to proton scattering in the ear. [17]*

size 180 x 180 µm² in a distance of 1.8 mm were prepared as in previous skin model experiments (cf. chapter 5, [24, 25]), resulting in a dose of approximately 6000 Gy in the minibeams (4.69×10^8 p/beam), which cover about 1 % of the total area. [17]

Dose distributions of the two irradiation modes were also analyzed using radiochromic films (Gafchromic EBT3, cf. [88]). The measured mean doses of the two irradiation modes were in good agreement with the desired 60 Gy, with (59 ± 5) Gy for the minibeam irradiation mode and (58 ± 6) Gy for the homogeneous mode. For both dose determinations, the number of applied protons had to be downscaled to fit the dose range of the film. The dose uncertainty was mainly determined by the film dosimetry to correct the detector dead times of ~ 15 % for HF and ~ 35 % for MB at the required high count rates and the uncertainty of the field sizes. [17]

6.5 Results of the in-vivo mouse ear study

The follow-up after irradiation for the acute radiation response lasted 90 days, with regular monitoring of the animals' health state, ear thickness and skin reaction, adapted to the severity of the acute reaction.

6.5.1 Ear swelling

Thickness of irradiated and unirradiated ears were measured at regular intervals in order to discover swelling and decrease as early as possible. The average ear thickness of each irradiation group is plotted in Fig. 6.12a for the monitored 90 days. After minibeam irradiations, no increase in ear thickness was detected at any time, i.e. control levels were never exceeded within the measurement accuracy of about 10-15 % (cf. Figure 6.12a). Like in the X-ray pilot study, homogeneous irradiation with 60 Gy lead to significant swelling of the ear of almost four times the initial thickness, i.e. up to 1 mm. The average maximal thickness was reached about 25 days after irradiation, but the individual curves of the 12 HF irradiated mice differed in shape and peak height (cf. Appendix D). Comparison with the X-ray study show a very similar response for ears irradiated with 60 Gy protons and X-rays, with comparable maximal thickness and temporal development (Fig. 6.12b). [17]

For evaluation of the effect of the minibeam irradiations, the homogeneous dose which yielded an equivalent response with respect to ear swelling had to be determined. As no major differences between 60 Gy X-ray and proton irradiation were observed regarding ear swelling, the measured X-ray curves were used to determine the minibeam-equivalent homogeneous dose. Because the initial ear thickness differed between the proton and X-ray mouse batch (approx. 25 µm), the ear swelling, i.e. the difference between right (irradiated) and left (unirradiated) ear was used for this comparison. Ear swelling was calculated for every mouse ($i = 1 - N$) and every time point (t_j) independently using the mean thickness of the left ear from all measurements ($\overline{left}$) and then averaged over the whole dose group for each day:

$$swelling(t_j) = \frac{1}{N}\sum_{i=1}^{N} right_i(t_j) - \overline{left}_i \tag{6.1}$$

20 Gy of X-rays lead to a significant increase from control levels from about 20 days until approximately 74 days after irradiation and thus yielded significantly higher ear swelling than minibeam irradiation ($P < 0.001$, cf. Fig. 6.13). During this time interval of approximately 50 days, and a homogeneous dose of 10 Gy (X-ray) also lead to a significantly higher increase in ear thickness than minibeams ($P < 0.01$). Homogeneous X-ray irradiation with 2 Gy and 5 Gy did not induce significant ear swelling relative to unirradiated controls or in comparison with minibeam irradiation ($P > 0.5$). This implies that a minibeam irradiation with an average dose of 60 Gy induced less swelling than a homogeneous irradiation at 10 Gy (cf. Table 6.3). [17]

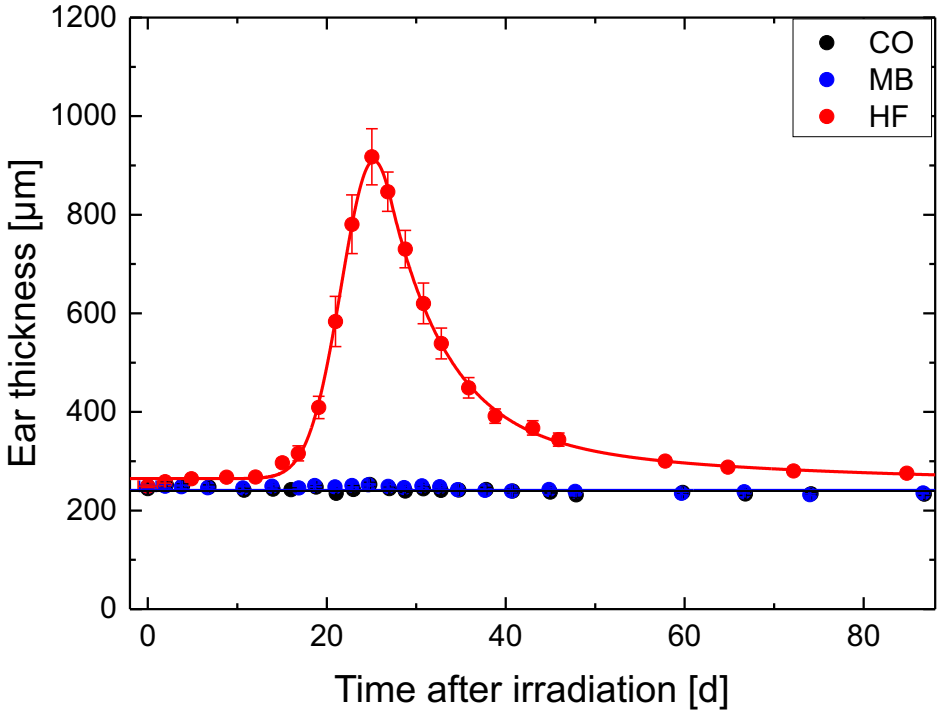

(a) *Mean ear thickness (±SEM) of the right ears following proton minibeam, homogeneous and sham-irradiation.*

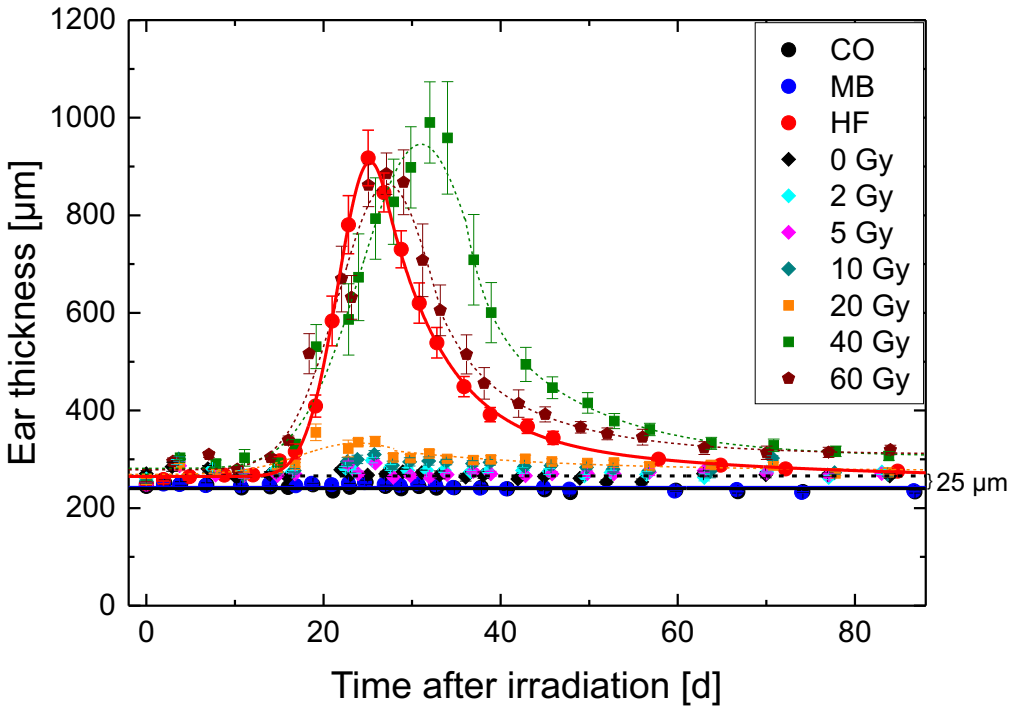

(b) *Mean ear thickness (±SEM) of the right ears following proton and X-ray irradiation. Difference in initial ear thickness between X-ray and proton mice of 25 µm*

Figure 6.12: *Ear thickness (mean and SEM) of the treated ears three months following proton irradiation with minibeams (MB), homogeneous field (HF) and after sham-irradiation (CO). For comparison, X-ray results are included in graph (b). [17]*

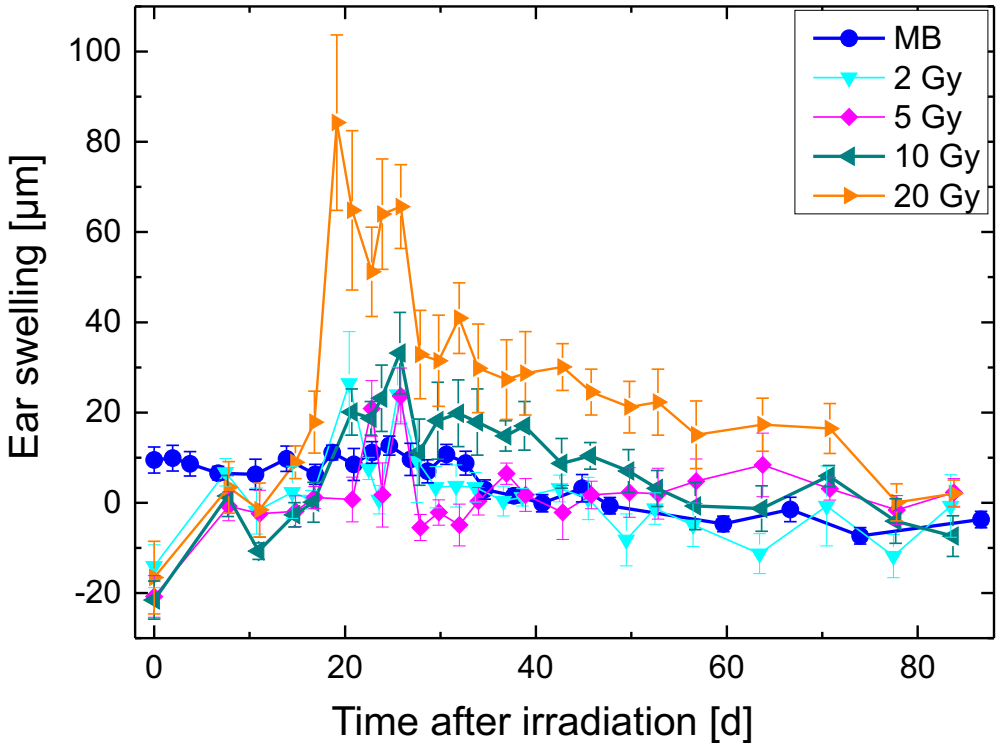

Figure 6.13: *Mean ear swelling (±SEM) of the right ears (compared to left ears) for 90 days following proton minibeam (MB) and X-ray irradiation of 2-20 Gy (at 0d). [17]*

6.5.2 Ear skin response

Ear reddening, desquamation and all other visible skin reactions were monitored at the same frequent time points as ear thickness. For ears irradiated with minibeams, no skin reaction or hair loss was visible at any time (cf. Fig. 6.14 and 6.15). This response is equivalent to the reaction of ears irradiated with X-rays of doses ≤ 10 Gy, whereas mild erythema occurred around 3 weeks after irradiation with 20 Gy, but not with 10 Gy (cf. section 6.3.2). [17]

Homogeneous proton irradiation with 60 Gy lead to comparable skin reactions as seen in X-ray irradiations of the same dose (Fig. 6.16): mild skin reddening appeared first about 9 days after irradiation (Fig. 6.15a), while dry desquamation was first detected around day 17 (Fig. 6.15b). Definite and even severe erythema, together with crust formation and partly moist desquamation developed from approximately day 20 and reached its maximum at about 25 days after irradiation, just like swelling of the ear. Additionally, changes of the ear morphology like bends, waviness and stiffness accompanied erythema and desquamation in several homogeneously irradiated ears (see Fig. 6.14; not included in the score).

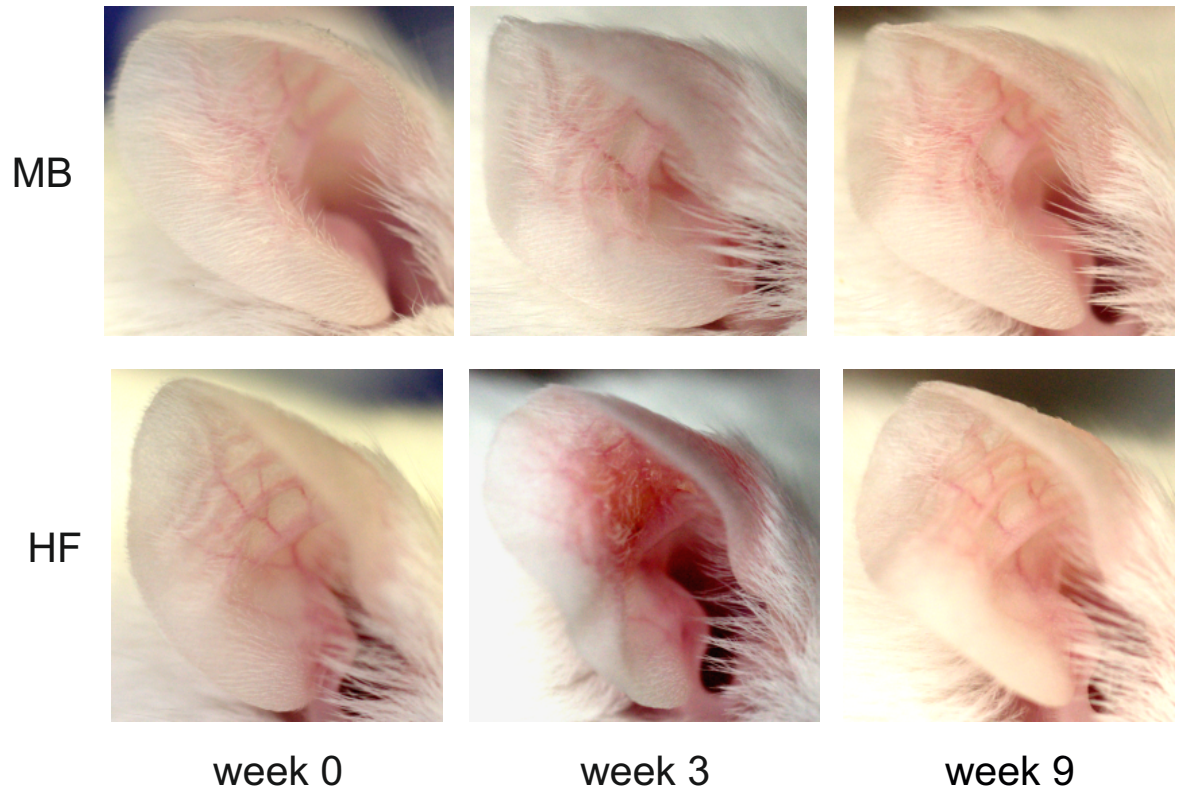

Figure 6.14: *Time course of the skin response after minibeam (MB) and homogeneous (HF) irradiation.*

After a regression with similar slope as the increase, skin response (i.e. Score A (erythema) + Score B (desquamation)) was back to zero after approx. 46 days, meaning no remaining signs of the irradiation (Fig. 6.15c). Hair loss in the irradiated field became visible after the decline of the desquamation at about 4-5 weeks after irradiation in all 12 mice. [17]

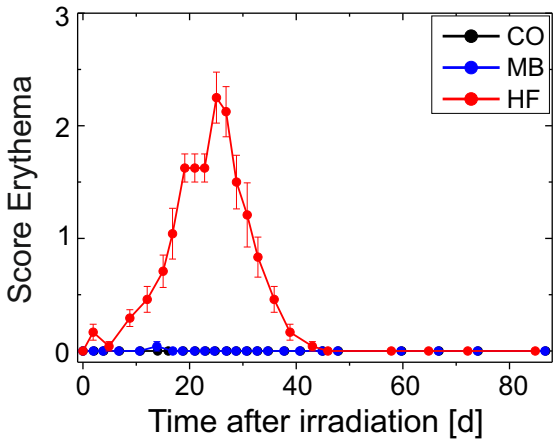

(a) *Skin reddening (erythema) of the treated ears (Score A, Table 6.1).*

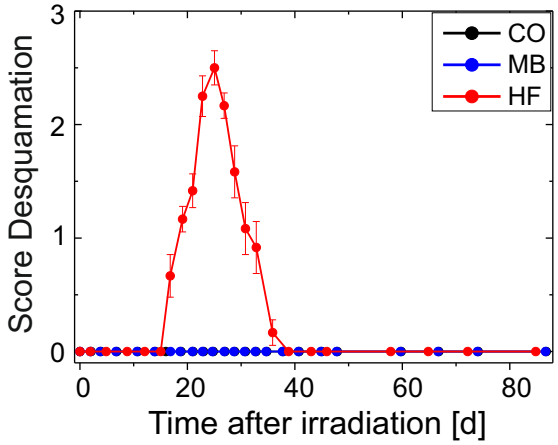

(b) *Desquamation of the right ears scored with Table 6.1 (B).*

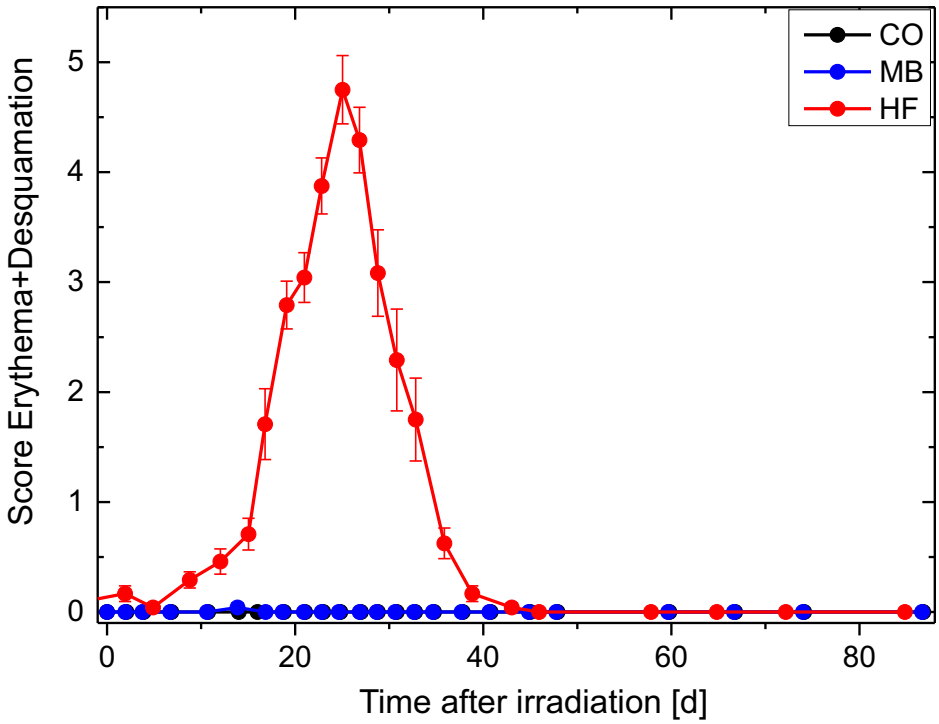

(c) *Complete skin response following proton irradiations, i.e. erythema and desquamation (Score A+B , Table 6.1). [17]*

Figure 6.15: *Skin reaction of the treated right ears monitored for three months following irradiation with minibeams (MB), homogeneous field (HF) and controls (CO).*

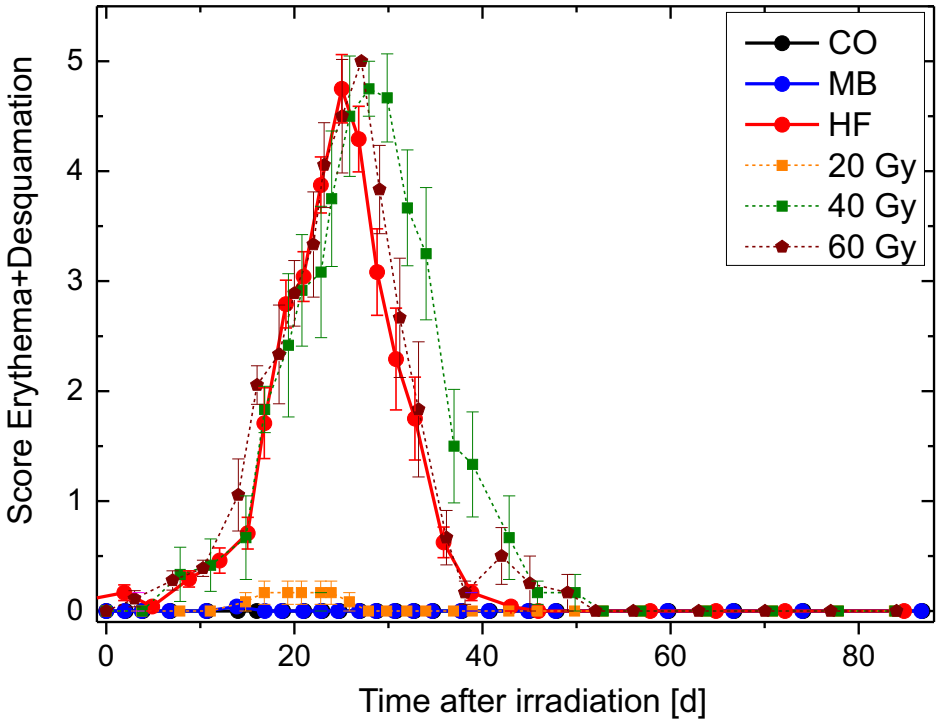

Figure 6.16: *Skin response after proton and X-ray irradiation for the first 90 days after irradiation (only 20-60 Gy, constant score 0 for lower doses, cf. Fig. 6.6c). [17]*

6.5.3 Histological findings

Histological sections through the central part of the ear, i.e. through the irradiation field, were prepared for three mice per irradiation group and time point (15, 25, 36 and 90 days after irradiation, Fig. 6.17). Unfortunately, it was impossible to ensure that the cuts go directly through one of the minibeams. Therefore, it cannot be excluded that histological changes occurred in the irradiated spots. However, in the analyzed skin sections no changes could be detected for all analyzed times, representing the majority of the area between the minibeams. [17]

By contrast, homogeneous irradiation lead to significant alterations in ear histology from 15 days after homogeneous irradiation until the end of the monitoring phase after three months (cf. Fig. 6.17). From day 15, sebaceous glands were lacking in the irradiated field, but were still present in the surrounding skin (cf. [50]). The maximum ear swelling and skin score around day 25 (sections 6.5.1 and 6.5.2) correlated well with significant enlargement of the epidermis in both skin layers, accompanied by inflammation and fibrosis (cf. [50]). Fibrosis is the excessive production of fibrous connective tissue mainly by fibroblasts, resulting from inflammation or disturbed blood flow and leading to scarring of the involved tissue [119]. The decline of the swelling of

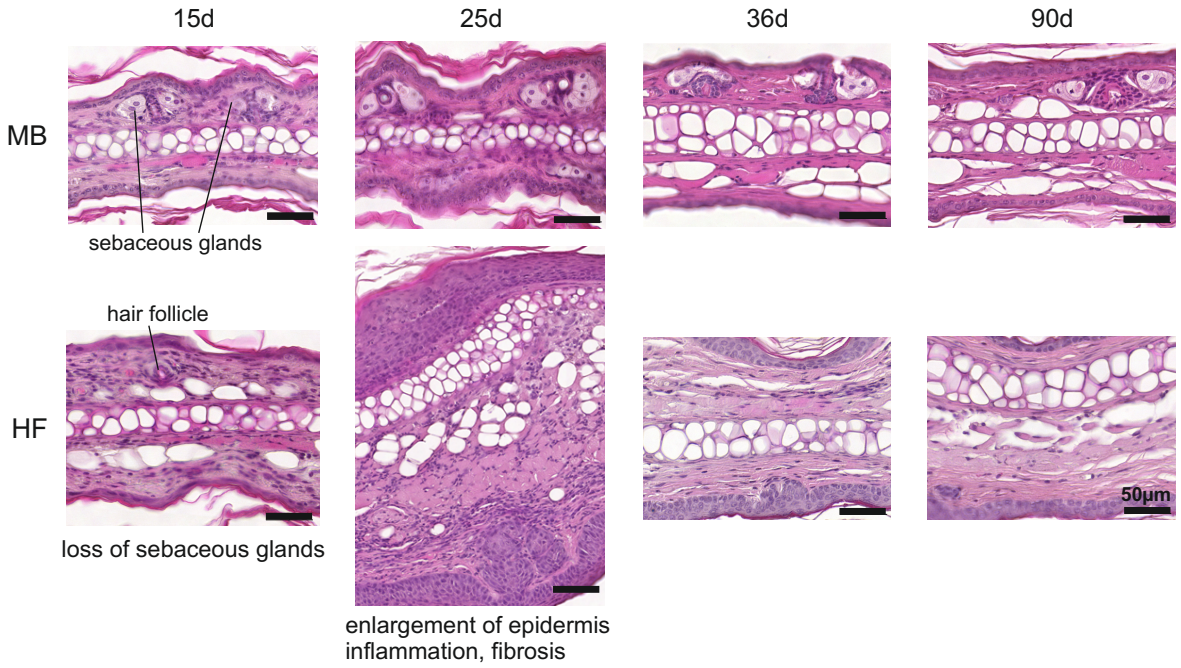

Figure 6.17: *Histological sections of ears irradiated with homogeneous field (HF) and minibeams (MB) at 15, 25, 36 and 90 days after irradiation. Histology of MB-irradiated ears was unchanged at all times, whereas homogeneous irradiation induced the loss of sebaceous glands (from day 15), a significant enlargement of the epidermis, inflammation and fibrosis (cf. control ear in Fig. 6.2). (Note: ears (within each group) are necessarily from different mice.) [17]*

the epidermis and the reduction of the fibrotic area until day 36 and even more until 90 days after irradiation could also be seen in the measurements of the ear thickness (Fig. 6.12a). Nevertheless, fibrosis was still prevailing at the end of the experiment after three months, explaining the still increased average ear thickness compared to the starting point. Furthermore, sebaceous glands in the irradiated area did not recover during the complete monitoring time. A loss of sebaceous glands means no sebaceous secretion and a decrease in surface lipid levels, leading to a reduction of the protective function of the skin barrier against germs and an impairment of the skin milieu, causing sensitive and dry skin [125]. In humans, cumulative doses beyond 12 Gy lead to loss in the function of sebaceous glands, resulting in a typical dry skin especially when perspiratory glands respond as well at slightly higher doses [41]. Surprisingly, abundance and appearance of the hair follicles in the homogeneous irradiation fields was unchanged at all times, but hair growth was still restrained from 4-5 weeks after irradiation until the end. In human hair follicles, single doses of 4 Gy or 10 Gy result in transient or permanent hair loss, respectively. Using fractionation, total doses up to

40 Gy still allow regrowth of the hair within one year, but frequently associated with discoloration/graying [41, 126]. [17]

6.5.4 Chromosome damage in blood lymphocytes

Micronucleus induction in blood lymphocytes is a sensitive biomarker for irradiation, as the micronucleus frequency increases in a dose-related manner after exposure of a certain body part, i.e. blood volume, in radiotherapy [104, 127, 128]. Micronucleus frequencies and distributions in the blood of mice irradiated with homogeneous fields, minibeams and of sham-irradiated controls are given in Table 6.2 and displayed in Fig. 6.18.

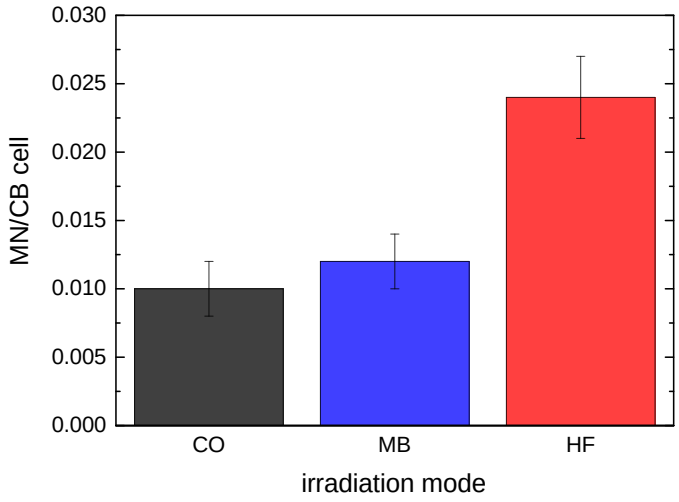

Figure 6.18: *Mean micronucleus frequencies in mouse blood lymphocytes 90 days after irradiation with minibeams (MB), homogeneous field (HF) or sham-irradiation (CO).*

The baseline micronucleus frequency in peripheral blood lymphocytes was 0.010 ± 0.002, as determined at the end of the monitoring period in unirradiated controls. Micronucleus abundance in the lymphocytes of minibeam irradiated mice was not significantly different from controls (0.012 ± 0.002; $P > 0.5$), meaning no detectable evidence of the irradiation in the blood. For mice irradiated with a homogeneous dose distribution, MN frequency doubled (0.024 ± 0.003) compared to control mice, indicating a clear and measurable effect of the irradiation on the blood.

Mouse number	Irrad. mode	Analyzed cells	MN per CB cell (± SE)	Intercellular MN distribution			
			y	0	1	2	3
1	CO	500	0.012±0.005	494	6	0	0
2	CO	500	0.006±0.003	497	3	0	0
3	CO	500	0.006±0.003	497	3	0	0
6	CO	500	0.012±0.006	495	4	1	0
7	CO	500	0.014±0.005	493	7	0	0
Σ CO	**CO**	**2500**	**0.010±0.002**	**2476**	**23**	**1**	**0**
11	MB	500	0.012±0.006	495	4	1	0
12	MB	500	0.016±0.006	492	8	0	0
13	MB	500	0.016±0.007	494	4	2	0
16	MB	500	0.010±0.004	495	5	0	0
17	MB	500	0.006±0.003	497	3	0	0
67	MB	500	0.014±0.005	493	7	0	0
Σ MB	**MB**	**3000**	**0.012±0.002**	**2966**	**31**	**3**	**0**
21	HF	500	0.022±0.007	490	9	1	0
22	HF	500	0.036±0.010	485	12	3	0
23	HF	500	0.016±0.006	492	8	0	0
26	HF	500	0.020±0.008	493	5	1	1
27	HF	500	0.018±0.007	492	7	1	0
69	HF	500	0.030±0.008	485	15	0	0
Σ HF	**HF**	**3000**	**0.024±0.003**	**2937**	**56**	**6**	**1**

Table 6.2: *Micronucleus data in blood lymphocytes*

In order to understand the difference between broad beam and minibeam irradiation with respect to micronuclei induction in blood lymphocytes, it is necessary to estimate the average dose to the blood and the irradiated blood volume in both modes. With a blood speed of 0.5-2 mm/s in the capillaries (the faster speed in blood vessels is neglected due to the small percentage of vessels in the irradiation field compared to capillaries), it takes about 4-15 s until the blood has crossed the homogeneous irradiation field of edge length 7.2 mm. This relates to a blood exchange of 80-375 times in the irradiation field during the 20-25 minutes of irradiation, corresponding to a mean dose of 0.2-0.75 Gy to the irradiated blood. Doses in this order of magnitude can cause increases of the MN frequency in the irradiated lymphocytes, e.g. 1 Gy whole-body X-ray irradiation increased the number of micronuclei by a factor of 20 compared to

controls 1-2 weeks after irradiation [128]. As in our case the irradiated blood volume is smaller, an estimate has to be obtained by assuming that the blood content in the ear is the same as in the rest of the body, so that the relative blood volume in the irradiation field over the irradiation time compared to the whole blood volume can be determined by using the relative weight of the irradiated field compared to the body weight ($V_{blood\ in\ irradiated\ field}/V_{whole\ blood} = m_{irradiated\ field}/m_{body}$) and multiplying this with the number of blood exchanges. The weight of the irradiated tissue ($\sim 0.013\,\mathrm{g}$, assuming a density of $1\,\mathrm{g/cm^3}$) is only about 0.5 ‰ of the total body weight ($\sim 25\,\mathrm{g}$) multiplying this by the factor 80-375 of blood exchanges, meaning a fraction of 4-18 % of the total blood receiving a mean dose of about $0.5 \pm 0.2\,\mathrm{Gy}$. This should therefore lead to an increase in MN/CB cell by a factor of 0.8-3.6, reduced by the lower induction rate at 0.5 Gy compared to 1 Gy, which has not been determined by Fenech et al. [128]. The measured doubling of the MN frequency compared to unirradiated lymphocytes can thus be attributed to the fraction of cells irradiated with sublethal doses of about 0.5 Gy, which are still present in the blood due to their long life-time of about 120 days [129].

For minibeam irradiations, the blood crosses one beam of size 180 µm in 0.1-0.4 s, meaning a blood exchange of 200-900 times in the $\sim$ 1.5 minutes it took to irradiate one minibeam. This corresponds to a mean dose of 7-27 Gy to the irradiated blood cells, so that many cannot be stimulated to divide anymore after 90 days as they have been removed by apoptosis or necrosis [129]. Furthermore, the irradiated blood fraction can be approximated to only about 0.3 ‰ of the whole blood volume, so that the cells receiving sublethal doses which are scored in the MN test cannot contribute to a significant increase in the micronucleus frequency.

Therefore, the micronucleus assay in the blood lymphocytes is sensitive for irradiation with homogeneous broad beams, but not with minibeams 90 days after exposure.

6.6 Conclusion

The murine in-vivo skin model of BALB/c ears was utilized to compare minibeam irradiation and conventional homogeneous proton irradiation of the same average dose (60 Gy) with respect to acute side effects like ear swelling and other skin reactions in the first three months after irradiation. 16 minibeams of 180 x 180 μm^2 size with inter-beam distances of 1.8 mm covered the same area of $\sim 52\,mm^2$ as the homogeneous field. Ear thickness was measured with a specially-adapted measuring gauge and was significantly increased after homogeneous irradiation, reaching up to four times the initial thickness of $\sim 250\,\mu m$ about 3-4 weeks after irradiation, while no swelling occurred at any time after minibeam irradiation. Acute inflammation, quantified via the reddening and desquamation of the irradiated ear, did not appear at all after minibeam irradiation, while severe erythema and crust formation or even moist desquamation developed around 3-4 weeks after homogeneous irradiation. Furthermore, ear morphology was changed in many homogeneously irradiated ears as well as hair was lost in the irradiation field from about 4-5 weeks after exposure. Histological analysis supported the findings of the visible examinations, showing no changes at all for minibeam-irradiated ears, but an enlargement of the epidermis at the time of the highest ear swelling together with large inflammatory and fibrotic regions after homogeneous irradiation. Despite a reduction of fibrosis towards the end of the study, histology was still changed from controls on day 90, explaining the still increased ear thickness compared to the start. From day 15 after homogeneous irradiation, sebaceous glands were lost in the irradiated skin and did not recover until the end of the experiment after three months.

The effects of minibeam irradiation on the skin of the mouse ears was also compared to the outcome after homogeneous irradiation at lower doses (analyzed with 70 kV X-rays) in the same system, to evaluate the improvements of minibeam irradiation compared to homogeneous irradiation. Equivalent homogeneous doses were determined for all endpoints by finding the highest (X-ray) dose which produced the same effects as minibeams (i.e. no effects). These values are summarized in Table 6.3 and show the highest sensitivity for ear swelling, where as little as 10 Gy yielded a higher increase compared to the unirradiated ear than 60 Gy minibeam irradiation. All other endpoints only responded to higher homogeneous doses, with desquamation and hair loss being the least sensitive ones, occurring only after > 40 Gy. Therefore, a minibeam irradiation of a mean dose of 60 Gy induced less side effects than a homogeneous irradiation at 10 Gy. [17]

These findings suggest a reduction of acute radiation effects in the skin after radiotherapy, like swelling, erythema, desquamation, loss of hair and sebaceous glands, when proton minibeams are used instead of conventional homogeneous broad beams.

endpoint	**homogeneous HF**	**minibeams MB**	**MB equivalent HF dose**
ear swelling	up to 4-fold	no	$\leq$ 10 Gy
erythema	severe	no	$\leq$ 20 Gy
desquamation	crust and moist	no	$\leq$ 40 Gy
changes of ear morphology	waviness, bend stiffness	no	$\leq$ 40 Gy
hair loss	in irradiation field	no	$\leq$ 40 Gy
histology	loss of sebaceous glands inflammation fibrosis enlargement of epidermis	no changes visible	n.a.

Table 6.3: *Summary of minibeam and homogeneous irradiation effects for all analyzed endpoints. MB equivalent HF dose is the homogeneous dose inducing the same effects as a minibeam irradiation of 60 Gy average dose (determined in the X-ray pilot study). [17]*

The chosen in-vivo murine skin model fulfilled the requirements of a working immune system and high skin complexity with vasculature, hair follicles and glands for the thorough evaluation of the benefits of this kind of radiotherapy method. Further considerations and challenges on the way towards implementation of minibeams in clinical radiotherapy will be discussed in the next chapter.

Chapter 7

Conclusion and Outlook

7.1 Conclusion

In the radiation therapy of tumors, the radiation dose delivered to healthy, normal tissue is kept as low as possible to reduce injuries and tissue damage and thus is often restricting the total dose that can be applied to the tumor itself. However, despite the development of new and more conformal treatment methods and planning techniques, skin reactions cannot always be prevented in the irradiation field [8]. The degree and extent of the skin response depends critically on the total dose delivered to the tumor and thus to the skin over the whole treatment period, the dose in each fraction and also on the size of the treatment field [25]. Acute side effects in the skin typically start as a slight reddening and proceed as definite or severe erythema together with dry up to confluent moist desquamation [8], causing discomfort or even considerable pain for the patient. In the radiation response of the skin, epidermis and dermis are involved [24, 90]. When the keratinocytes in the radio-sensitive basal layer of the epidermis undergo radiation-induced cell death, necrosis and edema develop in the irradiated skin, starting from about two weeks after exposure. Hence, this inflammatory response is found throughout the whole treatment duration and only disappears weeks after the end of therapy [24].

The aim of this work was to investigate if a new irradiation technique termed proton minibeam radiotherapy with sub-millimeter sized proton beams has the potential to minimize the risk of normal tissue damage, particularly in the skin. In the skin, the minibeams are still sharply defined and separated by more than the beam diameter, leaving the tissue in between the minibeams basically unirradiated. With increasing depth in the tissue, the beam width and the valley doses grow continuously due to small angle scattering of the protons. Eventually, this results in a homogeneous dose distribution in the tumor, when the beam diameter reaches the size of the inter-beam

distance. It is well known that normal tissue can tolerate high radiation doses in a small volume [13, 130, 131]. Therefore, spatial fractionation as in grid or sieve therapy [10–12], microbeam radiation therapy [14–16] or proton minibeam radiotherapy leads to tissue sparing and the recovery of the damaged regions is attributed to surviving cells between the irradiated parts. Thus, the valley dose between neighboring minibeams has to be as low as possible to achieve optimal normal tissue tolerance. The main difference of the described proton minibeams compared to approaches using micro- or minibeams of X-rays like at the European Synchrotron Radiation Facility [14, 132] is the irradiation of the tumor with a homogeneous dose like in conventional radiotherapy.

Calculations and simulations using the treatment planning tool LAP-CERR displayed the range of minibeam sizes and distances required to treat tumors in different depths in tissue. Inter-beam distances of a few millimeter can be used to irradiate tumors in several centimeter depth homogeneously, with increasing maximal distances for deeper-lying targets. Initial minibeam sizes determine the fraction and dose of irradiated skin and have to be adapted like-wise to the inter-beam distances and tumor dimensions, but are also limited by existing accelerator and focusing technologies.

First experimental studies at the ion microprobe SNAKE used square minibeams of 10-180 µm edge length and Gaussian-shaped minibeams of 0.6 and 1.2 mm FWHM in an in-vitro human skin model [23–25]. Tissue viability, expression and release of inflammatory proteins (IL-6, TGF-β and Pro-MMP1) into the culture medium and micronucleus induction in epidermal keratinocytes after minibeam irradiation were compared to homogeneous broad beam irradiation at the same mean dose of 2 Gy using 20 MeV protons. All examined endpoints showed the superiority of minibeam irradiation compared to homogeneous irradiation, i.e. tissue viability was about twice as high, release of pro-inflammatory cytokines was significantly lower and micronuclei induction was less than half for minibeams up to 180 µm size. Genetic damage, an indicator for the risk of secondary tumor induction, increased with growing minibeam size and fraction of irradiated skin, but never exceeded the effects of a homogeneous dose distribution. The expression of pro-inflammatory proteins, which was higher for homogeneous than for minibeam irradiations, is related to acute side effects and wound healing [108, 109, 111] and is therefore an important piece of evidence for the development of skin reactions after radiotherapy.

To further examine the development of acute skin reactions after minibeam and broad beam radiotherapy in a more complex skin model and under the influence of the vascular and the immune system, an in-vivo mouse skin model was introduced: the central part ($\sim 0.5\,\mathrm{cm}^2$) of the ear of adult BALB/c mice was irradiated with minibeams ($180 \times 180\,\mu\mathrm{m}^2$, 1.8 mm distance, nominal 6000 Gy) and homogeneous broad beams of

the same average dose of 60 Gy to study the acute skin response and other observable alterations of the mouse ear for 90 days after irradiation. Swelling of the ear or visible signs of acute inflammation could not be detected at any time after minibeam irradiation, supported by unchanged histological sections at 15, 25, 36 and 90 days. By contrast, homogeneous irradiation lead to ear swelling of up to four-fold the initial thickness with a maximum about 25 days after irradiation, manifesting in the histological sections as enlargement of the epidermal layers together with the appearance of large inflammatory and fibrotic regions. These declined towards three months after irradiation, but were still sufficient to cause a significantly increased ear thickness compared to the starting point. Between 3-4 weeks after homogeneous irradiation, ears showed definite to severe erythema and crust formation or in some cases moist desquamation, often accompanied by bends, stiffness and waviness. From 4-5 weeks after exposure, hair loss occurred only in the square irradiation field, while hair follicles were unchanged in histological sections. Loss of sebaceous glands in the irradiated area was first detected in sections from day 15 but did not reappear until the end of the observation, meaning a deterioration of the skin milieu and a degradation of the protective barrier against pathogens after radiotherapy. None of the reactions observed after the homogeneous proton irradiations occurred for the minibeam irradiated ears [17]

From comparison with homogeneous X-ray irradiations of the same mouse ear model, the homogeneous (X-ray) dose which yielded the same radiation effects as proton minibeam irradiation at 60 Gy (i.e. none) was determined to ≤ 10 Gy, corresponding to a dose reduction factor of larger than 6 (cf. [59]). This means a reduction of side effects when using minibeams instead of homogeneous broad beams at the same average dose (required for tumor control), but can also be translated into the option of escalating tumor dose for radiation resistant tumor types and still keeping normal tissue adverse effects at an acceptable extent. In addition, this would also enable hypofractionation in radiotherapy, i.e. the delivery of a lower number of fractions at higher doses, allowing cost reduction and a less exhausting fractionation scheme for the patient, as fractionation is mainly employed to keep side effects in the normal tissue at an acceptable level while controlling the tumor. [24]

7.2 Outlook

The in-vitro and in-vivo skin studies clearly demonstrate the potential of proton minibeam radiotherapy to reduce acute side effects compared to conventional broad beam irradiation and should therefore be considered for application in clinical proton therapy. Nevertheless, there are still a few questions to be answered before the implementation in clinics.

One of them is to better understand tissue sparing by spatial fractionation in order to determine the maximum minibeam size (and corresponding inter-beam distance) that would still significantly reduce normal tissue reactions after radiotherapy compared to conventional treatment schemes. This is of great importance for the technical realization, as minibeams of only 0.2 mm, as used in the presented studies, are not easily attainable with existing accelerator and focusing technologies. New accelerators, beam transport and focusing techniques might be required for sub-millimeter sized minibeams. Synchrotrons, having actively adjustable beam energies, might perform better than cyclotrons in generating proton beams with small energy spread and high brightness, or laser-acceleration might come into play, being currently in development in many research centers. On the other hand, multi-hole collimators in front of the patient, which are much easier to implement using passively scattered or scanned proton beams, could be a first step for clinical application but hold the disadvantages of increased valley doses due to scattering in the collimator and higher neutron doses for the patient. This would also require detailed studies of the dose distributions behind the collimator.

Investigations with microplanar beams showed advantageous outcome after irradiation of the thoracic spinal cord in rats for beam sizes up to 0.7 mm and 4 mm center-to-center distance, using in-beam depth doses of 400 Gy, but a high valley dose of 88 Gy in between [15]. Irradiation of the mouse cerebellum with 1 mm deuteron beams (25 MeV, 140 Gy) already lead to complete destruction after 240 days [55]. This might be explained by the reduced option of vascular repair with increasing beam size, so that the pure volume effect [13] is not sufficient anymore. To understand the influence of the size (and distance) of pencil minibeams in the context of acute skin reactions, further experiments using the in-vivo murine skin model are planned at SNAKE in the context of a master thesis. Single minibeams and a set of minibeams in the matrix of 1.8 mm as in previous experiments will systematically be enlarged to determine the threshold for the tissue tolerance towards minibeam irradiation. Gaussian-shaped beams will be employed instead of the previously used square beams, as this is the more realistic beam shape for future applications in therapy. If larger inter-beam distances became of interest, there would also be the possibility of irradiating the back or bottom of

the mice using lower beam energies of only up to 10 MeV, to avoid influences of tissue damage in deeper-lying tissues where the protons stop.

For elaboration of possible fractionation schemes, it will be important to understand what happens in the tissue hit by the minibeams with high radiation doses, i.e. if it will be important to position the minibeams again at the exact same location or if this is not necessary (cf. [18]). Presumably, the cells hit by the high doses in the beams will undergo apoptosis or necrosis soon after irradiation and will be replaced by the surrounding cells. In order to find out how long it takes to "close" the tracks of the minibeams, time series of hours up to days after irradiation could be helpful, using for example γ-H2AX or live/dead staining to visualize the irradiated cells or the induced DNA damage in the hit cell nuclei (cf. [65, 133]). Similar investigations after microplanar beam irradiation still showed DNA damage in the irradiated slices 84 hours after exposure, but did not examine if positively-stained cells disappeared at any later time [65].

On the road to clinical use, it will also be necessary to examine the complete irradiation scenario from the skin to the tumor in a suitable (larger) animal model, in order to demonstrate that the simulated minibeam spreading is correct and leads to a homogeneous tumor dose and therefore tumor control (especially in a fractionated irradiation scheme). This will also allow for the analysis of the side effects in deeper-lying tissues underneath the skin where the minibeams start overlapping, to ensure that no disadvantages compared to homogeneous irradiation occur in this intermediate region.

The implementation of precise and verified scattering data into treatment planning systems will be of high importance for the generation of reliable dose plans for radiotherapy, as the widening of the minibeams due to proton interactions in different tissues is crucial for the optimization of inter-beam distances and minibeam sizes for a homogeneous tumor dose. Investigations on the impact of set-up and motion errors will also be required for clinical application.

Verification of the dose distributions in the LAP-CERR treatment plans in a water phantom with Gafchromic films in different depths might help to prove that the simulated homogeneous doses in the tumor can really be attained under the used minibeam dimensions (cf. [18]). The application of hexagonal lattices for the minibeam application instead of the square lattices on which minibeams were set in this study could be analyzed for potential further (geometric) sparing of normal tissues.

Appendix A

Generation of treatment plans using LAP-CERR

The treatment planning software CERR has to be opened in MATLAB, while the optimization software Mosek is running. CERR allows loading of three-dimensional computed tomography (CT) images or the creation of simple (water) phantoms. The data is divided into small volume elements (voxels) and the dose is calculated for each voxel separately. CTs of real patients have a resolution of about 2-3 mm in every direction, which is not sufficient for minibeam irradiation with sub-millimeter beam sizes. Therefore the created water phantoms (total size $lx = ly, lz$) should have a resolution of 200-500 µm ($dx = dy, dz$). Rectangular tumors of various sizes (tx, ty, tz) can be created at different depths (d) of the phantom. As the beam direction is set in y-direction, the central point of the tumor is located at (0, d, 0). The "skin" is located around the target with an individually adaptable margin, only in y-direction it should extend up to the depth 0, so that the dose can be calculated for all depths penetrated by the beam.

For the generation of a treatment plan for a model tumor in a (water) phantom the following steps have to be performed.

1. Create a phantom:

   - load existing phantom (patient)

   - type "createMyPhantom($lx + 2dx, ly + 2dy, lz, dx, dy, dz$, $borderpercentage$, $indexofexistingscan$)", where $lx = ly$, $dx = dy$ and all parameters in cm. For a tumor in a depth $d_{min} - d_{max}$ the phantom length ly should be larger than d_{max}.

     Example: createMyPhantom(10.04, 10.04, 7, 0.02, 0.02, 0.02, 0, 1) with a resolution of 200 µm.

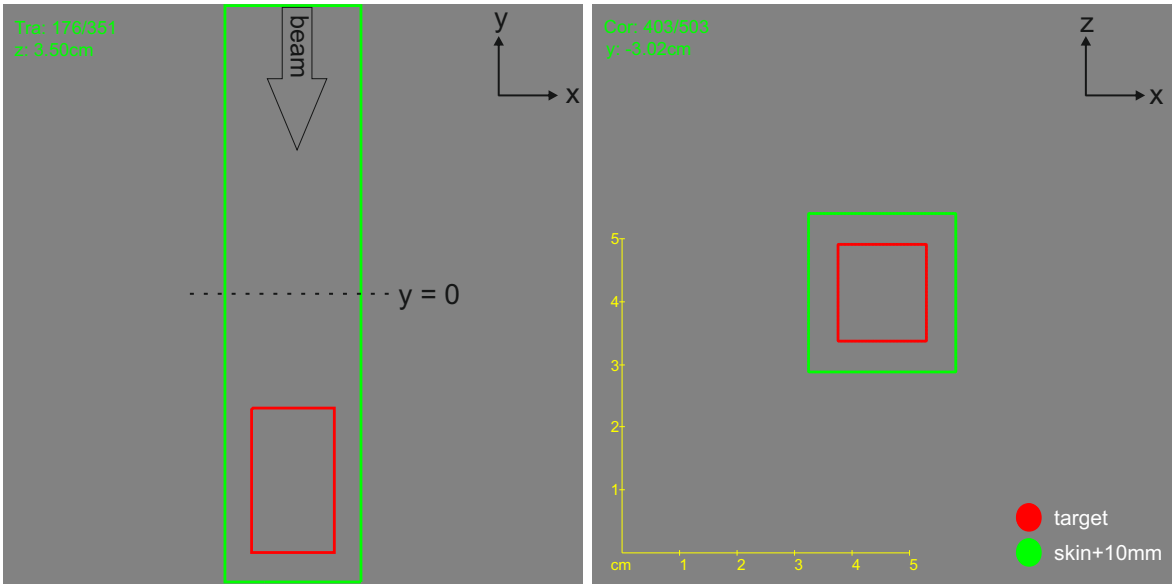

Figure A.1: *Transversal (left) and coronal (right) view of a water phantom (grey) with target structure (red) and surrounding skin structure (green). The tumor of 15x25x15 mm^3 size is lying in a depth of 7-9.5 cm of the water phantom and the skin has a margin of at least 1 cm around the target.*

- type "global planC", "indexS=planC{end}", "planC{indexS.header}.archive = 'phantom_name'" to name the new plan
- change to the new phantom in CERR and delete the old phantom (Scan Management -> delete Scan 1; Dose Management -> delete Dose 1)

2. Create structures:

- draw arbitrary structure in the phantom (Structures -> Contouring -> chose Category (any), create, save)
- create a structure: "createMyStructure(tx, ty, tz, *type*, x, y, z, *name*)" with size tx, ty, tz at the position x, y, z in the phantom. Note that $y = 0$ is in the center of the phantom (i.e. in a depth $ly/2$) and for a central position in z-direction, $lz/2$ is required[(1)]

  For a tumor e.g.
  "createMyStructure(1.5, 2.5, 1.5, 'target', 0, -3.25, 3.5, 'target1')" which lies in the depth 6.75±1.25 cm in the above phantom.

[(1)] Attention: In the generated treatment plan (planC{1,7}.doseArray(i,j,k)) the depth will be indexed by i and not j.

For the skin surrounding this tumor,
"createMyStructure(2.5, 10, 2.5, 'skin', 0, 0, 3.5, 'skin+10mm')" will contour normal tissue around the tumor in which the dose calculation will take place (see Fig. A.1).

- delete arbitrary structure (CERR Command Line Help -> Delete Structure 1)

3. Save the new treatment plan and add the new "patient" in readSettingsPatient.m as follows:

```
elseif strcmpi(name, 'phantom_name')
% targets:
% 1: target25mm (number 1 if tumor has been created first)
patientSettings.targetStructsV = 1;
patientSettings.targetStructsGoalsV = 100; % prescribed tumor dose
patientSettings.targetStructsPenaltiesV = 1000; % higher value for higher importance
                                                to achieve the prescribed dose
% non-targets:
% 2:skin+10mm
patientSettings.nonTargetStructsV = 2;
patientSettings.nonTargetStructsGoalsV = 0;
patientSettings.nonTargetStructsPenaltiesV = 1;

% master struct:
% 2: skin+10mm
patientSettings.masterStruct = 2;
patientSettings.dvhStructNumsV = [1 2];
```

4. For dose calculations, the readSettingsParticles file has to be set to the following parameters (otherwise default values):

```
particleSettings.modality = 'protons';
particleSettings.marginForSubletsAroundTarget = 0.1; % 0.5
particleSettings.deltaRadDepth = 0.01; % 0.05 or 0.5
particleSettings.doseDeliveryMethod = 1; % spot scanning
particleSettings.useTwoSigmasLateralDoseModel = true; % lateral dose model with
                                                      2 Gaussians
particleSettings.lateralCutoffDistanceInMultiplesOfTheLateralSpread = 4;
particleSettings.sigma0Sqr = (0.01)^2; % initial beam width (in cm)
```

When the patient file is loaded in CERR, IMRTP Creation has to be opened: one or more beams can be used for irradiation from defined directions (gantry angle 0 usually) and beamletDelta_x and beamletDelta_y are the distances between neighboring pencil beams in both directions (e.g. 0.18 (cm) for 1.8 mm distance). For homogeneous irradiation, these distances should not exceed twice the initial beam width (sigma0). "Target" and "skin+10mm" have to be chosen as "Structures" and "isTarg" has to be checked for "target" (sampRate = 1 for both). DoseTerm should be set to "GaussPrimary+scatter" and all other parameters default. The scatter of the dose can be suppressed by choosing the "Threshold" option and selecting a low threshold. Then under "File" the dose calculation can be performed ("dose") and subsequently the plan can be optimized ("opt").

Appendix B

Micronucleus data of the in-vitro skin study

In the following tables, the micronucleus (MN) frequency and distribution in cytokinesis-blocked (CB) keratinocytes from human skin tissues of Experiment 1-3 are listed. Each experiment was performed in duplicate in two independent beam-times. Results are presented for each individual subexperiment and pooled data can be found in the main text (section 5.4.3).

Minibeam irradiations with 10x10 and 50x50 μm^2 beams and homogeneous irradiation (HF) in Exp.1.

ID number	**Irrad. mode**	**Analyzed cells**	**MN per CB cell (± SE)**	**Intercellular MN distribution**			
				0	**1**	**2**	**3**
1	HF	500	0.074±0.016	475	16	6	3
2	HF	500	0.050±0.012	480	15	5	0
3	HF	500	0.078±0.016	472	20	5	3
Σ1-3	**HF**	**1500**	**0.067±0.009**	**1427**	**51**	**16**	**6**
4	10x10	500	0.024±0.009	492	5	2	1
5	10x10	500	0.018±0.009	495	2	2	1
6	10x10	500	0.030±0.011	490	7	1	2
Σ4-6	**10x10**	**1500**	**0.024±0.006**	**1477**	**14**	**5**	**4**
7	50x50	500	0.030±0.010	489	7	4	0
8	50x50	500	0.028±0.009	489	9	1	1
9	50x50	500	0.032±0.012	491	4	3	2
Σ7-9	**50x50**	**1500**	**0.030±0.006**	**1469**	**20**	**8**	**3**

Table B.1: *Micronucleus data from Exp.1.1 [23]*

ID number	**Irrad. mode**	**Analyzed cells**	**MN per CB cell (± SE)**	**Intercellular MN distribution**			
				0	**1**	**2**	**3**
1	HF	500	0.060±0.013	478	18	3	1
2	HF	500	0.088±0.018	470	20	6	4
3	HF	500	0.078±0.016	473	17	8	2
Σ1-3	**HF**	**1500**	**0.073±0.009**	**1421**	**55**	**17**	**7**
4	10x10	500	0.024±0.011	494	2	2	2
5	10x10	500	0.018±0.008	494	4	1	1
6	10x10	500	0.020±0.008	493	5	1	1
Σ4-6	**10x10**	**1500**	**0.021±0.005**	**1481**	**11**	**4**	**4**
7	50x50	500	0.046±0.014	487	6	4	3
8	50x50	500	0.032±0.010	488	9	2	1
9	50x50	500	0.014±0.007	495	3	2	0
Σ7-9	**50x50**	**1500**	**0.031±0.006**	**1470**	**18**	**8**	**4**

Table B.2: *Micronucleus data from Exp.1.2 [23]*

Micronucleus data from Experiment 2, using minibeams of 100x100 and 180x180 μm^2 size and homogeneous irradiation (HF).

ID number	**Irrad. mode**	**Analyzed cells**	**MN per CB cell (± SE)**	**Intercellular MN distribution**			
				0	**1**	**2**	**3**
1	HF	500	0.058±0.014	481	10	8	1
2	HF	500	0.102±0.020	471	12	12	5
3	HF	500	0.064±0.014	476	17	6	1
Σ1-3	**HF**	**1500**	**0.075±0.009**	**1428**	**39**	**26**	**7**
4	100x100	500	0.036±0.012	488	8	2	2
5	100x100	500	0.028±0.011	493	2	3	2
6	100x100	500	0.020±0.009	494	3	2	1
Σ4-6	**100x100**	**1500**	**0.028±0.006**	**1475**	**13**	**7**	**5**
7	180x180	500	0.018±0.008	494	3	3	0
8	180x180	500	0.016±0.007	494	5	0	1
9	180x180	500	0.014±0.008	496	2	1	1
Σ7-9	**180x180**	**1500**	**0.016±0.004**	**1484**	**10**	**4**	**2**

Table B.3: *Micronucleus data from Exp.2.1*

ID number	**Irrad. mode**	**Analyzed cells**	**MN per CB cell (± SE)**	**Intercellular MN distribution**			
				0	**1**	**2**	**3**
1	HF	500	0.050±0.011	478	19	3	0
2	HF	500	0.064±0.016	481	10	5	4
3	HF	500	0.078±0.017	476	12	9	3
Σ1-3	**HF**	**1500**	**0.064±0.009**	**1435**	**41**	**17**	**7**
4	100x100	500	0.022±0.008	492	5	3	0
5	100x100	500	0.038±0.013	491	2	4	3
6	100x100	500	0.034±0.011	489	7	2	2
Σ4-6	**100x100**	**1500**	**0.031±0.006**	**1472**	**14**	**9**	**5**
7	180x180	500	0.014±0.007	495	4	0	1
8	180x180	500	0.020±0.009	494	3	2	1
9	180x180	500	0.014±0.008	346	3	1	0
Σ7-9	**180x180**	**1500**	**0.015±0.004**	**1335**	**10**	**3**	**2**

Table B.4: *Micronucleus data from Exp.2.2*

Micronucleus test results from Experiment 3. Minibeam irradiations with 180x180 μm^2 beams through Aluminum (180x180*), Gaussian beams ($\sigma \approx 260\,\mu m$ (WB) and $\sigma \approx 520\,\mu m$ (OB)) and homogeneous irradiation (HF).

ID number	**Irrad. mode**	**Analyzed cells**	**MN per CB cell (± SE)**	**Intercellular MN distribution**			
				0	**1**	**2**	**3**
1	HF	465	0.075±0.017	441	15	7	2
2	HF	483	0.093±0.019	455	14	11	3
3	HF	505	0.050±0.013	489	9	5	2
Σ1-3	**HF**	**1453**	**0.072±0.009**	**1385**	**38**	**23**	**7**
4	180x180*	440	0.025±0.011	434	2	3	1
5	180x180*	493	0.034±0.012	483	5	3	2
6	180x180*	503	0.026±0.008	492	9	2	0
Σ4-6	**180x180***	**1436**	**0.029±0.006**	**1409**	**16**	**8**	**3**
7	WB	500	0.046±0.012	484	10	5	1
8	WB	496	0.040±0.012	483	8	3	2
9	WB	466	0.054±0.015	450	10	3	3
Σ7-9	**WB**	**1462**	**0.047±0.008**	**1417**	**28**	**11**	**6**
10	OB	510	0.049±0.013	493	10	6	1
12	OB	459	0.046±0.015	448	5	2	4
12	OB	429	0.049±0.013	413	12	3	1
Σ10-12	**OB**	**1398**	**0.048±0.008**	**1354**	**27**	**11**	**10**

Table B.5: *Micronucleus data from Exp.3.1 [25]*

ID number	Irrad. mode	Analyzed cells	MN per CB cell (± SE)	Intercellular MN distribution			
				0	1	2	3
1	HF	508	0.075±0.016	484	11	12	1
2	HF	518	0.070±0.015	492	17	8	1
3	HF	495	0.061±0.016	477	10	4	4
Σ1-3	**HF**	**1521**	**0.068±0.009**	**1453**	**38**	**24**	**6**
4	180x180*	510	0.026±0.008	498	11	1	0
5	180x180*	460	0.013±0.007	456	2	2	0
6	180x180*	502	0.028±0.011	493	6	1	2
Σ4-6	**180x180***	**1472**	**0.022±0.005**	**1447**	**19**	**4**	**2**
7	WB	509	0.024±0.009	500	7	1	1
8	WB	298	0.057±0.017	285	9	4	0
9	WB	502	0.038±0.011	486	14	1	1
Σ7-9	**WB**	**1309**	**0.037±0.007**	**1271**	**30**	**6**	**2**
10	OB	502	0.054±0.014	484	11	5	2
12	OB	517	0.070±0.015	491	17	8	1
12	OB	516	0.043±0.013	502	8	4	2
Σ10-12	**OB**	**1535**	**0.055±0.008**	**1477**	**36**	**17**	**5**

Table B.6: *Micronucleus data from Exp.3.2 [25]*

Appendix C

Design drawings of the mouse holder for X-ray irradiation

The next four pages display the design drawings for the mouse holder used for the X-ray irradiations, including tungsten collimator, base plate, ear plateau and tungsten shield. The scale on DIN A4 paper is 1:1 for the tungsten shield and 2:1 for the ear plateau and the collimator. For the bigger base plate, the scale is 1:1 on DIN A3.

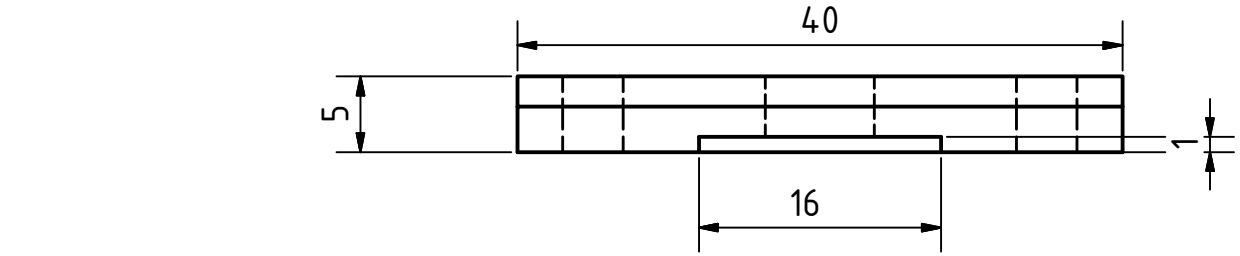

A-A (2 : 1)

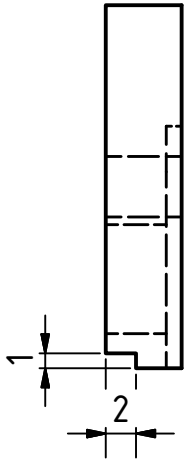

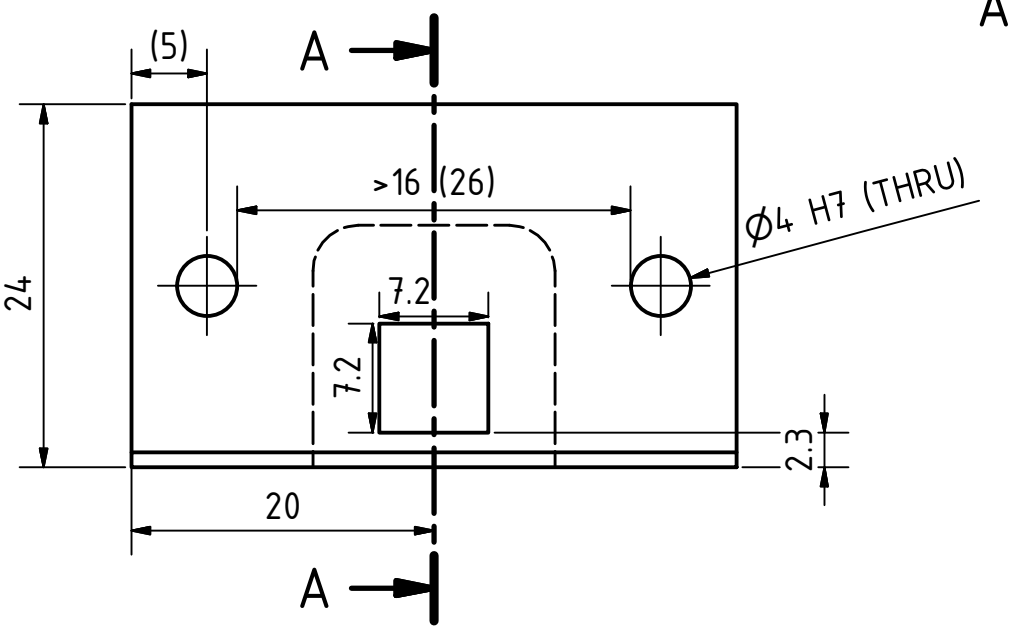

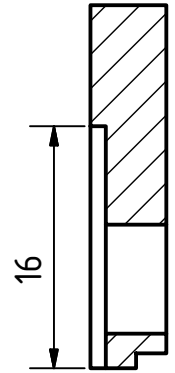

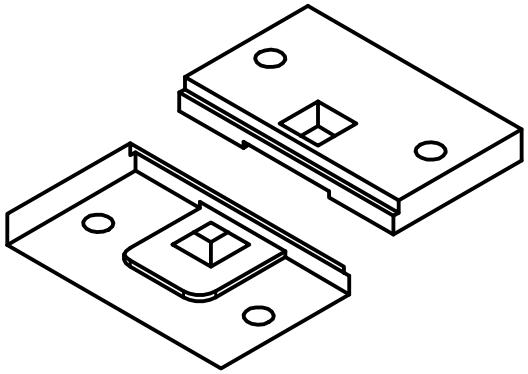

					Datum	Name
				Gezeichnet	17.03.2015	l21bstgi
				Kontrolliert		
				Norm		
Status	Änderungen	Datum	Name			

tungsten_collimator

1

A4

B-B (1 : 1)

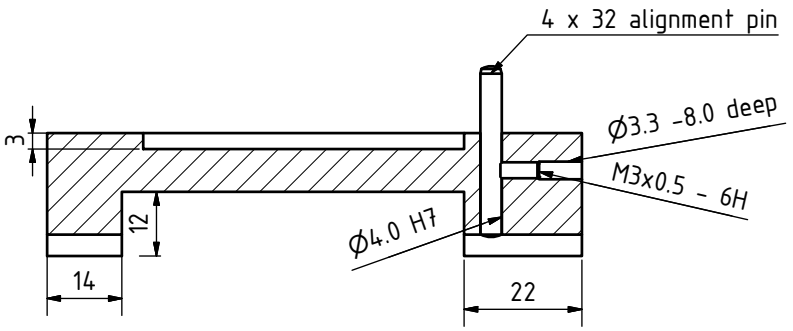

A-A (1 : 1)

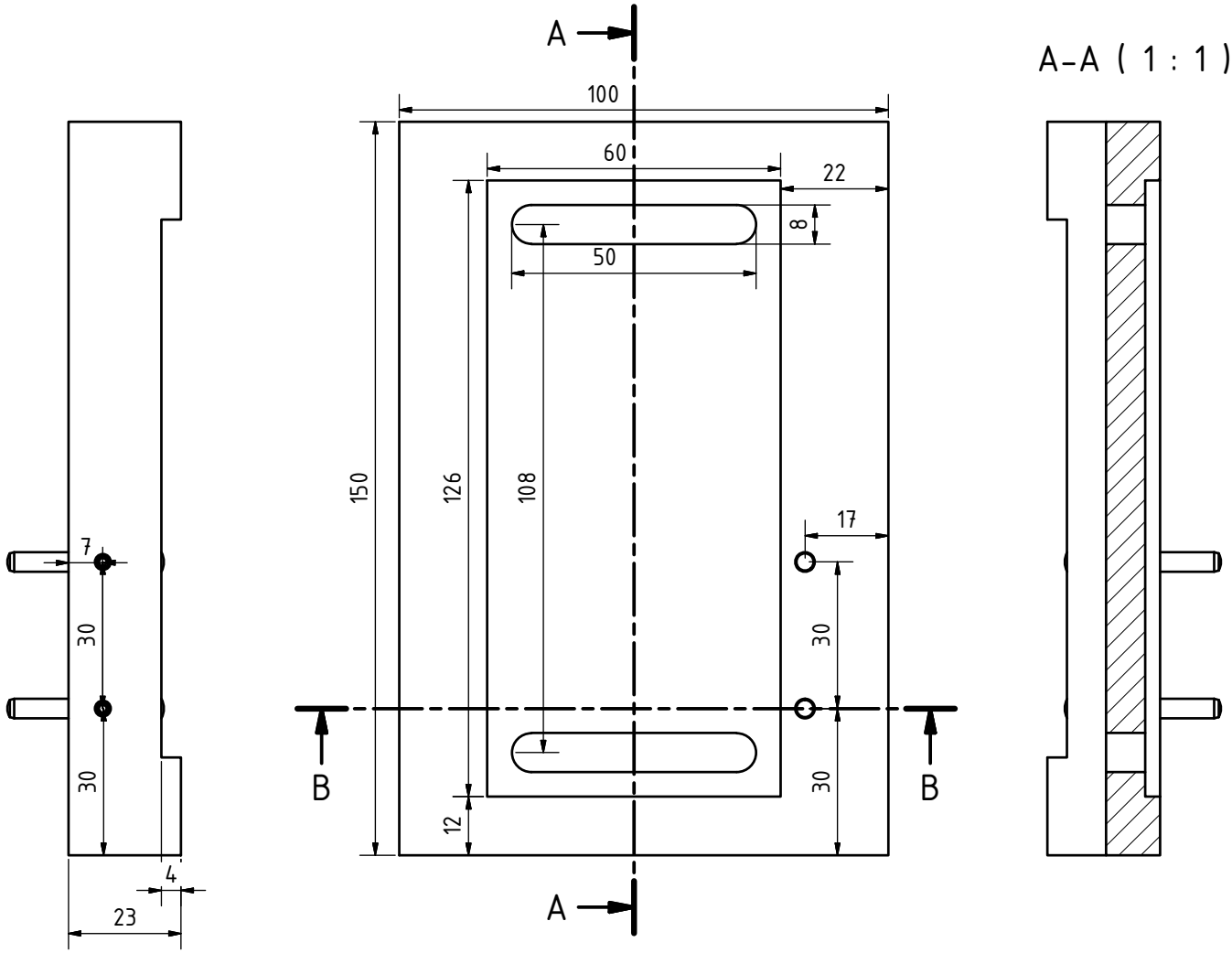

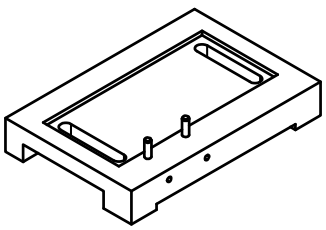

					Datum	Name	
				Gezeichnet	17.03.2015	l21bstgi	
				Kontrolliert			
				Norm			
						baseplate	1
							A3
Status	Änderungen	Datum	Name				

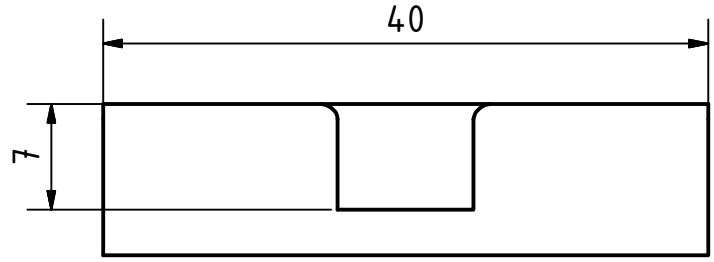

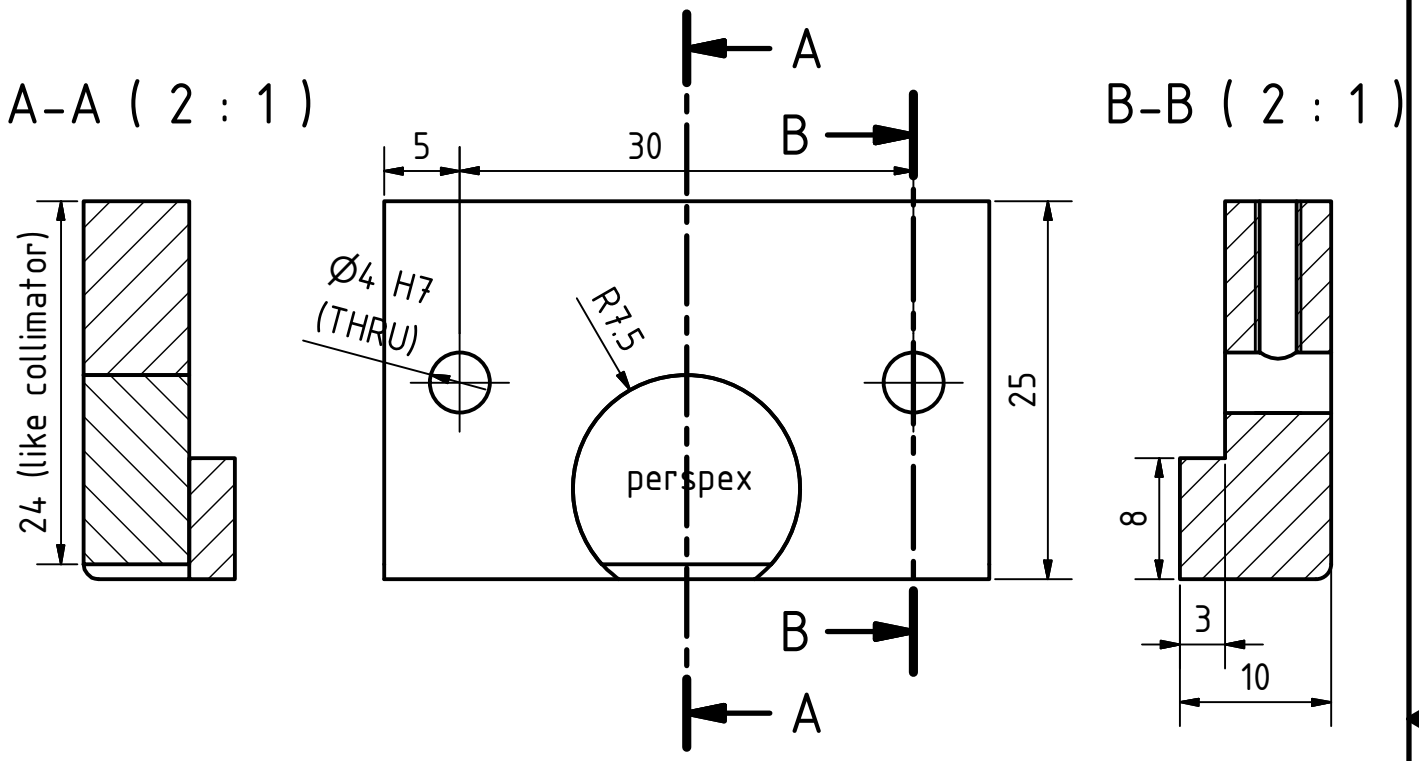

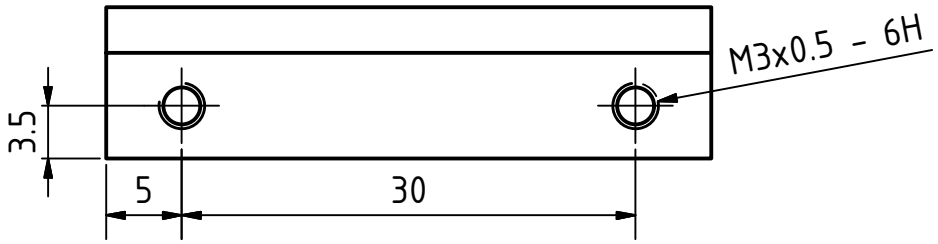

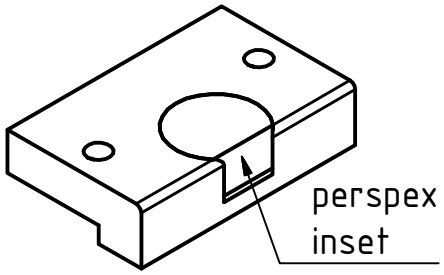

					Datum	Name
				Gezeichnet	10.03.2015	l21bstgi
				Kontrolliert		
				Norm		

ear_plateau+perspex

1

A4

Status	Änderungen	Datum	Name

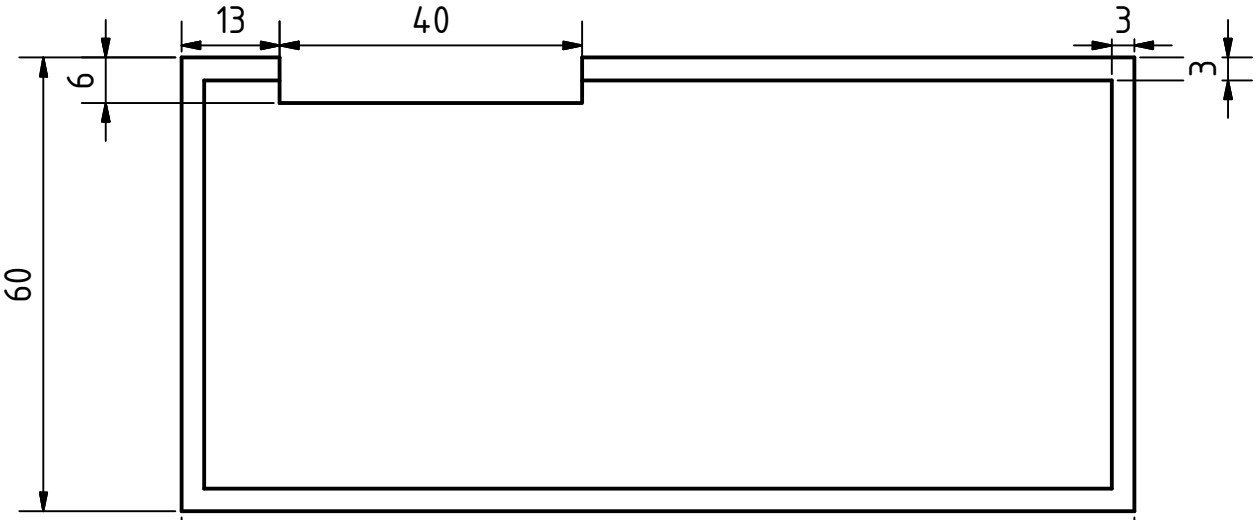

A-A (1 : 1)

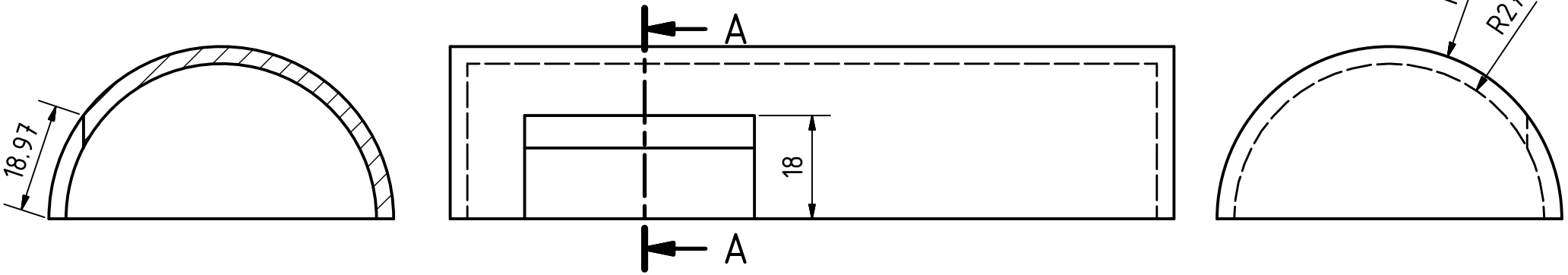

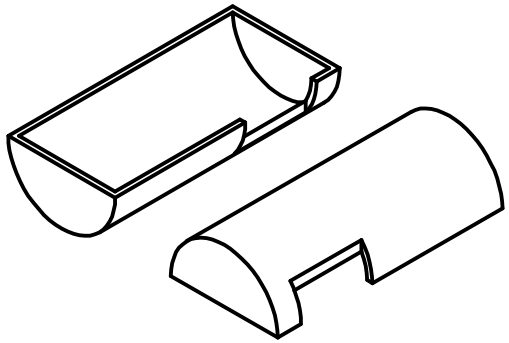

					Datum	Name
				Gezeichnet	09.03.2015	l21bstgi
				Kontrolliert		
				Norm		
Status	Änderungen	Datum	Name			

tungsten_shield

1

A4

Appendix D

Ear thickness data of the in-vivo mouse ear study

The following figures show the detailed ear thickness data of the X-ray pilot study and the comparative proton study. The ear thickness of each individual mouse of the X-ray and proton groups is displayed for the monitoring period of 90 days. The thickness was measured in triplicate for each time point. The mean thickness for each group can be found in the main text (section 6.3.2 and 6.5.1).

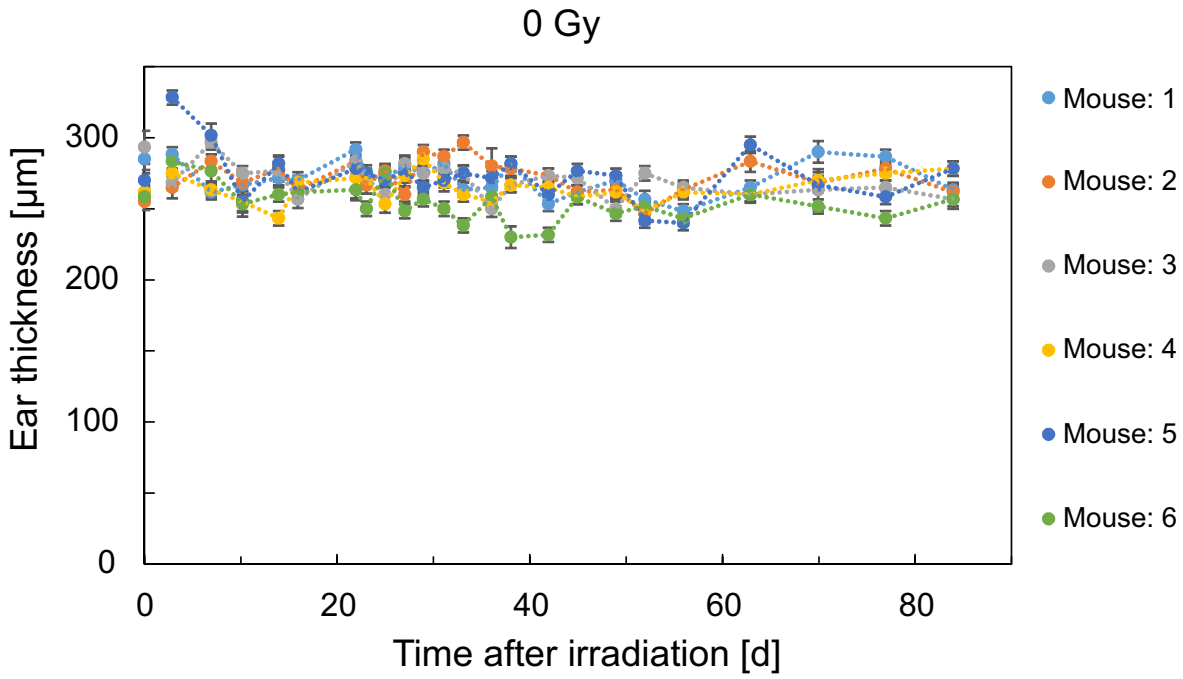

Figure D.1: *Ear thickness (±SEM) of the sham-irradiated (right) ear of each mouse of the X-ray control group for 90 days (0 Gy).*

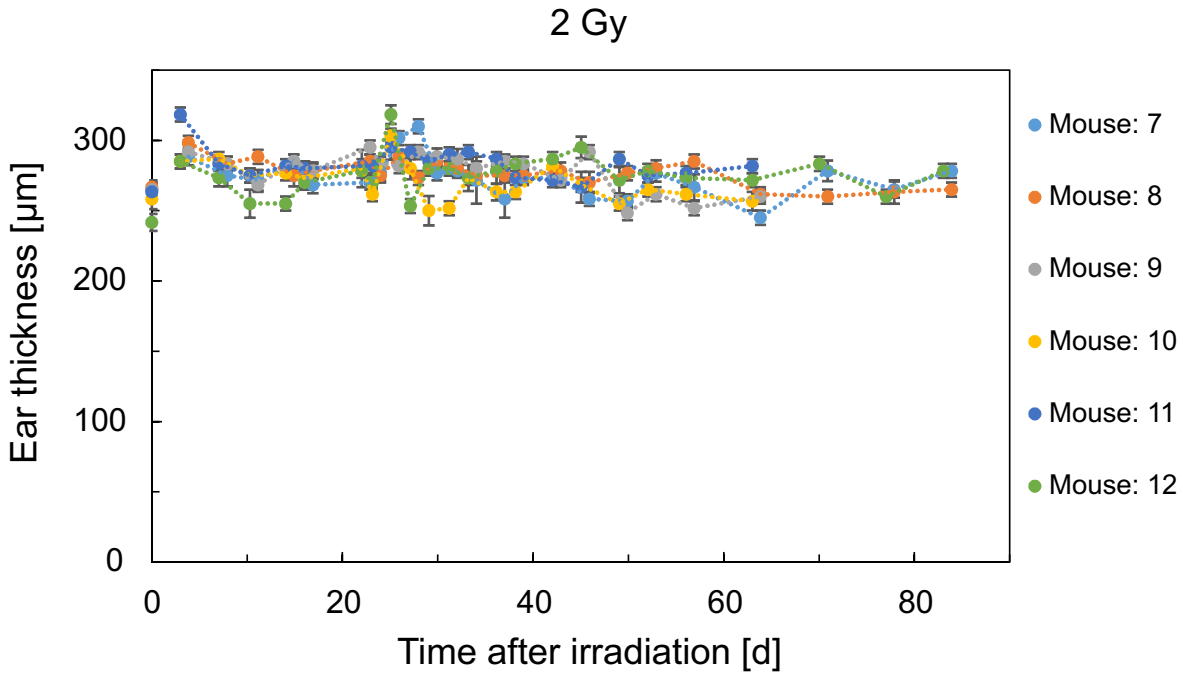

Figure D.2: *Ear thickness (±SEM) of the irradiated (right) ear of each mouse for 90 days following homogeneous X-ray irradiation at 2 Gy.*

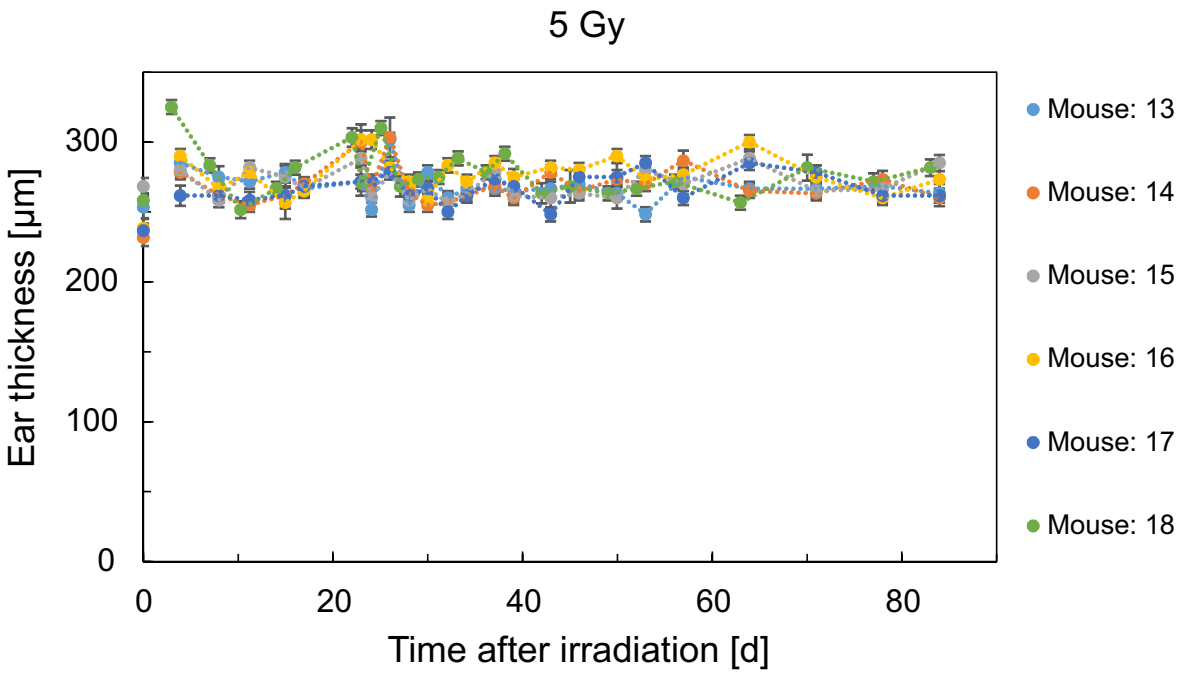

Figure D.3: *Ear thickness (±SEM) of the irradiated (right) ear of each mouse for 90 days following homogeneous X-ray irradiation at 5 Gy.*

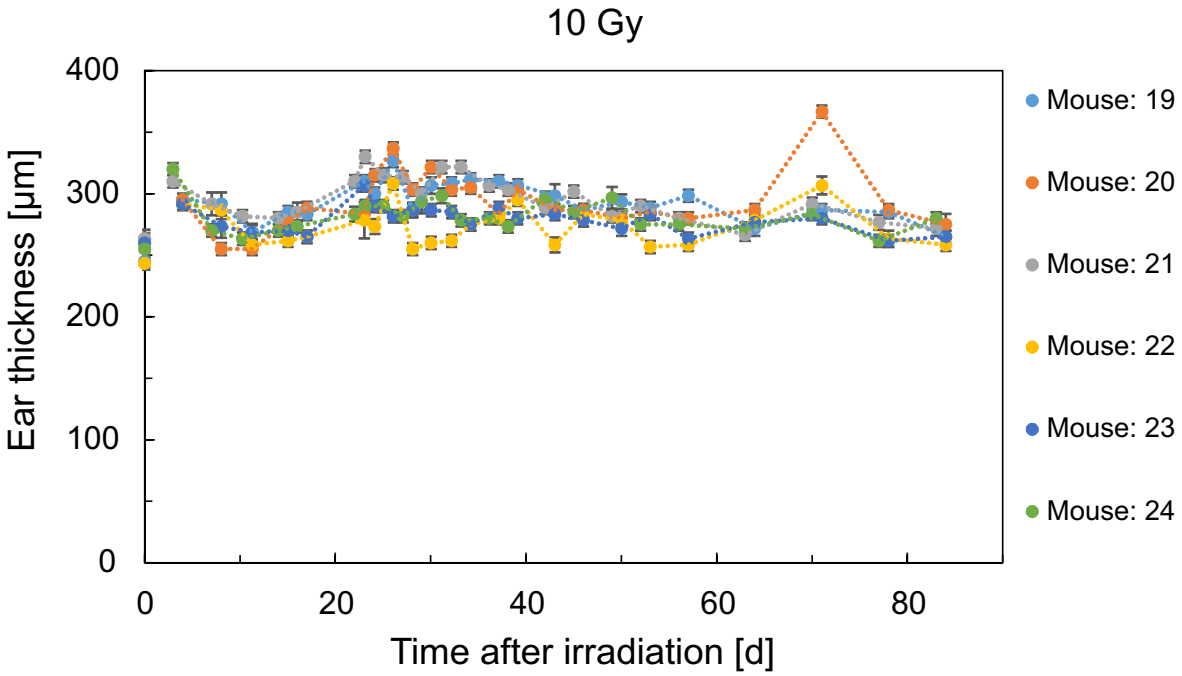

Figure D.4: *Ear thickness (±SEM) of the irradiated (right) ear of each mouse for 90 days following homogeneous X-ray irradiation at 10 Gy.*

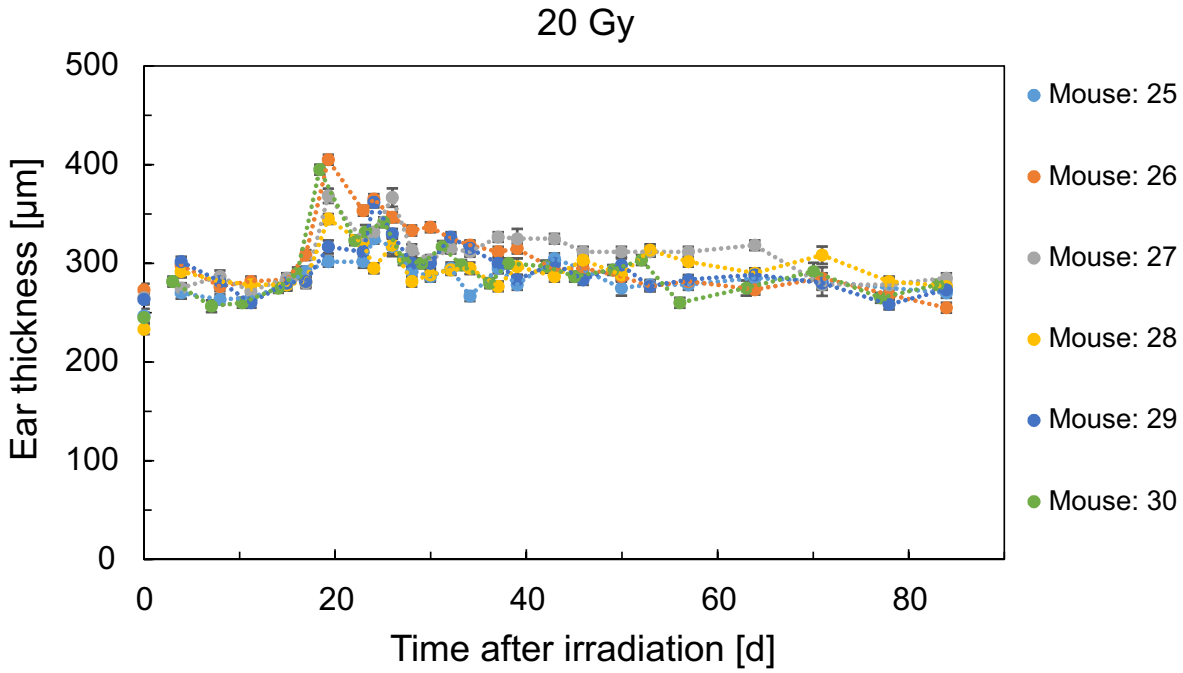

Figure D.5: *Ear thickness (±SEM) of the irradiated (right) ear of each mouse for 90 days following homogeneous X-ray irradiation at 20 Gy.*

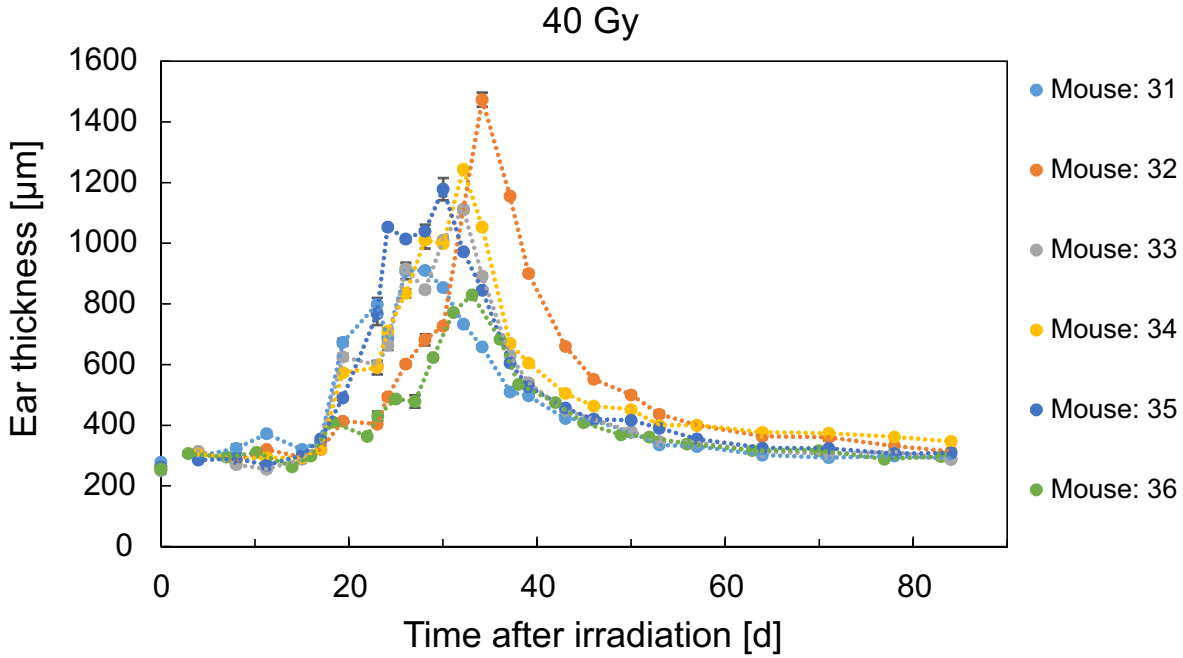

Figure D.6: *Ear thickness (±SEM) of the irradiated (right) ear of each mouse for 90 days following homogeneous X-ray irradiation at 40 Gy.*

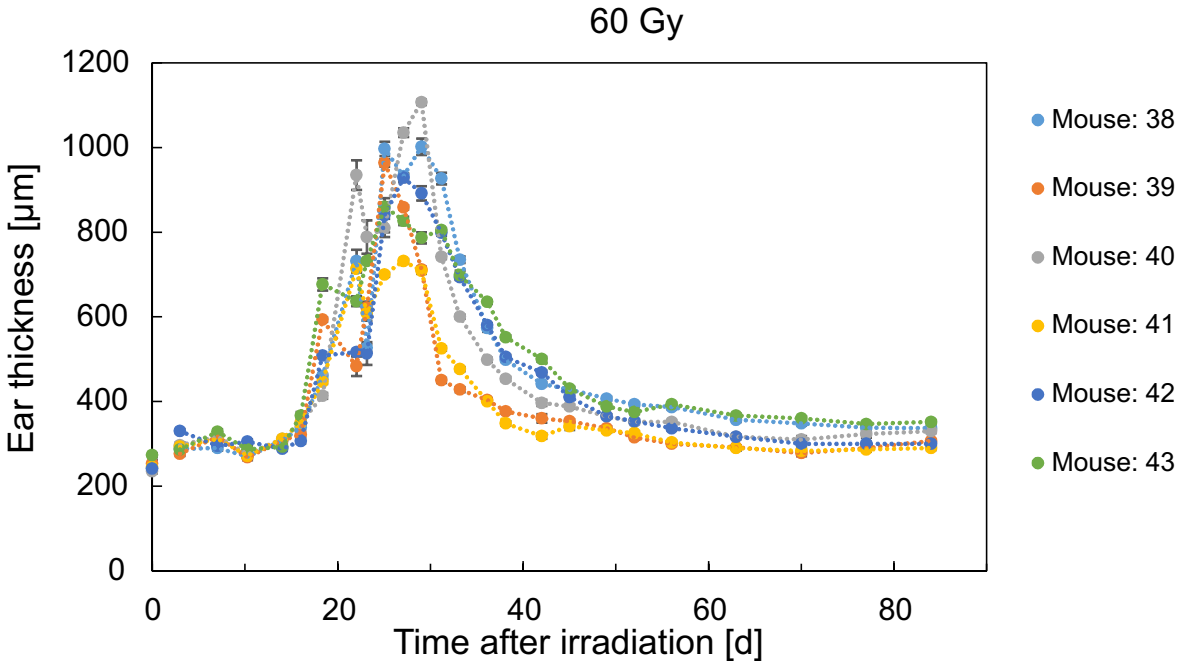

Figure D.7: *Ear thickness (±SEM) of the irradiated (right) ear of each mouse for 90 days following homogeneous X-ray irradiation at 60 Gy.*

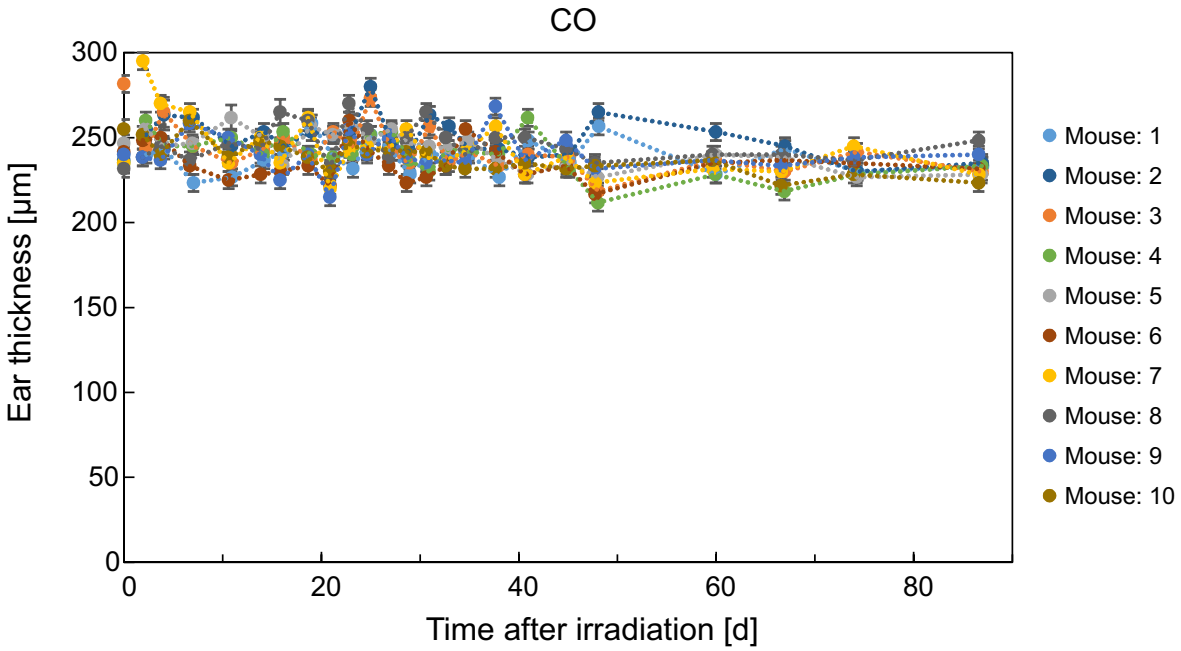

Figure D.8: *Ear thickness (±SEM) of the sham-irradiated (right) ear of each mouse of the proton control group (CO) for 90 days after irradiation.*

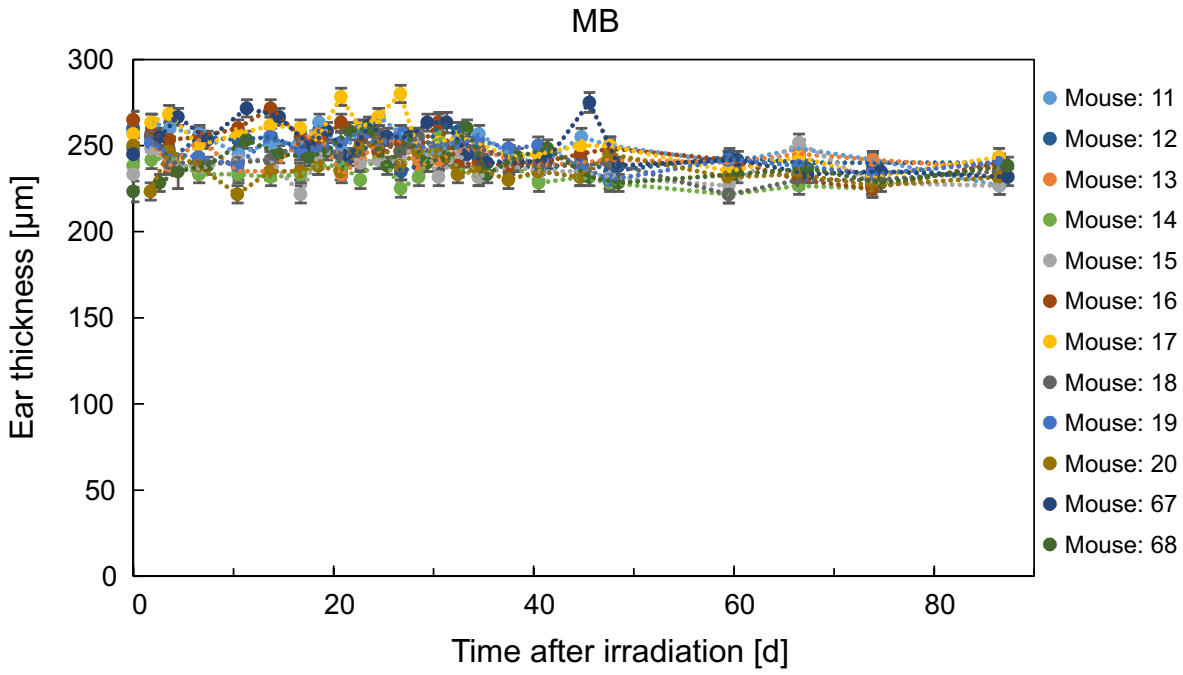

Figure D.9: *Ear thickness (±SEM) of the irradiated (right) ear of each mouse of the minibeam (MB) group for 90 days after irradiation.*

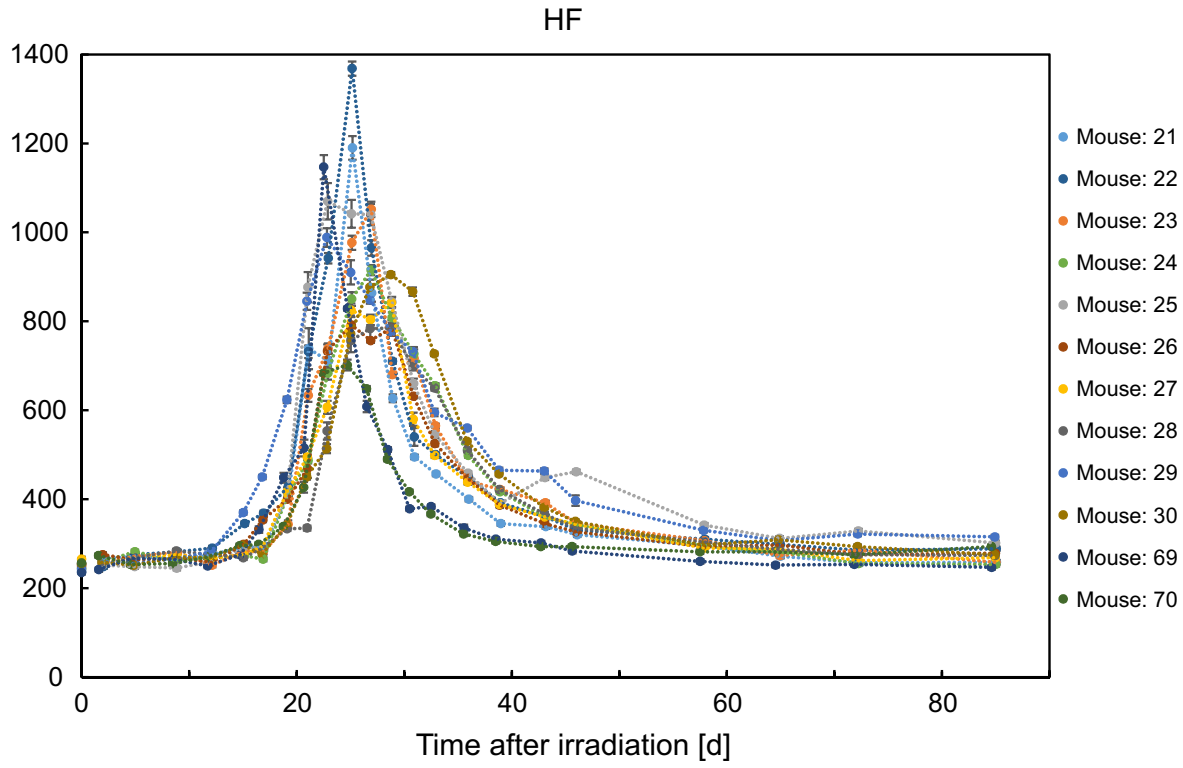

Figure D.10: *Ear thickness (±SEM) of the irradiated (right) ear of each mouse for 90 days following homogeneous proton irradiation (HF).*

Bibliography

[1] *Global Cancer Facts & Figures*, Atlanta: American Cancer Society, 3rd edition, 2015.

[2] *Krebs in Deutschland 2009/2010*, Robert Koch-Institut und die Gesellschaft der epidemiologischen Krebsregister in Deutschland e.V., 9th edition, 2013.

[3] P. Gallet, B. Phulpin, J.-L. Merlin, A. Leroux, P. Bravetti, H. Mecellem, N. Tran, G. Dolivet, *Long-term alterations of cytokines and growth factors expression in irradiated tissues and relation with histological severity scoring*, PloS ONE **6** (2011) e29399.

[4] W.P. Hogle, *The state of the art in radiation therapy*, **22** (2006) 212–220.

[5] L.J. Schreiner, *Dosimetry in modern radiation therapy: limitations and needs*, in *Journal of Physics: Conference Series*, Vol. 56, p. 1, IOP Publishing, 2006.

[6] E.B. Podgorsak et al., *Radiation oncology physics: a handbook for teachers and students*, Vienna: International Atomic Energy Agency, 2005.

[7] *Radiation Therapy and You: Support for People With Cancer*, National Cancer Institute; NIH Publication No. 12-7157, 2012.

[8] N. Salvo, E. Barnes, J. Van Draanen, E. Stacey, G. Mitera, D. Breen, A. Giotis, G. Czarnota, J. Pang, C. De Angelis, *Prophylaxis and management of acute radiation-induced skin reactions: a systematic review of the literature*, Current Oncology **17** (2010) 94.

[9] *Wikipedia, the free encyclopedia*, URL http://en.wikipedia.org/.

[10] M. Sakka, R. Kamata, *An increase in tolerance in mice by field-fractionated (sieve) X-irradiation*, Radiation research **9** (1958) 341–345.

[11] R.E. Albert, F.J. Burns, R.D. Heimbach, *Skin damage and tumor formation from grid and sieve patterns of electron and beta radiation in the rat*, Radiation research **30** (1967) 525–540.

[12] F.J. Burns, R.E. Albert, P. Bennett, I.P. Sinclair, *Tumor incidence in rat skin after proton irradiation in a sieve pattern*, Radiation research **50** (1972) 181–190.

[13] H.R. Withers, J.M.G. Taylor, B. Maciejewski, *Treatment volume and tissue tolerance*, International Journal of Radiation Oncology* Biology* Physics **14** (1988) 751–759.

[14] E. Brauer-Krisch, H. Requardt, P. Regnard, S. Corde, E. Siegbahn, G. LeDuc, T. Brochard, H. Blattmann, J. Laissue, A. Bravin, *New irradiation geometry for microbeam radiation therapy*, Physics in medicine and biology **50** (2005) 3103.

[15] F.A. Dilmanian, Z. Zhong, T. Bacarian, H. Benveniste, P. Romanelli, R. Wang, J. Welwart, Te. Yuasa, E.M. Rosen, D.J. Anschel, *Interlaced x-ray microplanar beams: a radiosurgery approach with clinical potential*, Proceedings of the National Academy of Sciences **103** (2006) 9709–9714.

[16] D.N. Slatkin, F.A. Dilmanian, P.O. Spanne, *Method for microbeam radiation therapy*, 1994, US Patent 5,339,347.

[17] S. Girst, C. Greubel, J. Reindl, C. Siebenwirth, O. Zlobinskaya, D.W.M. Walsh, K. Ilicic, M. Aichler, A. Walch, J.J. Wilkens, G. Multhoff, G. Dollinger, T.E. Schmid, *Proton minibeam radiation therapy reduces side effects in an in-vivo mouse ear model*, International Journal of Radiation Oncology* Biology* Physics (2015).

[18] F.A. Dilmanian, J.G. Eley, S. Krishnan, *Minibeam Therapy With Protons and Light Ions: Physical Feasibility and Potential to Reduce Radiation Side Effects and to Facilitate Hypofractionation*, International Journal of Radiation Oncology* Biology* Physics (2015).

[19] Y. Prezado, G.R. Fois, *Proton-minibeam radiation therapy: A proof of concept*, Medical physics **40** (2013) 031712.

[20] J.A. Laissue, H. Blattmann, H.P. Wagner, M.A. Grotzer, D.N. Slatkin, *Prospects for microbeam radiation therapy of brain tumours in children to reduce neurological sequelae*, Developmental Medicine & Child Neurology **49** (2007) 577–581.

[21] D.J. Anschel, A. Bravin, P. Romanelli, *Microbeam radiosurgery using synchrotron-generated submillimetric beams: a new tool for the treatment of brain disorders*, Neurosurgical review **34** (2011) 133–142.

[22] F.A. Dilmanian, A.G. Meek, *Heavy ion therapy with microbeams*, 2012, US Patent 8,269,198.

[23] O. Zlobinskaya, S. Girst, C. Greubel, V. Hable, C. Siebenwirth, D.W.M. Walsh, G. Multhoff, J.J. Wilkens, T.E. Schmid, G. Dollinger, *Reduced side effects by proton microchannel radiotherapy: study in a human skin model*, Radiation and environmental biophysics **52** (2013) 123–133.

[24] S. Girst, C. Marx, E. Bräuer-Krisch, A. Bravin, S. Bartzsch, U. Oelfke, C. Greubel, J. Reindl, C. Siebenwirth, O. Zlobinskaya, G. Multhoff, G. Dollinger, T.E. Schmid, J.J. Wilkens, *Improved normal tissue protection by proton and X-ray microchannels compared to homogeneous field irradiation*, Physica Medica **31** (2015) 615–620.

[25] S. Girst, C. Greubel, J. Reindl, C. Siebenwirth, O. Zlobinskaya, G. Dollinger, T.E. Schmid, *The influence of the channel size on the reduction of side effects in microchannel proton therapy*, Radiation and environmental biophysics **54** (2015) 335–342.

[26] C. Greubel, *Einfluss der zeitlichen und räumlichen Fokussierung auf die strahlenbiologische Wirksamkeit von Protonen*, PhD thesis, Universität der Bundeswehr München, 2013.

[27] M. Goitein, *Radiation Oncology: A Physicist's-Eye View*, Springer Science & Business Media, 2007.

[28] J.F. Ziegler, *Stopping of energetic light ions in elemental matter*, Journal of applied physics **85** (1999) 1249–1272.

[29] J.F. Ziegler, J.P. Biersack, *The Stopping and Range of Ions in Matter (SRIM & TRIM)*, URL http://www.srim.org.

[30] M. Durante, J.S. Loeffler, *Charged particles in radiation oncology*, Nature reviews Clinical oncology **7** (2010) 37–43.

[31] B. Gottschalk, A.M. Koehler, R.J. Schneider, J.M. Sisterson, M.S. Wagner, *Multiple Coulomb scattering of 160 MeV protons*, Nuclear Instruments and Methods

in Physics Research Section B: Beam Interactions with Materials and Atoms **74** (1993) 467–490.

[32] G. Moliere, *Theorie der Streuung schneller geladener Teilchen II Mehrfach-und Vielfachstreuung*, Zeitschrift für Naturforschung A **3** (1948) 78–97.

[33] S. Nill, *Development and application of a multi-modality inverse treatment planning system*, (2001).

[34] M.N. Varma, J.W. Baum, A.V. Kuehner, *Radial Dose, LET, and W for 16 O Ions in N2 and Tissue-Equivalent Gases*, Radiation research **70** (1977) 511–518.

[35] M.N. Varma, J.W. Baum, *Energy Deposition in Nanometer Regions by 377 MeV/Nucleon Ions*, Radiation Research **81** (1980) 355–363.

[36] J. Kiefer, H. Straaten, *A model of ion track structure based on classical collision dynamics (radiobiology application)*, Physics in medicine and biology **31** (1986) 1201.

[37] T. Elsässer, M. Scholz, *Cluster Effects within the Local Effect Model*, Radiat. Res. **167** (2007) 319–329.

[38] T. Elsässer, M. Krämer, M. Scholz, *Accuracy of the local effect model for the prediction of biologic effects of carbon ion beams in vitro and in vivo*, International Journal of Radiation Oncology* Biology* Physics **71** (2008) 866–872.

[39] W. Wang, Z. Yu, W. Su, *Ion irradiation induced direct damage to DNA*, arXiv preprint arXiv:0807.0079 (2008).

[40] B.D. Michael, P. O'Neill, *A sting in the tail of electron tracks*, Science **287** (2000) 1603–1604.

[41] M.C. Joiner, A. van der Kogel, *Basic Clinical Radiobiology*, CRC Press, 4th edition, 2009.

[42] B. Alberts, D. Bray, J. Lewis, M. Raff, K. Roberts, J.D. Watson, *Molekularbiologie der Zelle*, WILEY-VCH Verlag GmbH & Co. KGaA, Weinheim, 2004.

[43] E.J. Hall, A.J. Giaccia, *Radiobiology for the Radiologist*, Lippincott Williams & Wilkins, 2006.

[44] A. Hauptner, W. Friedland, S. Dietzel, G.A. Drexler, C. Greubel, V. Hable, H. Strickfaden, T. Cremer, A.A. Friedl, R. Krücken, H.G. Paretzke, G. Dollinger,

Spatial Distribution of DNA Double-Strand Breaks from Ion Tracks, in P. Sigmund, editor, *Ion Beam Science: Solved and Unsolved Problems*, Vol. 52 of *Matematisk-fysiske Meddelelser*, pp. 59–85, Royal Danish Academy of Sciences and Letters, Copenhagen, 2006.

[45] G.P. van der Schans, J.F. Bleichrodt, J. Blok, *Contribution of various types of damage to inactivation of a biologically-active double-stranded circular DNA by gamma-radiation*, International Journal of Radiation Biology **23** (1973) 133–150.

[46] J.R. Savage, *Classification and relationships of induced chromosomal structual changes.*, Journal of Medical Genetics **13** (1976) 103.

[47] K.K. Khanna, S.P. Jackson, *DNA double-strand breaks: signaling, repair and the cancer connection*, Nature genetics **27** (2001) 247–254.

[48] E.C. Mackonis, N. Suchowerska, M. Zhang, M. Ebert, D.R. McKenzie, M. Jackson, *Cellular response to modulated radiation fields*, Physics in medicine and biology **52** (2007) 5469.

[49] J.A. Laissue, G. Geiser, P.O. Spanne, F.A. Dilmanian, J.-O. Gebbers, M. Geiser, X.-Y. Wu, M.S. Makar, P.L. Micca, M.M. Nawrocky et al., *Neuropathology of ablation of rat gliosarcomas and contiguous brain tissues using a microplanar beam of synchrotron-wiggler-generated X rays*, International journal of cancer **78** (1998) 654–660.

[50] W.E. Straile, H.B. Chase, *The Use of Elongate Microbeams of X-Rays for Simulating the Effects of Cosmic Rays on Tissues: A Study of Wound Healing and Hair Follicle Regeneration*, Radiation research **18** (1963) 65–75.

[51] A. Köhler, *Theorie einer Methode, bisher unm"oglich unanwendbar hohe Dosen R"ontgenstrahlen in der Tiefe des Gewebes zur therapeutischen Wirksamkeit zu bringen ohne schwere Sch"adigung des Patienten, zugleich eine Methode des Schutzes gegen R"ontgenverbrennung "uberhaupt.*, Fortschritte auf dem Gebiet der Roentgenstrahlen **14** (1909) 27–9.

[52] F. Liberson, *The Value of a Multi-perforated Screen in Deep X-ray Therapy 1: A Preliminary Report on a New Method of Delivering Multiple Erythema Doses without Permanent Injury to the Skin*, Radiology **20** (1933) 186–195.

[53] M. Mohiuddin, D.L. Curtis, W.T. Grizos, L. Komarnicky, *Palliative treatment of advanced cancer using multiple nonconfluent pencil beam radiation: A pilot study*, Cancer **66** (1990) 114–118.

[54] W. Zeman, H.J. Curtis, C.P. Baker, *Histopathologic effect of high-energy-particle microbeams on the visual cortex of the mouse brain*, Radiation research **15** (1961) 496–514.

[55] H.J. Curtis, *The use of a deuteron microbeam for simulating the biological effects of heavy cosmic-ray particles*, Radiation Research Supplement (1967) 250–257.

[56] R. Asur, K.T. Butterworth, J.A. Penagaricano, K.M. Prise, R.J. Griffin, *High dose bystander effects in spatially fractionated radiation therapy*, Cancer letters **356** (2015) 52–57.

[57] I. Martínez-Rovira, G. Fois, Y. Prezado, *Dosimetric evaluation of new approaches in GRID therapy using nonconventional radiation sources*, Medical Physics **42** (2015) 685–693.

[58] F.A. Dilmanian, Y. Qu, L.E. Feinendegen, L.A. Peña, T. Bacarian, F.A. Henn, J. Kalef-Ezra, S. Liu, Z. Zhong, J.W. McDonald, *Tissue-sparing effect of x-ray microplanar beams particularly in the CNS: Is a bystander effect involved?*, Experimental hematology **35** (2007) 69–77.

[59] F.A. Dilmanian, G.M. Morris, N. Zhong, T. Bacarian, J.F. Hainfeld, J. Kalef-Ezra, L.J. Brewington, J. Tammam, E.M. Rosen, *Murine EMT-6 carcinoma: high therapeutic efficacy of microbeam radiation therapy*, Radiation research **159** (2003) 632–641.

[60] O.V. Belyakov, S.A. Mitchell, D. Parikh, G. Randers-Pehrson, S.A. Marino, S.A. Amundson, C.R. Geard, D.J. Brenner, *Biological effects in unirradiated human tissue induced by radiation damage up to 1 mm away*, Proceedings of the National Academy of Sciences of the United States of America **102** (2005) 14203–14208.

[61] O.A. Sedelnikova, A. Nakamura, O. Kovalchuk, I. Koturbash, S.A. Mitchell, S.A. Marino, D.J. Brenner, W.M. Bonner, *DNA double-strand breaks form in bystander cells after microbeam irradiation of three-dimensional human tissue models*, Cancer research **67** (2007) 4295–4302.

[62] J.S. Dickey, F.J. Zemp, A. Altamirano, O.A Sedelnikova, W.M. Bonner, O. Kovalchuk, *H2AX phosphorylation in response to DNA double-strand break formation during bystander signalling: effect of microRNA knockdown*, Radiation protection dosimetry **143** (2011) 264–269.

[63] O.V. Belyakov, M. Folkard, C. Mothersill, K.M. Prise, B.D. Michael, *Bystander-induced differentiation: a major response to targeted irradiation of a urothelial*

explant model, Mutation Research/Fundamental and Molecular Mechanisms of Mutagenesis **597** (2006) 43–49.

[64] F.A. Dilmanian, T.M. Button, G. Le Duc, N. Zhong, L.A. Peña, J.A.L. Smith, S.R. Martinez, T. Bacarian, J. Tammam, B. Ren et al., *Response of rat intracranial 9L gliosarcoma to microbeam radiation therapy*, Neuro-oncology **4** (2002) 26–38.

[65] J.C. Crosbie, R.L. Anderson, K. Rothkamm, C.M. Restall, L. Cann, S. Ruwanpura, S. Meachem, N. Yagi, I. Svalbe, R.A. Lewis et al., *Tumor cell response to synchrotron microbeam radiation therapy differs markedly from cells in normal tissues*, International Journal of Radiation Oncology* Biology* Physics **77** (2010) 886–894.

[66] A. Uyama, T. Kondoh, N. Nariyama, K. Umetani, M. Fukumoto, K. Shinohara, E. Kohmura, *A narrow microbeam is more effective for tumor growth suppression than a wide microbeam: an in vivo study using implanted human glioma cells*, Journal of synchrotron radiation **18** (2011) 671–678.

[67] R. Serduc, A. Bouchet, E. Bräuer-Krisch, J.A. Laissue, J. Spiga, S. Sarun, A. Bravin, C. Fonta, L. Renaud, J. Boutonnat et al., *Synchrotron microbeam radiation therapy for rat brain tumor palliation - influence of the microbeam width at constant valley dose*, Physics in medicine and biology **54** (2009) 6711.

[68] P. Regnard, E.A. Siegbahn, A. Kusak, C. Clair, D. Dallery, J.A. Laissue, A. Bravin et al., *Irradiation of intracerebral 9L gliosarcoma by a single array of microplanar x-ray beams from a synchrotron: balance between curing and sparing*, Physics in medicine and biology **53** (2008) 861.

[69] ICRU, *Prescribing, recording, and reporting proton beam therapy*, International Commission on Radiation Units and Measurements. Report **78** (2007).

[70] E.W. Weisstein, *Convolution. From MathWorld–A Wolfram Web Resource.*, URL http://mathworld.wolfram.com/Convolution.html.

[71] F. Kamp, *Comparison of the Lateral Dose Fall-Off for Proton and Ion Beams in Radiation Therapy*, diploma thesis, TU München, 2011.

[72] J.O. Deasy, A.I. Blanco, V.H. Clark, *CERR: a computational environment for radiotherapy research*, Medical physics **30** (2003) 979–985.

[73] *MATLAB*, URL http://www.mathworks.com/.

[74] S. Schell, J.J. Wilkens, *Advanced treatment planning methods for efficient radiation therapy with laser accelerated proton and ion beams*, Medical physics **37** (2010) 5330–5340.

[75] G. Datzmann, *Aufbau und Charakterisierung des Hochenergie Rasterionenmikroskops SNAKE*, PhD thesis, TU München, 2002.

[76] P. Reichart, G. Datzmann, A. Hauptner, R. Hertenberger, C. Wild, G. Dollinger, *Three-dimensional hydrogen microscopy in diamond*, Science **306** (2004) 1537–1540.

[77] A. Hauptner, S. Dietzel, G.A. Drexler, P. Reichart, R. Krücken, T. Cremer, A.A. Friedl, G. Dollinger, *Microirradiation of cells with energetic heavy ions*, Radiation and environmental biophysics **42** (2004) 237–245.

[78] C. Greubel, V. Hable, G.A. Drexler, A. Hauptner, S. Dietzel, H. Strickfaden, I. Baur, R. Krücken, T. Cremer, A.A. Friedl et al., *Quantitative analysis of DNA-damage response factors after sequential ion microirradiation*, Radiation and environmental biophysics **47** (2008) 415–422.

[79] T.E. Schmid, G. Dollinger, V. Hable, C. Greubel, O. Zlobinskaya, D. Michalski, M. Molls, B. Röper, *Relative biological effectiveness of pulsed and continuous 20MeV protons for micronucleus induction in 3D human reconstructed skin tissue*, Radiotherapy and Oncology **95** (2010) 66–72.

[80] O. Zlobinskaya, C. Siebenwirth, C. Greubel, V. Hable, R. Hertenberger, N. Humble, S. Reinhardt, D. Michalski, B. Röper, G. Multhoff et al., *The Effects of Ultra-High Dose Rate Proton Irradiation on Growth Delay in the Treatment of Human Tumor Xenografts in Nude Mice*, Radiation research **181** (2014) 177–183.

[81] S. Girst, V. Hable, G.A. Drexler, C. Greubel, C. Siebenwirth, M. Haum, A.A. Friedl, G. Dollinger, *Subdiffusion supports joining of correct ends during repair of DNA double-strand breaks*, Scientific reports **3** (2013).

[82] G. Dollinger, *Kohlenstoffolien als Stripper für schwere Ionen*, PhD thesis, TU München, 1990.

[83] G. Datzmann, G. Dollinger, G. Hinderer, H.-J. Körner, *A Superconducting Multipole Lense for Focusing High Energy Ions*, Nucl. Instr. and Meth. B **158** (1999) 74–80.

[84] V. Hable, *Echtzeitbeobachtung schneller Reaktionskinetiken in lebenden Zellen nach Ionenmikrobestrahlung*, PhD thesis, Universität der Bundeswehr München, 2011.

[85] V. Hable, C. Greubel, A. Bergmaier, P. Reichart, A. Hauptner, R. Krücken, H. Strickfaden, S. Dietzel, T. Cremer, G.A. Drexler, A.A. Friedl, G. Dollinger, *The live cell irradiation and observation setup at SNAKE*, NIMB **267** (2009) 2090–2097.

[86] S. Girst, *Anomalous subdiffusion of DNA repair protein foci after ion microirradiation*, diploma thesis, TU München, 2011.

[87] A. Hauptner, *Mikroskopisch genaue Zellbestrahlung mit hochenergetischen Ionen*, PhD thesis, TU München, 2006.

[88] S. Reinhardt, M. Hillbrand, J.J. Wilkens, W. Assmann, *Comparison of Gafchromic EBT2 and EBT3 films for clinical photon and proton beams*, Medical physics **39** (2012) 5257–5262.

[89] *MatTek corporation, EpidermFT*, URL http://www.mattek.com/epidermft/technical-specifications.

[90] J.W. Hopewell, *The skin: its structure and response to ionizing radiation*, International journal of radiation biology **57** (1990) 751–773.

[91] Stopping Powers ICRU, *Ranges for Protons and Alpha Particles*, International Commission on Radiation Units and Measurements. Report **49** (1993).

[92] T. Mosmann, *Rapid colorimetric assay for cellular growth and survival: application to proliferation and cytotoxicity assays*, Journal of immunological methods **65** (1983) 55–63.

[93] M.V. Berridge, P.M. Herst, A.S. Tan, *Tetrazolium dyes as tools in cell biology: new insights into their cellular reduction*, Biotechnology annual review **11** (2005) 127–152.

[94] *MatTek corporation, Protocol for: In Vitro EpiDermTM skin irritation test*, URL https://eurl-ecvam.jrc.ec.europa.eu/validation-regulatory-acceptance/docs-skin-irritation-1/DOC13-SOP20modified20EpiDerm20MTT.pdf.

[95] D.A Kidd, M. Johnson, J. Clements, *Development of an in vitro corrosion/irritation prediction assay using the EpiDerm^{TM} skin model*, Toxicology in Vitro **21** (2007) 1292–1297.

[96] K. Müller, V. Meineke, *Radiation-induced alterations in cytokine production by skin cells*, Experimental hematology **35** (2007) 96–104.

[97] M. Martin, M.C. Vozenin, N. Gault, F. Crechet, C.M. Pfarr, J. Lefaix, *Coactivation of AP-1 activity and TGF-beta1 gene expression in the stress response of normal skin cells to ionizing radiation.*, Oncogene **15** (1997) 981–989.

[98] D. Telgenhoff, B. Shroot, *Cellular senescence mechanisms in chronic wound healing*, Cell Death & Differentiation **12** (2005) 695–698.

[99] S.X. Leng, J.E. McElhaney, J.D. Walston, D. Xie, N.S. Fedarko, G.A. Kuchel, *ELISA and multiplex technologies for cytokine measurement in inflammation and aging research*, The Journals of Gerontology Series A: Biological Sciences and Medical Sciences **63** (2008) 879–884.

[100] E. Engvall, P. Perlmann, *Enzyme-linked immunosorbent assay (ELISA) quantitative assay of immunoglobulin G*, Immunochemistry **8** (1971) 871–874.

[101] K. Kaveh, V.S.K. Manem, M. Kohandel, S. Sivaloganathan, *Modeling age-dependent radiation-induced second cancer risks and estimation of mutation rate: an evolutionary approach*, Radiation and environmental biophysics (2014) 1–12.

[102] M. Fenech, *The in vitro micronucleus technique*, Mutation Research/Fundamental and Molecular Mechanisms of Mutagenesis **455** (2000) 81–95.

[103] S. Bonassi, R. El-Zein, C. Bolognesi, M. Fenech, *Micronuclei frequency in peripheral blood lymphocytes and cancer risk: evidence from human studies*, Mutagenesis **26** (2011) 93–100.

[104] M. Fenech, A.A. Morley, *Cytokinesis-block micronucleus method in human lymphocytes: effect of in vivo ageing and low dose X-irradiation*, Mutation Research/Fundamental and Molecular Mechanisms of Mutagenesis **161** (1986) 193–198.

[105] M. Kirsch-Volders, T. Sofuni, M. Aardema, S. Albertini, D. Eastmond, M. Fenech, M. Ishidate, S. Kirchner, E. Lorge, T. Morita et al., *Report from the in vitro micronucleus assay working group*, Mutation Research/Genetic Toxicology and Environmental Mutagenesis **540** (2000) 153–163.

[106] R.D. Curren, G.C. Mun, D. Gibson, M.J. Aardema, *Development of a method for assessing micronucleus induction in a 3D human skin model (EpiDerm^{TM})*, Mutation Research/Genetic Toxicology and Environmental Mutagenesis **607** (2006) 192–204.

[107] G.C. Mun, M.J. Aardema, T. Hu, B. Barnett, Y. Kaluzhny, M. Klausner, V. Karetsky, E.L. Dahl, R.D. Curren, *Further development of the EpiDerm^{TM} 3D reconstructed human skin micronucleus (RSMN) assay*, Mutation Research/Genetic Toxicology and Environmental Mutagenesis **673** (2009) 92–99.

[108] K. Fleckenstein, B. Gauter-Fleckenstein, I.L. Jackson, Z. Rabbani, M. Anscher, Z. Vujaskovic, *Using biological markers to predict risk of radiation injury*, in *Seminars in radiation oncology*, Vol. 17, pp. 89–98, Elsevier, 2007.

[109] M.-F. Chen, W.-C. Chen, C.-H. Lai, C.-H. Hung, K.-C. Liu, Y.-H. Cheng, *Predictive factors of radiation-induced skin toxicity in breast cancer patients*, BMC cancer **10** (2010) 508.

[110] M. Martin, J.-L. Lefaix, S. Delanian, *TGF-β1 and radiation fibrosis: a master switch and a specific therapeutic target?*, International Journal of Radiation Oncology* Biology* Physics **47** (2000) 277–290.

[111] T. Sugawara, R.M. Gallucci, P.P. Simeonova, M.I. Luster, *Regulation and role of interleukin 6 in wounded human epithelial keratinocytes*, Cytokine **15** (2001) 328–336.

[112] R.S. Asur, S. Sharma, C.-W. Chang, J. Penagaricano, I.M. Kommuru, E.G. Moros, P.M. Corry, R.J. Griffin, *Spatially fractionated radiation induces cytotoxicity and changes in gene expression in bystander and radiation adjacent murine carcinoma cells*, Radiation research **177** (2012) 751–765.

[113] K.T. Butterworth, C.K. McGarry, C. Trainor, J.M. O'Sullivan, A.R. Hounsell, K.M. Prise, *Out-of-field cell survival following exposure to intensity-modulated radiation fields*, International Journal of Radiation Oncology* Biology* Physics **79** (2011) 1516–1522.

[114] J.P. Williams, S.L. Brown, G.E. Georges, M. Hauer-Jensen, R.P. Hill, A.K. Huser, D.G. Kirsch, T.J. MacVittie, K.A. Mason, M.M. Medhora et al., *Animal models for medical countermeasures to radiation exposure*, Radiation research **173** (2010) 557–578.

[115] P. So, H. Kim, I. Kochevar, *Two-photon deep tissue ex vivo imaging of mouse dermal and subcutaneous structures*, Optics express **3** (1998) 339–350.

[116] D. Grahn, K.F. Hamilton, *Genetic variation in the acute lethal response of four inbred mouse strains to whole body X-irradiation*, Genetics **42** (1957) 189.

[117] R. Okayasu, K. Suetomi, Y. Yu, A. Silver, J.S. Bedford, R. Cox, R.L. Ullrich, *A deficiency in DNA repair and DNA-PKcs expression in the radiosensitive BALB/c mouse*, Cancer research **60** (2000) 4342–4345.

[118] E.B. Collen, M.N. Mayer, *Acute effects of radiation treatment: skin reactions*, The Canadian Veterinary Journal **47** (2006) 931.

[119] *Mosby's Medical Dictionary*, St. Louis, Missouri: Elsevier, 9th edition, 2013.

[120] M.I. Koster, *Making an epidermis*, Annals of the New York Academy of Sciences **1170** (2009) 7–10.

[121] M.P. Law, R.G. Ahier, S.B. Field, *The response of mouse skin to combined hyperthermia and X-rays*, International Journal of Radiation Biology **32** (1977) 153–163.

[122] M. Fenech, A.A. Morley, *Measurement of micronuclei in lymphocytes*, Mutation Research/Environmental Mutagenesis and Related Subjects **147** (1985) 29–36.

[123] F.A. Stewart, A.V. Akleyev, M. Hauer-Jensen, J.H. Hendry, N.J. Kleiman, T.J. Macvittie, B.M. Aleman, A.B. Edgar, K. Mabuchi, C.R. Muirhead et al., *ICRP publication 118: ICRP statement on tissue reactions and early and late effects of radiation in normal tissues and organs–threshold doses for tissue reactions in a radiation protection context*, Annals of the ICRP **41** (2012) 1–322.

[124] C. Siebenwirth, *Tumorbestrahlung mit gepulsten und kontinuierlichen Protonen am Mausmodell*, diploma thesis, TU München, 2010.

[125] E.A. Grice, J.A. Segre, *The skin microbiome*, Nature Reviews Microbiology **9** (2011) 244–253.

[126] H.J. Curtis, *The effect of a deuteron microbeam on graying of hair*, Radiation research **18** (1963) 510–515.

[127] M. Fenech, J. Denham, W. Francis, A.A. Morley, *Micronuclei in cytokinesis-blocked lymphocytes of cancer patients following fractionated partial-body radiotherapy*, International journal of radiation biology **57** (1990) 373–383.

[128] M.F. Fenech, V. Dunaiski, Y. Osborne, A.A. Morley, *The cytokinesis-block micronucleus assay as a biological dosimeter in spleen and peripheral blood lymphocytes of the mouse following acute whole-body irradiation*, Mutation Research Letters **263** (1991) 119–126.

[129] W.-U. Müller, A. Rode, *The micronucleus assay in human lymphocytes after high radiation doses (5–15 Gy)*, Mutation Research/Fundamental and Molecular Mechanisms of Mutagenesis **502** (2002) 47–51.

[130] N. Zhong, G.M. Morris, T. Bacarian, E.M. Rosen, A.F. Dilmanian, *Response of rat skin to high-dose unidirectional x-ray microbeams: a histological study*, Radiation research **160** (2003) 133–142.

[131] R.C.U. Priyadarshika, J.C. Crosbie, B. Kumar, P.A.W. Rogers, *Biodosimetric quantification of short-term synchrotron microbeam versus broad-beam radiation damage to mouse skin using a dermatopathological scoring system*, British Journal of Radiology **84** (2011) 833–42.

[132] R. Serduc, T. Christen, J. Laissue, R. Farion, A. Bouchet, B. Van Der Sanden, C. Segebarth, E. Bräuer-Krisch, G. Le Duc, A. Bravin et al., *Brain tumor vessel response to synchrotron microbeam radiation therapy: a short-term in vivo study*, Physics in medicine and biology **53** (2008) 3609.

[133] K. Rothkamm, J.C. Crosbie, F. Daley, S. Bourne, P.R. Barber, B. Vojnovic, L. Cann, P.A.W. Rogers, *In situ biological dose mapping estimates the radiation burden delivered to 'spared' tissue between synchrotron X-Ray microbeam radiotherapy tracks*, PloS ONE **7** (2012) e29853.

List of publications

2012

1. Low LET protons focused to submicrometer shows enhanced radiobiological effectiveness
T.E. Schmid, C. Greubel, V. Hable, O. Zlobinskaya, D. Michalski, **S. Girst**, C. Siebenwirth, E. Schmid, M. Molls, G. Multhoff, *Phys. Med. Biol.* **57** (2012) 5889

2013

2. Reduced side effects by proton microchannel radiotherapy: study in a human skin model
O. Zlobinskaya, **S. Girst**, C. Greubel, V. Hable, C. Siebenwirth, D.W.M. Walsh, G. Multhoff, J.J. Wilkens, T.E. Schmid, G. Dollinger, *Radiat. Environ. Biophys.* **52** (2013) 123

3. Subdiffusion supports joining of correct ends during repair of DNA double-strand breaks
S. Girst, V. Hable, G.A. Drexler, C. Greubel, C. Siebenwirth, M. Haum, A.A. Friedl and G. Dollinger, *Sci. Rep.* **3** (2013) 2511

2015

4. Live cell imaging at the Munich ion microbeam SNAKE–a status report
G.A. Drexler, C. Siebenwirth, S.E. Drexler, **S. Girst**, C. Greubel, G. Dollinger, A.A. Friedl, *Radiat. Oncol.* **10** (2015) 42

5. Determination of the accuracy for targeted irradiations of cellular substructures at SNAKE
C. Siebenwirth, C. Greubel, S.E. Drexler, **S. Girst**, J. Reindl, D.W.M. Walsh, G. Dollinger, A.A. Friedl, T.E. Schmid, G.A. Drexler, *Nucl. Instr. Meth. B* **348** (2015) 137

6. Improved normal tissue protection by proton and X-ray microchannels compared to homogeneous field irradiation
S. Girst, C. Marx, E. Bräuer-Krisch, A. Bravin, S. Bartzsch, U. Oelfke, C. Greubel, J. Reindl, C. Siebenwirth, O. Zlobinskaya, G. Multhoff, G. Dollinger, T.E. Schmid, J.J. Wilkens, *Physica Medica* **31** (2015) 615

7. The influence of the channel size on the reduction of side effects in microchannel proton therapy
S. Girst, C. Greubel, J. Reindl, C. Siebenwirth, O. Zlobinskaya, G. Dollinger, T.E. Schmid, *Radiat. Environ. Biophys.* **54** (2015) 335

8. Proton minibeam radiotherapy reduces side effects in an in-vivo mouse ear model
S. Girst, C. Greubel, J. Reindl, C. Siebenwirth, O. Zlobinskaya, D.W.M. Walsh, K. Ilicic, M. Aichler, A. Walch, J.J. Wilkens, G. Multhoff, G. Dollinger, T.E. Schmid, *International Journal of Radiation Oncology* Biology* Physics* (2015)

Acknowledgments

First of all I want to thank Professor Dr. Günther Dollinger for giving me the opportunity to accomplish this PhD project in his group, furthermore for his supervision and helpful support of this work.

Special thanks go to my colleagues Judith Reindl, Christoph Greubel, Christian Siebenwirth and former colleague Volker Hable, who helped me with any kind of problem that occurred and supported me all along this project.

Furthermore I want to thank all other members of the (extended) SNAKE team, especially Thomas Schmid, Olga Zlobinskaya, Dietrich Walsh, Katarina Ilicic, Jan Wilkens and Florian Kamp who contributed significantly to the completion and success of this project.

I also thank all other members of the LRT2 department (of the University of the Armed Forces) for helpful discussions and ideas and Wolfgang Engl and Ralf Schubert for help with constructions and fabrications, especially in urgent cases. Thank you also to the MLL team for support with the experimental part of this work.

Last but not least I am very thankful to my friends and above all my family and my partner Jan who supported me all along my studies and were always there when I needed them.